High Vacuum Chemical Vapor Deposition (HV-CVD) of Alumina Thin Films

THÈSE N^{O} 4485 (2009)

PRÉSENTÉE LE 11 SEPTEMBRE 2009

À LA FACULTE SCIENCES ET TECHNIQUES DE L'INGÉNIEUR
LABORATOIRE D'OPTIQUE APPLIQUÉE PROF. SALATHÉ
PROGRAMME DOCTORAL EN SCIENCE ET GÉNIE DES MATÉRIAUX

ÉCOLE POLYTECHNIQUE FÉDÉRALE DE LAUSANNE

POUR L'OBTENTION DU GRADE DE DOCTEUR ÈS SCIENCES

PAR

Xavier MULTONE

acceptée sur proposition du jury:

Prof. C. Ballif, président du jury
Dr P. Hoffmann, directeur de thèse
Prof. C. N. Afonso Rodriguez, rapporteur
Prof. M. Hitchman, rapporteur
Prof. P. Muralt, rapporteur

ÉCOLE POLYTECHNIQUE
FÉDÉRALE DE LAUSANNE
Suisse
2009

Abstract

We analyzed along this work the feasibility to produce high quality alumina thin films by High Vacuum Chemical Vapor Deposition (HV-CVD). We study the influence of various parameters on the growth process and on the film quality, such as substrate temperature, gas flow or pressure. We aim to highlight the advantages and the limitations of the HV-CVD technique. A high vacuum CVD reactor has been designed, built and optimized. A novel effusing source has been designed to guarantee a molecules distribution uniformity of 95% on the substrate surface.
The main technical challenges faced were to reach the maximum substrate temperature in vacuum, to control the precursor flux and to control the temperature of the gas lines to avoid condensation.

For the first time, films of Al_2O_3 are obtained by HV-CVD from aluminum isopropoxide as precursor in a novel HV-CVD reactor. The HV-CVD approach stands out of all the other CVD methods as it allows excellent prediction of growth rates and film thickness homogeneities if the decomposition probability of the precursor is once determined. In this work, the latter was determined to increase with increasing substrate temperature to 0.2, further increase of temperature reduces the decomposition probability due to increased desorption rate.

Pure alumina films are obtained in a reliable and reproducible way. The presence of oxidizing agents, as decomposition partners, reduces the activation energy of deposition process from 33.1 ± 8.2 kJ/mol to 11.4 ± 5.3 kJ/mol in presence of sufficient oxidizing agent. The Al_2O_3 films are growing at deposition rate from 1 to 50 nm/min.

It has been found that, the lower the deposition temperature, the higher the density of the deposited films therefore the higher refractive index. The index of refraction varies from 1.65 ± 0.01 to 1.35 ± 0.01 at 632 nm wavelength from lowest to highest deposition temperature.

At low deposition temperature, Al_2O_3 can contain residual OH-groups and Al=O entities. This content is independent of the total flow rates of the precursor in the range of $5 \cdot 10^{15}$ molecules/cm^2·s to $3 \cdot 10^{16}$ molecules/cm^2·s impinging on the substrate.
Substrate effects have not been observed in the limited range of tests on natural oxidized silicon, 3 µm SiO_2 on silicon, quartz, stainless steel, fused silica and 100 nm silicon nitride on top of silicon.

The chemical composition of the deposited alumina films measured by EDX and XPS is nearly stoichiometric with 35 ± 5 at% Al and 65 ± 5 at% O, without carbon contamination. Remaining hydrogen in the films has not been studied in detail, but the difference of OH- absorption peaks by FTIR indicates that, a low temperature deposition, hydrogen incorporation is possible.

Concerning the optical properties of the HV-CVD deposited films, absorption is very low from 250 nm to 1800 nm wavelength, but due to the porosity and granular structure of the films, light scattering can take place. But propagation loss smaller than 2 dB/cm were measured in channel waveguides fabricated from the HV-CVD alumina films. Planar and channel waveguides demonstrate good guiding properties at 670 nm and 1.55 µm, as well.

This work also opens new possibilities to deposit in situ local structures of or in transparent alumina on large surface. Light induced high vacuum chemical vapor deposition of alumina microstructures by 248 nm excimer laser is presented and shows an activation energy of 5.2 ± 0.4 kJ/mol, much smaller than for thermal deposition. The influence of the fluence and the repetition rate is discussed. Electron beam assisted HV-CVD of alumina is demonstrated and proves the feasibility of in situ structuration under HV-CVD conditions.

Key words: High Vacuum Chemical Vapor Deposition (HV-CVD), laser assisted CVD, electron beam assisted CVD, aluminum oxide, erbium doped alumina, waveguides.

Résumé

La faisabilité de production de films d'alumine par déposition chimique en phase vapeur sous vide (HV-CVD) est analysée dans ce travail. Nous avons étudié l'influence de différents paramètres, tels que la température du substrat, le flux de gaz ou la pression, sur le processus de croissance et sur la qualité des films ainsi obtenus. Nous voulons mettre en évidence les avantages et les limitations de cette technique. Un réacteur de déposition sous vide a été développé, construit et optimisé. Une nouvelle source effusive a été conçue de manière à garantir une distribution uniforme à 95% des molécules arrivant à la surface du substrat.

Les principaux challenges techniques rencontrés ont été d'obtenir une température du substrat maximale sous vide, de contrôler le flux du précurseur et de contrôler la température des lignes de gaz pour éviter toute condensation.

Pour la première fois, des films d'Al_2O_3 ont été obtenus par HV-CVD à partir de la décomposition d'aluminium isopropoxide comme précurseur dans ce nouveau réacteur sous vide. L'approche de déposition chimique en phase vapeur sous vide se démarque des autres procédés de déposition chimique en phase vapeur par la possibilité de prévoir le taux de croissance et l'homogénéité de l'épaisseur des films avec précision, à condition de connaitre au préalable la probabilité de décomposition du précurseur. Cette probabilité augmente, en augmentant la température, jusqu'à 0.2, ensuite re-diminue à plus haute température dû à l'augmentation du taux de désorption des molécules.

Des films d'alumine pure sont obtenus de manière fiable et reproductible par cette technique. La présence d'agent oxydant, comme partenaire de décomposition, diminue l'énergie d'activation du processus de 33.1 ± 8.2 kJ/mol à 11.4 ± 5.3 kJ/mol en présence suffisante d'agent d'oxydation. Les films d'oxyde d'aluminium sont déposés avec un taux de croissance allant de 1 à 50 nm/min.

Il a été démontré que plus la température de déposition est basse, plus la densité des films est élevée et ainsi plus l'indice de réfraction est élevé. L'indice de réfraction varie de 1.65

± 0.01 à 1.35 ± 0.01 pour une longueur d'onde de 632 nm et des films déposés à haute et basse température respectivement.
L'Al_2O_3 contient des groupes -OH résiduels et de l'Al=O. La présence de ces entités est indépendante du flux total de précurseur arrivant à la surface du substrat, pour de valeurs de flux de $5 \cdot 10^{15}$ molécules/$cm^2 \cdot s$ à $3 \cdot 10^{16}$ molécules/$cm^2 \cdot s$.
Aucun effet dû au substrat n'est observé dans la limite du nombre de tests effectués sur silicium, quartz, acier, verre, oxyde de silicium ou nitrure de silicium.
La composition chimique des films d'alumine, déposés par HV-CVD et mesurés par EDX et XPS, est quasi stœchiométrique avec 35 ± 5 at% Al et 65 ± 5 at% O. Aucune contamination carbonée n'est détectée. La présence d'hydrogène n'a pas été analysée en détails mais l'absorption par des groupes –OH mesurée par FTIR indique qu'à basse température de déposition de l'hydrogène résiduel peut être présent.

Concernant les propriétés optiques des films déposés par HV-CVD, nous constatons une très faible absorption dans l'intervalle de 250 à 1800 nm de longueur d'onde. Cependant, la porosité et la structure granulaire des films peuvent induire de la diffusion. Toutefois des pertes par propagation plus petites que 2 dB/cm ont été mesurées dans des guides d'onde fabriqués à partir d'alumine déposée par HV-CVD. Des guides d'onde planaire et bidimensionnel ont démontré d'excellentes propriétés de guidage à 670 nm et 1.55 μm.

Ce travail ouvre également de nouvelles portes pour la déposition in situ de structures locales d'alumine. Des microstructures déposées chimiquement en phase vapeur sous vide et assisté par excimer laser à 248 nm sont présentées et une énergie d'activation de 5.2 ± 0.4 kJ/mol est obtenue, nettement plus petite que dans le cas de la décomposition thermique. L'influence de la fluence et du taux de répétition est discutée. La déposition assistée par faisceau d'électrons est démontrée et prouve la faisabilité de structuration in-situ sous vide.

Mots clé : Déposition chimique en phase vapeur sous vide (HV-CVD), déposition assistée par laser, déposition assistée par faisceau d'électrons, oxyde d'aluminium, alumine dopée à l'erbium, guides d'onde.

Chapter 1 Introduction

1.1. General

The strong growth of telecommunication, data storage, display applications, etc in the last decade helped micro- and opto- electronics industries to become among the strongest technological drivers of our economy. The fast development of these technologies had expanded coating uses in diverse areas, as optical, protective, insulating or decorative thin films.
Thus, thin films deposition plays a key role in development of the semiconductors, microelectronics, optoelectronics, optics and many other fields.
Industry continuously demands films of improved quality and sophistication. Large efforts have been done in the domain of equipment to reach the requirements needed and to design more economical system. The rapid growth of deposition technology is also due to the improved understanding of the physics and chemistry of films, surfaces, interfaces and microstructure during the past thirty years.

Patterning, the basis of sophisticated functionality is generally obtained by lithographic processes resulting in alternating film deposition, lithography and etching steps. In-situ patterning is not applied industrially. Thin films depositions can be carried out by a large variety of technologies, none of them allows easy in situ patterning. Knowing that, patterning is not possible for most of the deposition technologies, we still present here some basic information about them. Before going in more detail in thin film deposition possibilities, we have to define what a thin film is and precisely state the most promising applications we are interested in.

The simplest common definition of thin film is: Thin material layers ranging from fraction of nanometers to several micrometers in thickness. However, it is difficult to define thin films with a physical dimension because the critical value thickness depends on the application and discipline. Thereby, Bunshah proposes another definition: A thin film is a coating that has different properties than the bulk material [1]. Smith goes even a step further pretending: Thin films are deposited onto bulk materials (substrates) to achieve properties unattainable or not easily obtainable in the substrates alone or deposited in a combination of different layers (multilayer) that can behave as completely new material [2].

Thin films are present in many and various applications of the daily life. A few examples of coatings are listed:

Decorative (metallization of surfaces)
Electrically functional (antistatic, insulating)

Mechanically functional (wear and friction resistant)
Chemically functional (corrosion resistant)
Optically functional (photovoltaic, communication, antireflection)

This latter application, optical functional thin films, will be discussed in more detail along this thesis.
Indeed, future optical system will operate with multi wavelengths at a frequency exceeding 1 Gbit/s. In order to allow for high functionality in optical routing and data processing such devices have to be compact. Furthermore, reliability and low cost will be key issues from the end user's point of view. The answer to these challenges will be the massive introduction of very large scale integrated photonics based on high index contrast waveguiding structures. Thin films technology is a promising solution for the fabrication of dielectric, high refractive index, high heat conductivity, amorphous or crystalline oxide materials, which can satisfy the properties needed for such next generation optical systems. Photonic devices will be useful wherever integration of light or amplification on the same chip is required (optical communication, cell phone, space equipment, etc). Transparent amorphous and crystalline oxide materials such as alumina (Al_2O_3) and yttria (Y_2O_3) can provide both advantages and will be studied in the next chapters.

1.2. Thin films deposition

Many dozens of deposition technique exist for the growth of films in the range of few nanometers to tens of micrometers.
The selection of a specific process for the formation of films can be based on a variety of considerations, for example: 1) material to deposit 2) properties needed 3) rate of deposition 4) limitation imposed by the substrate 5) purity of the film 6) adhesion to substrate 7) cost 8) ecological considerations [1].
The desired material characteristics of the deposited films will be, in most cases, the decisive factor for the selection of a preferred deposition technology [3].
The task of classifying the different technologies is difficult and can vary from different points of view: film properties desired, physical and chemical principles involved or type of equipment needed, etc.
We have to keep in mind that there are a large number of deposition techniques with no unique classification way; that each technique has its advantages and limitations and more than one technique can be used to deposit a specific film.

Here we decided to distinguish, first, two principles: purely physical or chemical deposition and then to subdivide each process in a classical way, as represented in Figure 1. A brief overview of each deposition technique is presented in the next two sections.

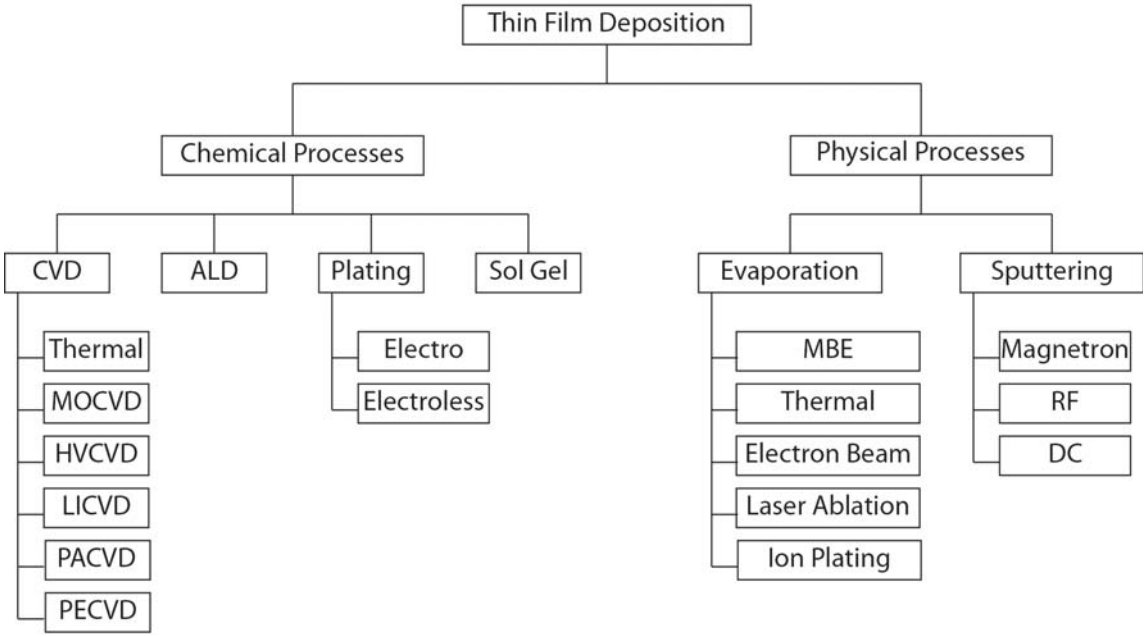

Figure 1 Overview of thin film deposition techniques [4].

There are some research approaches of patterning in CVD and electroplating [5].

1.2.1. Physical Vapor Deposition (PVD)

PVD is a method to deposit thin films by the condensation of a vaporized form of the material onto various surfaces. We generally distinguish two categories.

Evaporation:

A vapor is generated by boiling or subliming a source material and condensed to a solid film on the substrate surface [3].

Molecular Beam Epitaxy (MBE) is a sophisticated finely controlled method based on evaporation principle for growing epitaxial films in high vacuum.

Sputtering:

The ejection of surface atoms from an electrode surface by momentum transfer from bombarding ions to surface atoms produces a vapor of electrode material which is condensed on a substrate [3].
The most common source of sputtering is magnetron; which can be operated with Direct Current (DC) or Radio Frequency (RF).

1.2.2. Chemical Processes

Chemical Vapor Deposition (CVD):

For homogenous non patterned deposition the following CVD processes can be applied.
A non volatile solid material is deposited from a vapor, containing the material to be deposited, by a chemical reaction (possibly with other gases) occurring on or in the vicinity of a normally heated substrate [1, 6].

The CVD chemical reaction can be activated by several methods, in different environments and with different types of reactants, so we differentiate different CVD techniques; the following list is not exhaustive and only a short definition is given, more details will be presented in paragraph 1.3.

Metallo-Organic CVD (MOCVD) consists in use of metallo-organic compounds as precursor, resulting usually in lower temperature process as compared to the thermal decomposition of other types of precursors (halides or hydrides). The advantages of using metallo-organic precursors can be safety, improved deposition characteristics and reduction of unwanted side reactions in the gas phase.

Low Pressure CVD (LPCVD) (< 1 mbar) or *High Vacuum CVD* (HVCVD) (< 10^{-2} mbar) deal with deposition processes in vacuum. In that way, gas phase transport, thickness uniformity, film homogeneity and purity are increased.

Plasma Enhanced CVD (PECVD) uses a plasma environment to perform two functions: formation of chemical reactive species by electron impact collisions and promotion of surface chemistry with the energy supplied by the radiation present in the plasma (ions, electrons, photons). The combination of these two effects and the

strictly chemical reactions results in lower deposition temperature and different material properties are possible to obtain compared to standard CVD process.
Photo Assisted CVD (PACVD) exploits the photo activation of a reactant or a surface using electromagnetic radiation, usually ultraviolet or infrared radiation. Light is used to decompose compounds in the gas phase and/or adsorbed on a surface to form thin films. The photo activation enables deposition at enhanced rates and lower substrate temperature without damage due to ions bombardment.

Laser Induced CVD (LICVD) occurs as a result of the thermal energy from the laser coming in contact with and heating a substrate. Like in PACVD, laser induced CVD allows patterned films to be grown in situ by direct writing or image projection.

All these techniques will be described in more details in Chapter 2 in the particular case of the deposition of aluminum oxide.

Atomic Layer Deposition (ALD):

ALD is a special modification of CVD with the distinct feature that film growth takes place in a cyclic manner. At least two chemicals, called precursors, react with a surface one at a time in a sequential manner in order to deposit a thin film by repeatedly exposure of the precursors [7].

Sol Gel:

A stable chemical mixture of suspended precursor particles known as sol gel is spin coated, dipped or sprayed onto a substrate. A transition or destabilization of the sol occurs resulting in the formation of a gel and the gel is hardened to form a film [4].

1.2.3. Comparison of the major thin film deposition techniques

Properties	Evaporation	MBE	Sputtering	CVD	ALD
Production of depositing species	Thermal energy	Thermal energy	Momentum transfer	Chemical reaction	Chemical reaction
Deposition rate	Can be very high	Low	Low except for pure metal	Moderate to high	Low
Depositing species	Atoms and ions	Atoms and ions	Atoms and ions	Atoms	Atoms
Bombardment of substrate	Normally not	Not	Yes	Possible	Not
Substrate heating	Normally yes	Yes	Generally not	Yes	Yes
Energy of deposit species	Low	Low	Can be high	Low but can be high in PECVD	Low
Metal alloy deposition	Yes	Yes	Yes	Yes	Limited
Compound deposition	Yes	Yes	Yes	Yes	Yes
Advantages	Simple Versatile High rate	Film quality Thickness control Low temperature	Large range of elements	Large area Versatile High rate 3D coatings	Thickness control Low temperature Multilayer
Drawbacks	Vacuum technology No polymeric material	Low rate Complex Expensive	Vacuum technology No polymeric material	High temperature By-products	Slow By-products

Table 1 Comparison of the major thin film deposition techniques [1].

As we already mentioned before, the decision concerning the choice of a thin film deposition technique is mainly related to the films properties desired and the applications targeted.

Thus, the first question to ask is, "What properties are required for the optical applications we aim at?"

In simple words, we intend to deposit transparent, amorphous or crystalline, high refractive index oxide material. In the same time the objective is to grow high quality films with high uniformity on large area in an industrial orientation using standard substrates, as for instance silicon or quartz wafers. Finally, in order to fabricate some devices, the process must be versatile and allow to give the opportunity to in-situ locally structure the films by adding an external beam. Further motivations are developed in the paragraph 1.6.

The material chosen is aluminum oxide, also called alumina, because the required properties are fulfilled, as presented in paragraph 1.4.

Knowing the material, the properties and the restrictions (large area, local structuration) due to the applications, we can select a deposition technique.

CVD method is the best compromise for large area deposition, uniformity and film quality, furthermore high growth rate can be obtained. The possibility to add a laser beam (LICVD) to induce local structuring is a further argument for this technique.

In Chapter 2, we will study the possibilities to deposit alumina by CVD with emphasis on High Vacuum Chemical Vapor Deposition for high quality films and on Laser Induced Chemical Vapor Deposition for the structuration.

1.3. Chemical Vapor Deposition (CVD)

Basic fundamentals of Chemical Vapor Deposition are presented in this paragraph. General considerations on thermodynamics, kinetics, growth mechanisms and precursor's chemistry are exposed to precise the phenomena involved in CVD.

1.3.1. Fundamentals

The basic physicochemical principles involved in CVD are illustrated in Figure 2 and each individual CVD process steps may be summarized in terms of the following deposition sequence [8]:

- 1) Mass transport of the precursor from the reservoir to the deposition zone
- 2) Gas phase reactions
- 3) Mass transport of precursor to the substrate
- 4) Adsorption of precursor molecules on the growth surface
- 5) Surface diffusion of precursor molecules
- 6) Precursor decomposition and incorporation into the growing film
- 7) Desorption of by-products of the surface reactions
- 8) Mass transport of by-products away from the deposition zone

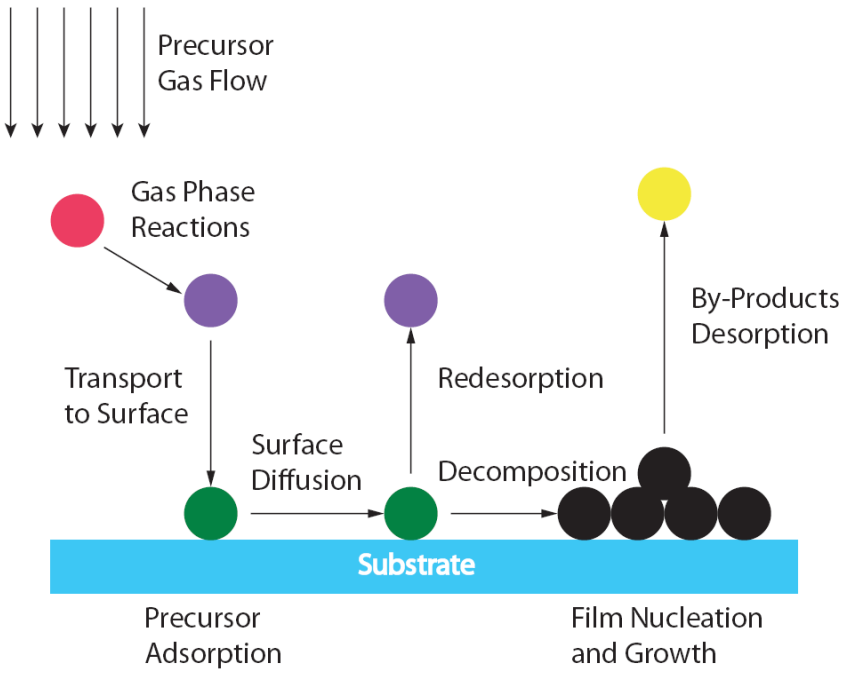

Figure 2 Transport and reaction processes in CVD [8].

Each process steps must be controlled in order to deposit thin films of uniform composition and film thickness with desired materials properties.
In case of HV-CVD the steps 2, 3 and 8 do not exist, whereas 1,4,5,6 and 7 are still relevant.

1.3.2. Film growth kinetics and mechanisms of HV-CVD

Thin films growth kinetics in HV-CVD is limited by the slowest process of the above sequence. The main physical parameters influencing the different phases of the deposition is the temperature; surface diffusion, adsorption, desorption and decomposition kinetics are all determined somehow by temperature. Three growth rate behaviors, in function of temperature, are distinguished in HV-CVD, see Figure 3.

1) *Chemical reaction limited* or *Surface reaction controlled*

   This regime occurs at low temperature when many gas molecules of precursor impinge on the substrate surface but the chemical reaction rate is poor. In other words, the growth rate is limited by temperature according to the Arrhenius law: $\text{Growth rate} \approx A \cdot e^{\frac{-E_a}{RT}}$

   Where E_a is the activation energy of the decomposition reaction, R is the gas constant, T is the temperature and A is a pre-exponential factor.
   The thickness of the film deposited in this regime is temperature dependant on each point of the substrate.

2) *Mass transport limited* or *Gas precursor supply controlled*

   Above a certain temperature, the growth rate is nearly independent of temperature. Precursor mass transport to the surface controls the rate. This regime is advantageous where it is difficult to obtain a uniform temperature distribution on the substrate, but to guarantee thickness uniformity, the gas flow distribution must be uniform. If the precursor flux is increased the mass transport limited regime starts at higher temperature.

3) *Desorption limited*

   The growth rate decreases even at higher temperature because of an increased desorption rate. In all regimes, the emergence of an alternative reaction path way may also lead to a variation (increase or decrease) in the growth rate [8].

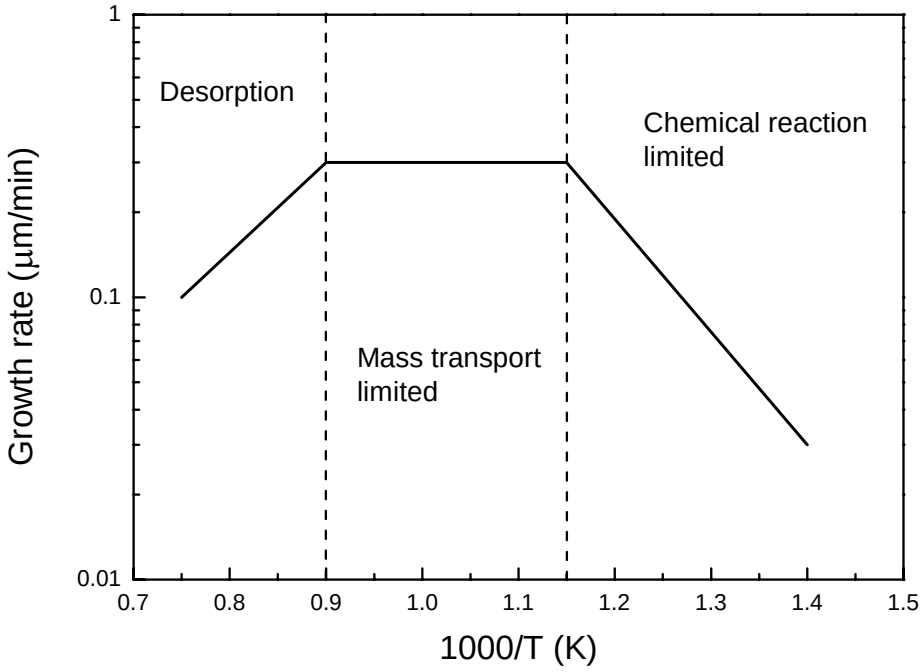

Figure 3 Typical HV-CVD deposition rate variation with reciprocal growth temperature.

Different film growth mechanisms take place in HV-CVD according to the deposition parameters. Growth rate and film microstructure are determined by surface diffusion and nucleation which are influenced principally by temperature, pressure, chemical composition, topology and surface impurities. Often amorphous films are deposited at low temperature and usually at high growth rate when surface diffusion is slow as compared to the impinging precursor flux. At higher temperature and lower growth rates when surface diffusion is fast compared to the incoming flux, epitaxial layers can be formed.

For crystalline growth, different main growth models for thin films are usually distinguished [8], but are not relevant here, because only amorphous alumina films are deposited.

1.3.3. Chemistry: Reactions and Precursors

Chemical reactions

Chemical reaction in CVD can be activated by several methods; the simplest one is the thermal decomposition (or pyrolysis): a precursor molecule is thermally dissociated into its elements or other simple molecules.
However several different species are usually involved in classical CVD chemical reactions, a typical example is the reaction between the precursor and a reactive gas. We distinguish different types of reaction [9]:

- *Oxidation and hydrolysis*
  O_2, CO_2, N_2O, O_3 or H_2O can be used as oxidizing agents.
  e.g. $SiH_4 + O_2 \rightarrow SiO_2 + 2H_2$ (400-450 °C)
  $SiCl_2H_2 + 2N_2O \rightarrow SiO_2 + 2N_2 + 2HCl$ (900 °C)

- *Hydrogen reduction*
  H_2 acts as reducing agent.
  e.g. $SiCl_4 + 2H_2 \rightarrow Si + 4HCl$ (1200 °C)

After this short overview of the different chemical reactions possible in CVD we have to determine if the desired reaction is feasible and will take place or not?
Thermodynamics can predict if the conditions are favorable. This is the case, if the transfer of energy, defined below, is negative. But it is important to precise that thermodynamics does not provide information on reaction speed and growth rate as well as limited to the case of chemical equilibrium, state that is rarely obtained in CVD processes. Furthermore in HV-CVD, the interaction time of molecules is limited to the residence time of the molecule adsorbed on the surface, which might kinetically hinder the reaction, i.e. the molecules do not react before being desorbed.

Anyway, if the Gibbs energy of reaction ΔG_r is negative, the forward reaction is spontaneous:

Where $\Delta G_r = \Delta G_r^0 + RT \ln Q$

with $\Delta G_r^0 = \sum \Delta G_f^0(\text{products}) - \sum \Delta G_f^0(\text{reactants})$, ΔG_f^0 is the standard Gibbs energy of formation, R is the gas constant, T is the temperature

and Q is the reaction quotient, $Q = \frac{\text{activities of products}}{\text{activities of reactants}}$ with each species raised to the power given by its stoichiometric coefficient [10].

Precursors

Several precursor families are briefly reviewed in this section underlining special characteristics, advantages and drawbacks. More details on the precursors used in this work will be given in paragraph 2.1 and Chapter 4.
An ideal CVD precursor must have the following properties [11]:

- stability at room temperature
- ability to react cleanly in the reaction zone
- sufficient volatility (i.e. high vapor pressure)
- high degree of purity
- ability to react without producing side or parasitic reactions
- react at a temperature lower than the substrate melting temperature
- non toxic or hazardous and environmental friendly compounds
- for patterning, interacting with the irradiation species

Metallo-organics

Metallo-organic or metalorganic precursors contain carbon atoms in the ligands. The advantage is a relative low deposition temperature but on the other hand carbon contamination can be incorporated in the growing film.
We distinguish:

- Alkyls: non polar, volatile, reactive, pyrophoric, toxic
  Trimetyl aluminum $Al(CH_3)_3$
- Acetylacetonates: stable, soluble in organic solvent
  Aluminum acetylacetonate $Al(C_5H_7O_2)_3$
- Alkoxides: water sensitive
  Aluminum isopropoxide $Al[OCH(CH_3)_2]_3$

Halides

They are binary compounds of a halogen and a more electropositive element such as a metal. Halide precursors are reactive and toxic, e.g. Aluminum chloride $AlCl_3$.

1.3.4. Transport

Transport phenomena (gas flow, heat transfer, etc) in CVD processes can influence chemical reactions, film uniformity and impurity level; and they are determined by pressure, temperature gradient as well as reactor geometry. That is the reason why these phenomena will be studied, in Chapter 3, in the particular case of the custom CVD reactor used in this work.
We propose here to define some dimensionless parameters useful in CVD reactor characterization to distinguish the flow regimes of the precursors in the different parts of our HV-CVD reactor [8].

Knudsen number:

$$Kn = \frac{\lambda}{L},$$

where L is a characteristic length of the system and λ is the mean free path.

When $Kn \geq 10$ the system operates in the free molecular flow regime, where wall collisions dominate and the molecules undergo few gas phase collisions.

Reynolds number:

$\mathrm{Re} = \frac{\langle v \rangle L}{\upsilon}$, where υ is the viscosity and $\langle v \rangle$ is the mean fluid velocity

When $\mathrm{Re} \leq 100$ the flows are laminar.

1.3.5. Deposition pressure

In CVD processes the pressure is a key parameter influencing the gas transport, the growth rate, the quality and the microstructure of the thin film.
The pressure range in CVD is divided in four regimes: 1) Atmospheric CVD (1 bar), 2) Reduced Pressure CVD (100-1 mbar), 3) Low Pressure CVD (1-10^{-2} mbar) and 4) High Vacuum CVD ($\leq 10^{-2}$ mbar).
Even if the growth rate is smaller in low pressure CVD, we have a better control of the thickness uniformity, the film properties and the grain size; moreover the step coverage is better. The reason is that at low pressure, there is usually no significant mass transfer control on growth, only chemical reactions kinetic control. So that

uniform accessibility of the wafer surfaces to the reaction can still be maintained even with very close wafer spacing [8]. This offers the possibility to deposit thin films on several wafers in the same time and reactor if temperature uniformity is guaranteed. This multi wafers deposition can reduce the cost per wafer induced by the need of expensive vacuum equipment. On the other hand, in-situ patterning is obviously impossible.

In vacuum conditions the growth performances, the layer uniformity and the composition homogeneity are better controllable by the process conditions. Although the low pressure chemical vapor deposition systems operate at pressure three to four orders of magnitude below those of atmospheric pressure CVD system, the difference in rate of deposition at comparable temperatures is often less than one order of magnitude smaller [8]. HV-CVD allows to minimize impurities incorporation and to eliminate the complexity of vapor phase molecular interactions and reactions present at atmospheric pressure [12]. Indeed, the Knudsen number is higher than ten for high vacuum reactors; this means that no molecule collisions take place in the gas phase due to the large mean free path of the molecules compared to the reactor dimensions. This free molecular beam regime is necessary to guarantee high thickness uniformity in our HV-CVD reactor, as presented in the paragraph 3.3.3.

Another advantage of high vacuum deposition systems is that in-situ characterization or structuration involving electron or ion beam can be performed, as demonstrated in Chapter 6.

1.3.6. Light assisted deposition

Different energy sources are available in CVD technique; we will discuss here the possibilities to use light in order to decompose precursor and form a film on a substrate in CVD regime.

The advantages are:

- Local and pattern deposition
- Deposition at lower temperature
- Local change of film properties (electrical, optical)
- Remove impurities
- Low damage
- Change the crystanillity

Different setup configurations exist and two major physical principles are involved, separately or in the same time, in light induced CVD.

Pyrolytic process

Two main configurations are usually distinguished: parallel and perpendicular irradiation of the substrate.

In the parallel system, the precursor is heated by the laser in the gas phase near the substrate surface. For example, West et al. have deposited titanium silicide films using a CO_2 laser shining parallel to a silicon substrate [13]. The gas mixture composed of SiH_4 and $TiCl_4$ is heated by the laser light because of the slight absorption of the silane and the thermal equilibrium due to molecular collisions; thereby the CVD reaction can take place. Aluminum oxide has also been deposited from trimethylaluminum decomposition by parallel irradiation with excimer laser [14].

In the perpendicular illumination, the energy of a light source is used to locally heat the absorbing substrate, in the range of the decomposition temperature, to induce the chemical reaction. The deposition will only take place where the light illuminates the substrate, which must be absorbent at the illumination wavelength.
The temporal profile of the surface temperature rise can be described in this photo-thermal effect by the heat flow equation in the case of a pulsed laser irradiation [8].

$$\frac{\partial T}{\partial t} = \frac{\alpha}{\rho C_p} I(z,t) + \frac{1}{\rho C_p}\left\{\kappa \frac{\partial T}{\partial z}\right\}$$

Where t is time, z the distance below the surface, α is the absorption coefficient, ρ is the density, C_p is the specific heat and κ is the thermal conductivity.

The laser intensity I(z,t) at distance z into the film is given by $I(z,t) = I_0(1-R)e^{-\alpha z}$

Where $I_0(t)$ is the laser power density at the surface and R is the reflectivity of the interface.

By focusing the beam, usually a laser beam, we can illuminate a very small part of the substrate and by moving the beam we can scan on the substrate and deposit patterns. Selective and local deposition of fine features is thus possible. The same deposition mechanism and chemistry as thermal CVD are involved in LICVD.

Photolytic process

A number of photolytic processes can happen when light is directed at a substrate in presence of a gas. Photodissociation of molecules by light in the gas phase, photodecomposition of molecules adsorbed on a surface and photodissociation of adsorbates from the substrate excitation can take place and are here reviewed.
First, if a gas (AB) absorbs some of the incident light, composed of photons with energy of (hν), we can have [8]:

- *Absorption* $AB + h\nu \rightarrow AB^*$
- *Emission* $AB^* \rightarrow AB^{\times} + h\nu'$
- *Quenching* $AB^* + M \rightarrow AB^{\times} + M^{\times}$
- *Dissociation* $AB^* \rightarrow A + B$

Where AB^* is the excited state, $AB^{\times}$ denotes residual rotational or vibrational energy and M another species.
In that case, the light interacts directly with the molecules in the gas phase. The right combination of light and chemistry must be found in order to deposit the desired film. A good precursor for PACVD has to absorb well the light at a given wavelength.
The absorption of optical radiation by a gas with a density ρ and length L is governed by the Beer-Lambert relation [15]: $I_t = I_i e^{-\rho\sigma L}$ where I_i is the incident intensity, I_t is the transmitted intensity and σ the absorption cross-section.
This relation is true in the case of a single photon absorption by the precursor molecule and is considered valid if the incident intensity is smaller than 10^5 W/cm^2.
In brief, sufficient photon energy is needed to break the chemical bonds in the reactant molecules to induce dissociation and then deposition.

Then the photochemistry on surfaces can induce photodecomposition of adsorbed species on a substrate surface either by direct electronic excitation of the molecules or by excitation of the substrate.
Higashi et al. have demonstrated the photodissociation of $Al(CH_3)_3$ adsorbed on sapphire substrate by 193 nm wavelength irradiation [16].
On the other hand, dissociation of adsorbed molecules can also arise from substrate excitation. This happens by generation of electrons at the surface of the substrate from the light irradiation. This phenomenon has been demonstrated in alumina PACVD [17] as well as by dissociation of oxygen on silver without polarization dependence meaning that the substrate excitation is dominant [18].

Laser irradiation can also enhance or inhibit the nucleation of thin films growth. Physical effect (surface tension) and chemical effect (reaction activation) are both responsible of this nucleation effect [19]. Tsao et al. demonstrated that UV laser photodeposition has been used to predispose surfaces to classical CVD of aluminum from tri-isobutyl aluminum [20]. This technique can be useful for mask-less patterned growth [21].

1.4. Aluminum oxide

The aluminum oxide (or alumina) has the formula Al_2O_3 and can exist under different structural varieties: α, γ, δ, θ, κ, ε, η and χ. In the nature, we can find alumina in bauxite in a hydrated form and mixed with iron oxide, or as pure mineral as crystalline corundum form (α-Al_2O_3); much less-common, rubies and sapphires are gem-quality forms of corundum with their characteristic colors due to metallic trace impurities. Rubies are given their characteristic deep red color by traces of the trivalent chromium. Sapphires come in different colors given by various other impurities, such as iron and titanium ions, replacing Al^{3+} in the oxide.

Pure alumina is generally prepared from the dehydroxylation (Bayer process) of γ-AlO(OH) (boehmite), α-AlO(OH) (diaspore), α-$Al(OH)_3$ (bayerite) or γ-$Al(OH)_3$ (gibbsite).

Alpha alumina has a wide range of technological and industrial applications as a result of its hardness, corrosion resistance and good electrical insulation. However transition alumina can also be useful in some applications: wear resistance (κ-Al_2O_3) [22], bioactive composite (δ-Al_2O_3) [23] or precursor for the production of high purity α-alumina (θ-Al_2O_3) [24].

For a better understanding, the different forms of alumina will be discussed in more detail.

The alpha phase is the only thermodynamically stable oxide of aluminum. Corundum has a trigonal Bravais lattice. The primitive cell contains two formula units of aluminum oxide. The oxygen ions nearly form a hexagonal close-packed structure with aluminum ions filling two-thirds of the octahedral interstices [25].

The other phases are metastable and are usually considered as transition aluminas; γ- and η-Al_2O_3 are structurally cubic, δ-Al_2O_3 either tetragonal or orthorhombic, θ-Al_2O_3 is monoclinic, χ-Al_2O_3 is hexagonal and κ-Al_2O_3 is orthorhombic [25, 26].

Phase	Structure	a (nm)	b (nm)	c (nm)	β (deg)
α-Al_2O_3	hex	0.47589		1.291	
γ- Al_2O_3	cub	0.7911			
θ-Al_2O_3	mon	1.183	0.292	0.564	104
χ-Al_2O_3	hex	0.556		1.344	

Table 2 Crystal structure and lattice parameters of alumina phases [27].

There still exists controversy about the definitive structures of the different alumina phases, but Levin et al. [25] proposed processing routes resulting in formation of different metastable alumina structures and the sequence of phase transformation toward the stable α-Al_2O_3, as illustrated in Figure 4.

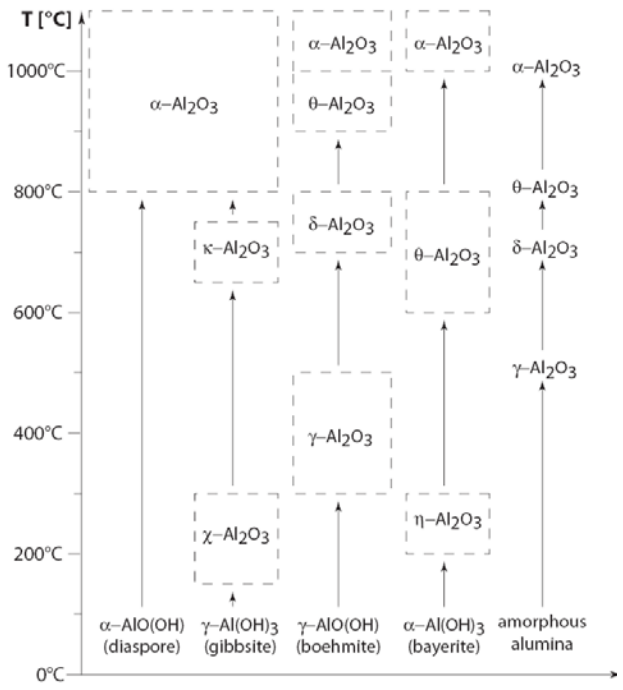

Figure 4 Schematic representation of aluminum oxide phases [25, 28].

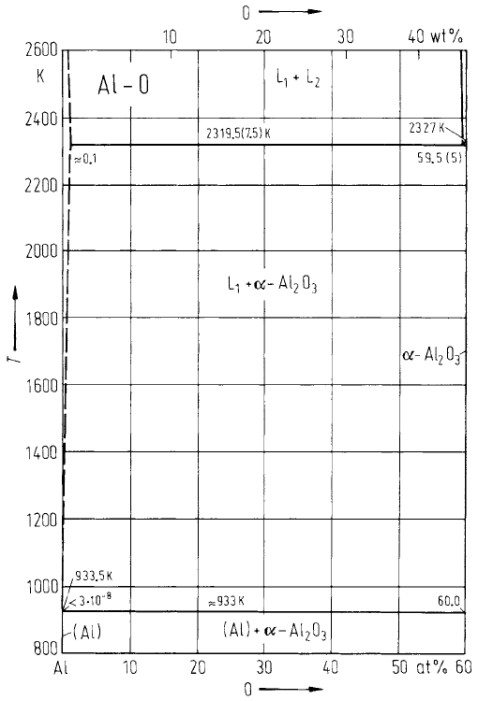

Figure 5 Al-O phase diagram [27].

The aluminum oxygen system illustrated by the phase diagram in Figure 5 confirms that only the alpha phase exists in a stable form.

The principal properties of alumina are listed in Table 3. We differentiate some properties according to the alumina phases. The list is not exhaustive but gathers the properties used in the main applications of alumina thin films.

	Corundum (α-Al_2O_3)	γ-Al_2O_3	Ceramics	Amorphous
Molecular weight (g/mole)	101.961	101.961		
Density ρ (g/cm^3)	3.99	3.97		2 - 3.6
Melting point θ_m (ºC)	2054	Transition to corundum @ 1200 ºC		
Enthalpy of formation $\Delta_f H^0$ (kJ/mol)	-1675.7 @ 298.15 K			
Standard molar entropy S_0 (J/K·mol)	50.92 @ 298.15 K			
Standard molar energy of formation $\Delta_f G^0$ (kJ/mol)	-1528.3 @ 298.15 K			
Molar heat capacity C_p (J/mol·K)	79.0 @ 298.15			
Enthalpy of fusion $\Delta_{fusion}H$ (kJ/mol)	111.1 @ 2054 ºC			
Thermal conductivity λ (W/m·K)	2.6 @ 100 ºC ($\perp$ to c axis)		30 @ 100 ºC 13 @ 400 ºC	
Refractive index n	$n_o = 1.7673$ $n_e = 1.7598$ @ 589 nm	1.7 @ 632 nm		1.51-1.65 @632 nm
Hardness	9 Mohs			1200 HV
Dielectric constant ε	$\varepsilon_{11} = \varepsilon_{22} = 9.34$ $\varepsilon_{33} = 11.54$ @298.15 K			7.7 @298.15 K
Magnetic susceptibility χ_m (cm^3/mol)			$-37 \cdot 10^6$	

Table 3 Alumina properties [25].

In conclusion alumina is a transparent, hard and insulating oxide with relatively high refractive index and its properties can slightly change according to the phases.
Thus, aluminum oxide is a good candidate to be an important material in integrated optics, due to good optical properties and the possibilities to be deposited in thin films.

1.5. Waveguides

1.5.1. Planar waveguide

A planar waveguide is a slab of dielectric material surrounded by media of lower refractive indices. The light is guided inside the slab by total internal reflection. In thin film devices the slab is called film and the upper and lower media are called the cover and the substrate respectively [29].

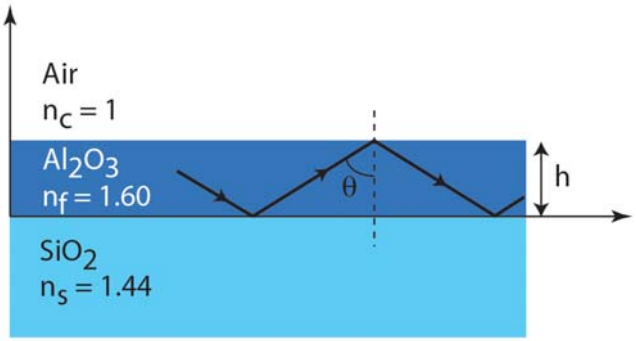

Figure 6 Sketch of an alumina planar waveguide on SiO_2.

Practically, in order to have an asymmetric planar waveguide, we deposited an amorphous alumina thin film on 3 µm SiO_2 buffer layer on top of the silicon substrate, as sketched in Figure 6. Thus, we have a three media structure composed of air on top as cover, the alumina film and the SiO_2/Si substrate, with refractive indices at 670 nm wavelength of $n_c = 1$, $n_f = 1.6$ and $n_s = 1.44$ respectively [30].

In order to guide the light inside the film, total internal reflections have to take place at the boundaries. From the Snell's law, we can determine the two critical angles θ_c and θ_s at the air-film and film-substrate interfaces:

$$\sin\theta_s = \frac{n_s}{n_f} \; and \; \sin\theta_c = \frac{n_c}{n_f}, \text{ where } n_f \geq n_s \geq n_c.$$

The guiding condition is: $\theta \geq \theta_s \geq \theta_c$, where θ is the propagation angle.

The twice reflected wave lags behind the original wave and there is twice phase shift introduced by each internal reflection at each corresponding dielectric boundaries; the propagation mode is given by:

$$h \cdot k \cdot n_f \cos\theta_m - \phi_s(\theta_m) - \phi_c(\theta_m) = m \cdot \pi ,$$

where h is the slab thickness, k is the wave vector, ϕ_s and ϕ_c the phases and m = 0, 1, 2, ...

Due to the smaller index difference between the silicon dioxide and the alumina compared to air/alumina the limiting factor for guiding is θ_s at the interface between SiO_2 and Al_2O_3 ($\phi_s = 0$). So the condition is: $\frac{2\pi \cdot n_f \cdot h}{\lambda}\cos\theta_s \geq \phi_c(\theta_s)$

For TE_0 and TM_0 (fundamental mode) the cut-off wavelength is expressed as:

$$\left(\frac{h}{\lambda}\right)_0 = \frac{1}{2\pi\sqrt{n_f^2 - n_s^2}} \arctan\sqrt{a_{E,M}}$$

where for TE: $a_E = \frac{n_s^2 - n_c^2}{n_f^2 - n_s^2}$ and for TM: $a_M = \frac{n_f^4}{n_c^4} a_E$

For the higher order modes we have: $\frac{2\pi \cdot n_f \cdot h}{\lambda}\cos\theta_s \geq \phi_c(\theta_s) + m \cdot \pi$ and the cut-off for TE_m and TM_m is: $\left(\frac{h}{\lambda}\right)_m = \left(\frac{h}{\lambda}\right)_0 + \frac{m}{2\sqrt{n_f^2 - n_s^2}}$

1.5.2. Channel waveguide

A channel waveguide is a waveguide that confines light in the two transverse directions.

There exists different kind of channel waveguides. We differentiate (see Figure 7) (a) the strip with a delimited, in two directions, band of higher refractive index on top of a substrate, (b) the embedded strip where the higher refractive index part is buried in the substrate, (c) the rib where the channel structure is on top of the same material on a substrate and (d) the strip loaded with a delimited band on material on top of a higher index material on a substrate.

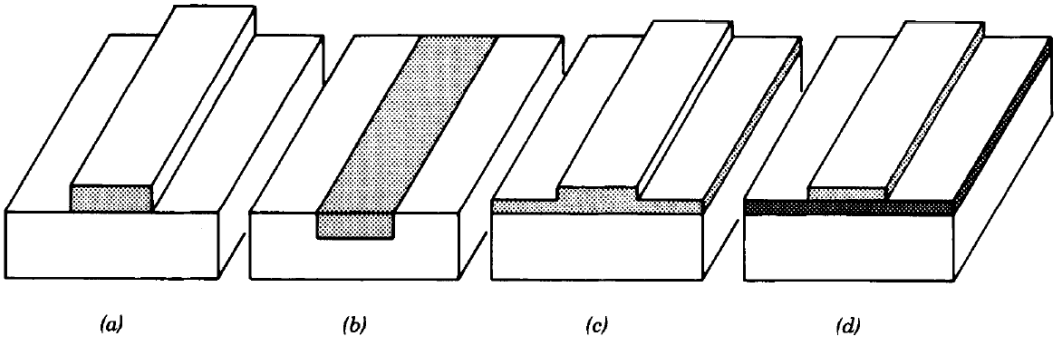

Figure 7 Various types of waveguides geometries: (a) strip, (b) embedded strip, (c) rib or ridge and (d) strip loaded. (the darker the shading, the higher the refractive index) [29].

1.6. Motivation of this thesis

In the future, the production of integrated optical devices will need the production of fast, cheap, reliable, large surface and good quality thin films.
High Vacuum Chemical Vapor Deposition (HV-CVD) can offer these characteristics but this new deposition technique for transparent oxide is not yet completely studied. This is the reason why we propose in this work to analyze the feasibility to deposit alumina thin films by this technique and to understand better the limitations.
For this purpose a new specific reactor is needed to deposit thin films with high thickness uniformity and to have enough flexibility in the parameters variation in order to test a wide range of conditions. Our aim is to have a versatile HV-CVD system oriented in an industrial way which allows studying the growth behavior of alumina in specific conditions. The main motivations are first to prove the opportunity to form good quality thin films with competitive growth rate in HV-CVD, secondly to have an overview of the limitations of this technique and finally to demonstrate potential applications from the deposited alumina films by HV-CVD.

1.7. Structure of the script

Chapter 2 is a literature survey. First the chemical vapor deposition of alumina thin films is presented in function of the different precursors used during the last 20 years. Then a brief review of the different possibilities to deposit alumina layers by Plasma Enhanced CVD and Light induced CVD is summarized. Alternative methods as Atomic Layer Deposition and Sol Gel are reported as well. Finally, the main

applications of alumina thin films are listed with emphasis on optical applications as for instance waveguides.

In Chapter 3, the High Vacuum Chemical Vapor Deposition (HV-CVD) experimental setup is presented in detail. The performances to achieve and the final design of the deposition system are reported. The heating system and the gas delivery system are described more carefully. Indeed, the original design of the effusing source allows depositing films with high thickness uniformity. The simulations and the measurements of the thickness distribution are discussed. Finally the different characterization setups used during this work are described.

Chapter 4 reports the main properties of the precursor, aluminum isopropoxide (ATI), used to the deposit the alumina thin films. The thermal behavior and the aging effect of ATI are presented.

In Chapter 5 a complete study of the deposition of alumina thin films by HV-CVD is shown. Growth behavior, chemical composition, optical characterization and structure analysis are studied in function of the different deposition conditions. Rare earth doping of alumina is also reported by co-deposition of alumina and erbium.
248 nm Excimer laser induced CVD of alumina is presented in Chapter 6 and the irradiation parameters influence, such as fluence and repetition rate, on the alumina growth is investigated. Local alumina microstructures are deposited in situ by this mean. Assisted electron beam CVD of alumina is reported and compared to thermal deposited and laser induced alumina.

Finally in the Chapter 7 are presented the optical applications resulting of the alumina thin films deposition. Planar and channel waveguides are fabricated and briefly characterized, some results of optical waveguiding are presented. The feasibility of nanostructuration of alumina in order to create integrated optical devices is demonstrated with the realization of Bragg grating and nano-holes array on channel alumina waveguide.

Chapter 8 summarizes the main results obtained in this work and proposes guide lines for future research. High Vacuum Chemical Vapor Deposition assisted by external beam could produce, in the future, integrated optical devices on large substrate and in an industrial oriented way.

Chapter 2 State of the art

2.1. Chemical Vapor Deposition of alumina thin films

The aim of this paragraph is to give an overview of the different possibilities to deposit alumina thin films by CVD processes. We decided here to present a literature survey classified by energy source and by precursors with emphasis on thermal CVD and aluminum isopropoxide and to focus on the films applications in the paragraph 2.4.

2.1.1. Thermal CVD

Aluminum tri-isopropoxide $Al[OCH(CH_3)_2]_3$ (ATI)

Aboaf in 1967 is the first to report amorphous alumina thin film deposition by thermal CVD of Aluminum tri-isopropoxide at atmospheric pressure [31]. ATI cracks at 250 °C in oxygen and a growth rate of 10 nm/min at 420 °C is obtained on silicon substrates.
From the seventies, low pressure chemical vapor deposition of alumina from thermal composition of ATI has been studied and a decomposition reaction is proposed [32].

$$2\,Al(C_3H_7O)_3 \rightarrow Al_2O_3 + 3\,C_3H_7OH + 3\,C_3H_6$$

Saraie et al. proposed the same experiments as Aboaf under 10 mbar reduced pressure [33]. The films deposited between 250-420 °C were amorphous with a maximum growth rate of 17 nm/min and activation energy of 76.2 kJ/mol. In another work [34], Saraie et al. deposited, in low pressure conditions, alumina films with OH group incorporation at 170 °C in presence of water but concluded that a substrate temperature higher than 370 °C is desirable to obtain high quality film. He also found that the activation energy is 79.9 kJ/mol in nitrogen, 18.8 kJ/mol in nitrogen and oxygen mixture, and 14.7 kJ/mol in nitrogen and hydrogen mixture.
Then Morssinkhof et al. [35] studied in more detail the amorphous alumina deposition process reaching a maximum growth rate of 40 nm/min at 420 °C. They also underlined the different CVD regimes by measuring an activation energy of 30 kJ/mol in the chemical reaction limited regime and a transition temperature between the chemical reaction limited regime and the mass transport limited regime of 420 °C.
Gamma phase alumina deposited by LPCVD at 750 °C on Si is reported by Yom et al. [36].

In 2000 Niska et al. [37] published the deposition of alpha crystalline phase alumina in oxygen at 1100 ºC and proposed a decomposition reaction:

$$2\,Al(C_3H_7O)_3 + 27\,O_2 \rightarrow Al_2O_3 + 18\,CO_2 + 21\,H_2O$$

Finally, corundum alumina (alpha) has been deposited on metallic substrates at 1080 ºC in excess of oxygen facilitating the formation of dense films [38].

Triethyl(tri-sec-butoxy)dialuminum $(C_2H_5)_3Al_2(OC_4H_9)_3$ (ATSB)

ATSB is used in 1987 by Kodas et al. to produce alumina powder [39].
The first report of atmospheric pressure CVD alumina film formation, in 1993 by Haanappel et al., shows amorphous films deposited in the temperature range of 290 to 420 ºC with an activation energy of 83 kJ/mol [40, 41].
Kuo et al. studied the thermal decomposition of ATSB in low pressure CVD conditions between 300 and 500 ºC. The maximum growth rate was 23 nm/min and the activation energy was in the range of 8 to 12 kJ/mol [42].

Aluminum acetylacetonate $Al(CH_3COCHCOCH_3)_3$ (Al-acac)

One of the first deposition of alumina by pyrolysis of Al-acac was demonstrated at about 420 ºC by Ajayi et al. [43]. In the beginning of the nineties, Maruyama et al. [44] studied more in detail the alumina chemical vapor deposition from aluminum acetylacetonate. The lower limit of the reaction temperature was 250 ºC and the activation energy was 28 kJ/mol. The maximum growth rate reached for this amorphous alumina was about 9 nm/min at 600 ºC.
Amorphous alumina LPCVD from Al-acac on silicon substrate was demonstrated by Kim et al. [45] between 230 ºC and 330 ºC with a maximum growth rate of 5 nm/min. The addition of water vapor improves the deposition rate and the activation energy is 17.3 kJ/mol [46].
Based on the thermal decomposition of this metallo-organic precursor, Pradhan et al. showed that a mix of kappa and gamma crystalline phase alumina can be deposited at 950 ºC [47].
Almost all the authors reporting on alumina thin film deposition by Al-acac pyrolysis noticed carbon contamination as problem.

Trimethylaluminum $Al(CH_3)_3$ (TMA)

In 1988, Ishida et al. deposited epitaxial γ-Al_2O_3 in LPCVD from the thermal decomposition of TMA in N_2O at 950 ºC on silicon wafer. The growth rate was 7 nm/min [48]. Kimura et al. [49] proposed the same process but in Ultra High Vaccum (UHV) environment in order to improve uniformity and control of the film growth. In these conditions the growth rate decreased to 0.3 nm/min. In another paper they demonstrated the alumina thin film deposition from TMA in oxygen with a growth rate of 2 nm/min [50].

Aluminum chloride $AlCl_3$

Aluminum oxide films were produced, in 1971, from the hydrolysis of aluminum chloride by Kamoshida [51]; the films were amorphous under 700 ºC and polycrystalline above 800 ºC. Chlorine contamination was measured.
Aluminum oxide films were deposited from vapor phase by reaction of $AlCl_3$ with CO_2 and H_2 onto silicon substrate between 400 ºC and 1000 ºC as described by Iida [52]. Activation energy for this reaction was 56.7 kJ/mol and the deposition rate at 420 ºC was 1.5 nm/min. A hydrolysis reaction is also proposed:

$$CO_2 + H_2 \rightarrow H_2O + CO$$
$$2\,AlCl_3 + 3\,CO_2 + 3\,H_2 \rightarrow Al_2O_3 + 3\,CO + 6\,HCl$$

Increasing the temperature to 1027 ºC, Kim [53] succeeded to form α-Al_2O_3 and the activation energy was 146.5 kJ/mol.

Aluminum ethylhexanoate $Al(C_7H_{15}COO)_3$ (AEH)

From the thermal decomposition of aluminum ethylhexanoate in atmospheric pressure CVD, amorphous alumina can be deposited on silicon substrate at temperature in the range of 480 ºC to 700 ºC [54]. The activation energy is 28.1 kJ/mol and the maximum growth rate is 12 nm/min.

Aluminum tris(tetramethylheptanedionate) $Al(OCC(CH_3)_3CHCOC(CH_3)_3)_3$

Ciliberto et al. used this precursor to deposit amorphous Al_2O_3 with low content of carbon impurities in a LPCVD reactor [55].

Aluminum tris(tetrahydroborato) $Al(BH_4)_3$

Aluminum oxide has been prepared from the LPCVD (background pressure of 10^{-6} Torr) of volatile boron containing precursor material admitting a small partial pressure (10^{-3} Torr) of oxygen [56].

2.1.2. Plasma enhanced CVD

As this technique is not used in this work, only a short overview is given.

Aluminum chloride $AlCl_3$

Transparent amorphous alumina can be deposited at 300 ºC by means of 13.56 MHz discharge in $AlCl_3$, H_2 and CO_2 mixture with a maximum growth rate of 3.3 nm/min [57]. The effect of residual stress of alumina on glass is studied [58].

Trimethylaluminum $Al(CH_3)_3$ (TMA)

Meiners deposited, in 1983, alumina at 375 ºC from TMA and oxygen excited in RF plasma [59]. Low temperature (250 ºC) deposition of Al_2O_3 layers was achieved in PECVD with DC excited plasma, the growth rate was 35 nm/min [60].
Aluminum oxide films were deposited on Si substrate at lower temperature (150 ºC) by PECVD method using TMA and N_2O gases. The film structure is amorphous and the growth rate 40 nm/min [61].

2.1.3. Light induced CVD

Trimethylaluminum $Al(CH_3)_3$ (TMA)

In 1983, Solanki et al. presented aluminum oxide photodepostion from TMA and N_2O on silicon [14]. The KrF excimer laser irradiation was parallel to the substrate with a 248 nm wavelength and an average power of 10 W. The growth rate was 200 nm/min for 200 ºC substrate temperature. Then Ishida et al. demonstrated the formation of alumina on Si by photolysis of TMA and N_2O at room temperature under direct irradiation of 193 nm ArF excimer laser [62].

Aluminum tri-isopropoxide $Al[OCH(CH_3)_2]_3$ (ATI)

Al_2O_3 thin films photo CVD from ATI and oxygen by perpendicular illumination of Hg lamp (185 and 245 nm) is demonstrated by Saraie et al. for the first time in 1990 [63]. A maximum growth rate of about 10 nm/min at 260 ºC is obtained and 6.3 kJ/mol activation energy is measured, more than 3 times smaller than for thermal CVD. In the continuation of this study, Fukushima et al. suggested that due to the small absorption by the ATI and O_2 molecules, UV photons are absorbed in the Al_2O_3 film, and photo-generated electrons and holes play some role in enhancing deposition reactions on the surface, such as photocatalytic effect [17].
ATI vapor does not show strong absorption for the UV light from the Hg lamp (185 nm) in consequence they focused on D_2 lamp (125 and 160 nm) for the photo deposition of alumina from aluminum isopropoxide [64]. Films with 1.65 refractive index were obtained at 260 ºC, clearly larger index than with thermal CVD even at 400 ºC.

Other precursors

Hudson et al. deposited alumina from the photo-deposition of home made precursor ($Al(OCH(CH_3)_2$ Acac); the maximum growth rate was 250 nm/min under direct illumination of doubled argon laser or Xe-Hg lamp [65].

2.2. Atomic Layer Deposition of alumina thin films

As this technique is not used in this work, only a short overview is given.

Trimethylaluminum $Al(CH_3)_3$ (TMA)

In 1989, Higashi et al. proposed a sequential surface chemical reaction growth technique to make Al_2O_3 dielectric films on Si at temperature as low as 100 ºC [66]. TMA and water are used as precursors and the growth rate was low 0.3 - 0.6 nm/min. Fan et al. increased the growth rate (0.11 nm/cycle) of alumina on GaAs at 150 ºC using H_2O_2 and TMA [67]. Soto proved in 1991 that alumina can be deposited at room temperature from TMA and water in UHV conditions [68]. Then Kumagai et al. used N_2O as reactive agent and reached a growth rate of about 4 nm/cycle on Si at 500 ºC [69].

More recently, Al_2O_3 ALD growth has been demonstrated at temperature as low as 33 ºC on thermally fragile substrate such as organic, polymeric or biological material [70]. Alumina ALD coated PET (polyethylene terephthalate) bottle to lower CO_2 gas diffusion is illustrated as application. Gas diffusion tests with CO_2 were carried out on PET bottles coated with Al_2O_3 ALD films. Bottles were coated with 300 reaction cycles of Al_2O_3 ALD at 58 °C. This coating procedure should deposit Al_2O_3 ALD film with a thickness of 360 Å. The CO_2 gas diffusion test revealed a CO_2 loss rate of 1.55% per week, or 2.91 $cm^3/(day\ bar\ cm^2)$. This CO_2 loss rate for the Al_2O_3 ALD-coated bottle is a factor of 1.6 lower than the CO_2 loss rate of an uncoated PET bottle.

Aluminum chloride $AlCl_3$

Aluminum oxide was deposited using atomic layer deposition from aluminum chloride and water at 300 ºC on glass [71]. Ritala et al. deposited alumina thin films by ALD from $AlCl_3$ and H_2O on glass at 500 ºC for optical applications, such as anti-reflection coatings [72].

Dimethylaluminum chloride $Al(CH_3)_2Cl$ (DMACl)

Amorphous aluminum oxide thin films were deposited by ALD via sequential surface reactions in the temperature range of 95-500 ºC using DMACl and H_2O with a maximum growth rate of 0.08 nm/cycle [73].

Tris(diethylamino) aluminum $Al[N(C_2H_5)_2]_3$ (TDEAA)

ALD of TDEAA and water allows to deposit alumina between 200-400 ºC with a growth rate of 0.14 nm/min [74].

2.3. Summary of alumina thin films deposition

Chemical process		Precursor	Note	T min [°C]	T max [°C]	Growth rate [nm/min]	E_a [kJ/mol]	Phase	Ref.
CVD	Thermal	ATI	Atm. pressure	250	420	10	-	am	[31]
		ATI	Low pressure	-	420	40	30	am	[35]
		ATI + H_2O	Low pressure	170	-	-	-	am	[33]
		ATI + N_2	Low pressure	250	420	17	76.2	am	[34]
		ATI + O_2					18.8		
		ATI + H_2					14.7		
		ATI + N_2O	Low pressure	200	750	-	-	γ	[36]
		ATI + O_2	Low pressure	-	1100	-	-	α	[37]
		ATSB	Atm. pressure	290	420	-	83	am	[40]
		ATSB	Low pressure	300	500	23	12	am	[42]
		Al-acac	Atm. pressure	250	600	9	28	am	[44]
		Al-acac + H_2O	Atm. pressure	230	330	5	17.3	am	[46]
		Al-acac	Atm. pressure	-	950	-	-	γ	[47]
		TMA + N_2O	Atm. pressure	-	950	7	-	γ	[48]
		TMA + N_2O	UHV	-	950	0.3	-	γ	[49]
		$AlCl_3$ + CO_2 + O_2	Atm	400	1000	1.5	56.7	γ	[52]
		$AlCl_3$ + CO_2 + O_2	Atm. pressure	-	1027		146.5	α	[53]
		AEH	Atm. pressure	480	700	12	28.1	am	[54]

		Al (TMHD)	Low. pressure	-	600	-	-	am	[55]
	Plasma	$AlCl_3$ + CO_2+ H_2	14 MHz	300	-	3.3	-	am	[58]
		TMA + O_2	RF plasma	250	-	35	-	am	[60]
		TMA + N_2O	-	150	-	40	-	am	[61]
	Laser	TMA + N_2O	193 nm laser	RT	-	200	-	am	[62]
		ATI + O_2	Hg lamp	260		10	6.3	am	[63]
ALD		TMA + H_2O	-	100	-	0.6	-	am	[66]
		$AlCl_3$ +H_2O	-	300	-	-	-	am	[71]
		DMACl + H_2O	-	95	500	0.08 nm/cycle	-	am	[73]
		TDEAA + H_2O	-	200	400	0.14	-	am	[74]

Table 4 Summary of alumina thin films deposition (am = amorphous).

In order to deposit amorphous alumina of good optical quality, HV-CVD seems to be the most promising technique combining high growth rate and high film quality. ALD is slower and more complicated technique. Thin films deposition by CVD can be performed with the help of external beam to induce local structure; it is a real advantage in the implementation of one step procedure for optical devices fabrication. The activation energy of the chemical reaction can be usually decreased by the addition of a reactive gas and, in the same time, that reduces the potential contamination coming from metallo-organic precursors.

2.4. Applications of alumina thin films

Alumina thin films can be useful in a wide range of applications. Different alumina properties are exploited, as for example insulating material, transparent oxide, chemical stability and hardness. We listed here the main applications we can find at present in research and development and some of them are commercially available.

Applications	Properties	Functions	Ref.
Cutting tool	- Wear resistance - High hardness - Chemical stability - Thermal stability	Protective coating	[22]
Humidity sensor	Surface conduction	Intermediate layer in SOI	[75]
Pressure sensor	- Etch stop layer - Electrical insulator	Intermediate layer in SOI	[76]
Optical waveguides	High refractive index	Guiding film	[77]
MOSFET	-Low permeability to ions - High dielectric constant - Radiation resistance	- Passivation layer - Diffusion barrier - Gate insulator	[78, 79]
Gas separator	Hydrogen permselectivity	Membrane	[80]
Steel protection against corrosion and oxidation	- Chemical stability - Thermal stability	Protective coating	[41, 81]
Protective coating for solar cells	Refractive index	Protective coating	[82]
Radio valve heater	High dielectric strength	Intermediate layer	[83]
Control sensor for aerospace	- Electrical insulator - High temperature	Intermediate layer	[37]
Planar waveguide	- High refractive index - Low attenuation	Guiding film	[84]

Er doped alumina waveguide	- Low optical loss - High refractive index - Good host for doping	Active guiding film	[85, 86]
Anti reflection coating and filter	- High refractive index	Transmitting film	[72]

Table 5 Applications of alumina thin films.

The alumina thin films are useful in a large range of applications covering different fields; however we propose here to focus on the optical applications which correspond to the aimed goal of this work.

Dielectric thin films are widely employed in various optical devices, such as filters and antireflection and high reflection coatings. The performance of these devices is based on interference effects, and their spectral properties are tailored by constructing film stacks of two or more different materials.
Using ZnS and Al_20_3 as high and low refractive index materials respectively, antireflection coatings, neutral beam splitters, high-reflection coatings and Fabry-Perot filters can be prepared for 580 nm wavelength [72].

For films to be used in integrated optical circuits as waveguide the most important characteristics are the optical attenuation and the refractive index of the films, as well as the stability and the production tolerances of the refractive index and the film thickness. The acceptable attenuation is dependent on the size of a circuit and its typical application, nevertheless attenuation of 1 $dB \cdot cm^{-1}$ or less is desirable.
The sandwich structure $SiO_2/Al_2O_3/SiO_2$ is an attractive waveguide because of the good optical contrast, the stability of the oxide, the possibility of prism coupling; and the fact that attenuation can be reduces down to 1 $dB \cdot cm^{-1}$ by adjusting the deposition conditions and annealing [77].

Erbium doped alumina optical waveguides offer a means for optical amplification or compensation for the losses present in passive integrated optical circuits.
Ridge-type waveguides were formed on 2 μm thick Al_2O_3 films on 5 μm thick plasma-enhanced chemical vapor deposition grown silica film (used as cladding) on silicon substrate [87].

The different applications realized during this work and based on alumina thin films deposited by HV-CVD are presented in Chapter 7.

2.5. Summary and conclusion

Thermal CVD of alumina is possible in a large range of conditions and from many different precursors. Carbon contamination can be a problem for the decomposition of metallo-organic precursors, especially for aluminum acetylacetonate. The crystallization of alumina appears usually above 800 ºC and amorphous alumina is deposited at lower temperature. Typical CVD growth rate of alumina is 1 to 40 nm/min.

External source of energy, such as plasma or light, can decrease the deposition temperature and can be useful for temperature sensitive substrate. Higher growth rate is also usually obtained.

Atomic Layer Deposition is somehow close to high vacuum CVD (molecular beam) but is a very slow process (usually 0.1 to 0.3 nm/min) and high thickness uniformity on large substrate is difficult to obtain.

Alumina is useful in wide range of applications due to the transparency, hardness, insulating and chemical stability properties. But the properties depend strongly on the deposition conditions.

High Vacuum Chemical Vapor Deposition is not well studied and electron beam assisted CVD is not reported in the literature. This new process is somewhere between CVD and ALD processes and is promising technique for large and uniform thin films deposition.

Chapter 3 Experimental setup

3.1. Performances to achieve

Prior to this work only a very preliminary study of HV-CVD of TiO_2 existed [88]. In this work the high potential of performances of HV-CVD were discovered, but no systematic study of the limits or limitations of processing windows was achieved.
Here, we propose the design, construction and testing of a new HV-CVD reactor to explore the possibilities to deposit alumina thin films by this technique and to investigate, by varying a large set of parameters, the limitations in term of deposition and films quality.

High Vacuum Chemical Vapor Deposition can theoretically deposit good quality alumina thin films with high thickness uniformity on large area and with the possibility to structure in situ the deposit. That is the reason why we selected this deposition technique. Therefore, we need high-tech machine able to produce reliable layers in controlled conditions. In addition to the special features needed to guarantee high thickness uniformity and in situ structuration, this new reactor is designed in an industrial orientation, including automation and partial computer assisted control. We have first to guarantee high vacuum ($< 10^{-6}$ mbar) in the reactor. The substrate has to be heated at high temperature (ideally 1000 °C). Then a special design of the gas distribution system is needed to assure high thickness uniformity (> 95%) of the film on the substrate. Direct access to the substrate through a window from the bottom of the machine is necessary to illuminate the substrate with an external beam; smaller is the distance window-substrate, easier will be the film structuration. Finally, different parts of the machine must be able to be heated at a given temperature (~ 150 °C) to avoid precursor condensation. Taking care of all these specifications, the final machine design is presented in the following sections. The technical drawings of the different machine parts and some more details are in appendix 9.1.

3.2. HV-CVD reactor design

3.2.1. Vacuum chamber

The body of the HV-CVD machine is the reactor, composed of a stainless steel cylindrical reactor with 13 ConFlat (CF) flanges. The bottom opening allows connecting the effusing source (see 3.2.3), while the heating unit is attached on top (see 3.2.2).

A schematic representation of the pumping system is represented on Figure 8. The chamber is pumped by a two stages system composed of a primary pump and a turbo molecular pump. The primary vacuum is obtained by a BOC Edwards rotary vane pump and high vacuum is reached with the help of a BOC Edwards turbo molecular pump (540 l/s N_2). The primary pump can be protected from contamination by a liquid nitrogen (LN_2) trap.
A circular liquid nitrogen cryopannel surrounding the substrate participates to the pumping efficiency by trapping the precursor molecules that do not reach the substrate and the by-products resulting of the chemical reaction in the process. It preserves the pumping system from contamination and, above all, avoids that the desorbed molecules contribute in the deposited film.

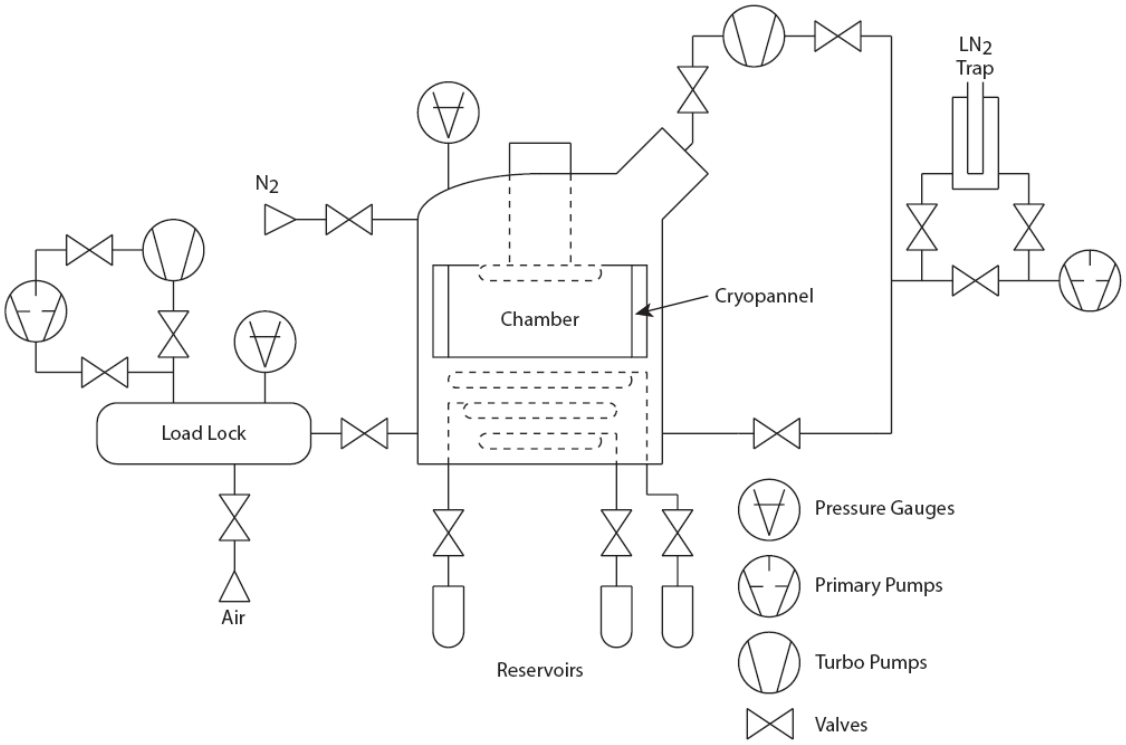

Figure 8 Pumping system.

The combination of the pumping unit and the croypannel guarantees a high vacuum during deposition; in other words the precursor transport is in the molecular beam regime, which is necessary to have a high uniform molecules distribution on the substrate, as presented in paragraph 3.3.3. Then, one flange is dedicated to pressure measurement with a BOC Edwards wide range gauge (10^{-9}-100 mbar). The typical background pressure obtained in the reactor is about 10^{-7} mbar. The quality of the background vacuum (after backing) has been characterized with a Residual Gas Analyzer (RGA) with a measurement range of 0 to 64 amu, showing the possible presence of H_2 and N_2 partial pressure but no H_2O.

On the sidewall of the machine 160 CF flange connects the reactor to a load lock for the substrate transfer and loading. The load lock is individually pumped by a BOC Edwards rotary vane pump and BOC Edwards turbo molecular pump (220 l/s N_2). The remaining flanges are dedicated to vent the chamber with nitrogen, two windows to observe the inner part and finally to connect analysis tools, as Residual Gas Analyser (RGA) for instance.

The reactor wall can be heated up to 120 °C with heating band installed around to desorb the precursor molecules.

3.2.2. Substrate heating and vertical motion

The heating system and the substrate holder are designed to hold four inch wafers. A mechanical system allows moving the substrate in the vertical direction on about five centimeters. This vertical range enables to place the substrate at the correct distance from the effusing source for a uniform distribution of the precursor molecules on the surface substrate, see paragraph 3.3.3. The substrate, during deposition, is maintained between the molybdenum heating block and a counter piece, called horse shoe.

The substrate is heated by conduction and radiation of the heating block, which is inductively heated by Power Cube inductive system delivered by CEIA. All the details about heat transfer to the substrate and reached temperature are discussed in paragraph 3.3.1.

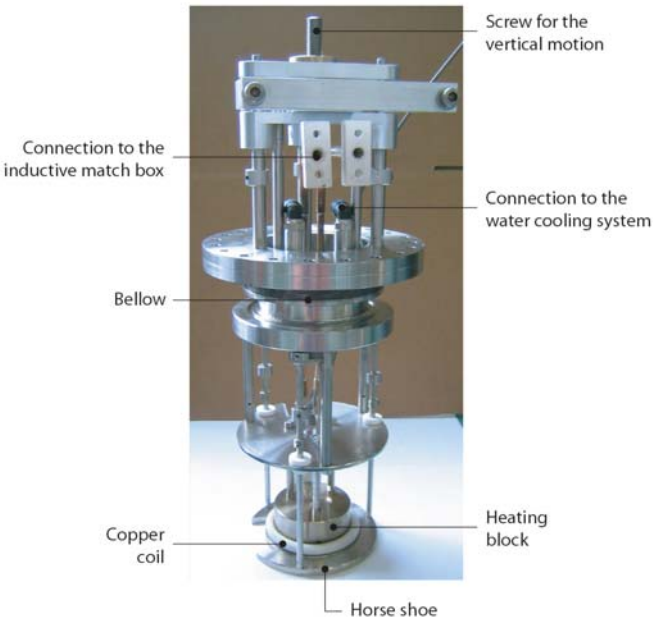

Picture 1 Heating system.

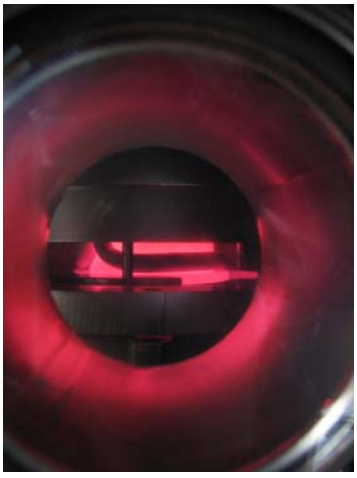

Picture 2 Mo block heated at about 600 °C in high vacuum.

To resume, the heating system is composed of a molybdenum heating block that is inductively heated. Indeed, a one spire copper coil is placed around the heating block then an alternative current passes through the copper piece and induces Eddy current in the molybdenum. These currents lead to resistance heating of the metal by Joule effect. The maximum temperature of the heating block is 1100 °C. The limitations are the inconel shielded thermocouple and some mechanical stainless steel pieces; indeed overheating will result in serious damages on the heating system.

3.2.3. Gas transport

To induce a CVD process we need to transport the precursor to the reaction zone. In our HV-CVD machine, no carrier gas is used; only the precursor vapor is transported to the substrate by the pressure difference between the vacuum chamber and the precursor reservoir. The difference between the background pressure in the reactor and the vapor pressure of the chemical compound at a given temperature induces a precursor flux oriented in the direction of the substrate due to the special geometry presented on paragraph 3.3.3.

First the precursor is stocked in a glass reservoir that can be heated up to 150 °C. Then the precursor is transported through four millimeters inner diameter stainless steel tube resistively heated 10 °C higher (maximum 200 °C) than the reservoir to avoid condensation on the wall. The regulation of the precursor flow with temperature is not reliable due to vapor pressure variation versus time, see paragraph 4.2.

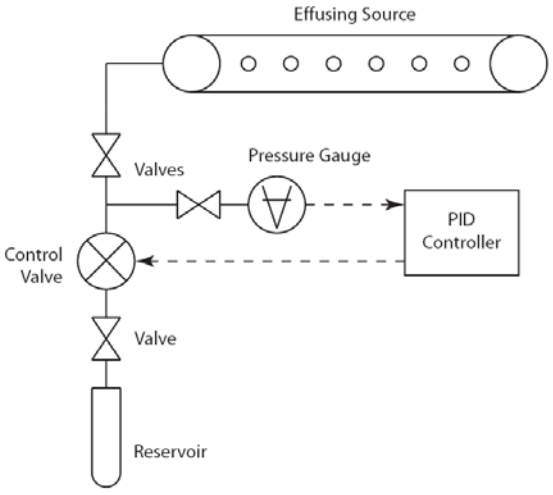

Figure 9 Gas line.

Therefore, in order to guarantee a constant flux, the pressure in the gas line is regulated with a servo valve piloted by a Proportional Integral Derivative (PID) regulator with a given pressure set point, see Figure 9.

The system is composed of MKS heated baratron 631B (10^{-3}-10 mbar) to measure the pressure in the line and MKS control valve 148J to regulate the pressure; the performance of the setup is described in paragraph 4.2. Note that Brooks mass flow

controller (0-10 Standard Cubic Centimeter per Minute or sccm) regulates the flux when an ideal gas is used, for example oxygen.

Picture 3 Effusing source composed of three rings and connecting pipes.

Picture 4 Detail of the three rings and of the 500 µm holes of the effusing source.

Finally the precursor reaches the effusing source that distributes the precursor through twenty-five holes in a way to cover the substrate with high uniformity.
The effusing source is composed of three independent rings connected on individual gas line similar to the one presented above. In this manner, we have the possibility to transport three different precursors in direction of the substrate by three independent ways. Besides to deposit thin films with high uniformity on wafer scale, the advantage of this ring geometry is to liberate some space under the substrate to connect an external beam to induce local deposition.
One ring is composed of 10 millimeter inner diameter pipe connected to the gas line.

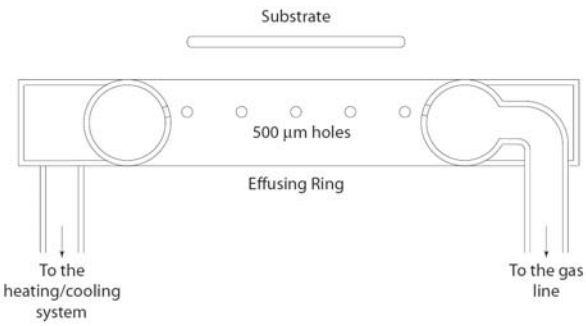

Figure 10 Schematic view of ring effusing source.

Twenty-five holes (500 µm diameter) on the ring are oriented in direction of the substrate under 78°, 53° and 35° angle for the upper, middle and lower ring respectively. The combination of all the holes, the diameter of the ring and the distance between this latter and the substrate guarantee a uniform distribution of molecules precursor on the substrate surface as well as high impinging rate of precursor.
The rings diameter are 181 mm, 158 mm and 135 mm for the upper, middle and lower ring respectively.

The wall around each orifice must be as thin as possible to guarantee a perfect effusion following a cosine law as explained in detail in paragraph 3.3.3; practically the vicinity of each hole is machined to be as thin as possible, in the range of 250 µm.

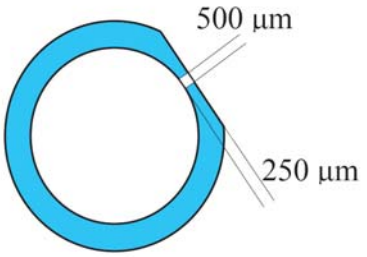

Figure 11 Detail of a hole.

The details of the gas distribution, based on Knudsen theory, are presented and simulated in paragraph 3.3.3. Each ring has a double wall; thereby a cooling or heating circulating liquid (silicone oil) can control the effusing source temperature. The three rings can be heated to avoid precursor condensation or cooled to prevent precursor decomposition in the tubes if the substrate overheats by radiation the effusing source. The possible temperature range of the effusing source is -20 to 175 °C for room temperature environment and is controlled by a Huber Unistat thermoregulator.

3.2.4. In situ reflectometry

For some applications, a perfect control of the thin film thickness is needed, furthermore, in a research and development context, it can be really useful to follow the growth in real time to ensure that deposition take place, to study in situ the influence of some parameters or to verify if the rate is constant or not.

For theses reasons we developed an in situ system able to measure in real time the growing behavior of the films in the HV-CVD system.

The measurement system is based on reflectometry. Indeed a 632.8 nm wavelength HeNe laser illuminate the substrate under an angle of 15° and the reflected light is detected on a photodiode (Gentec PH100 Serie), see Figure 12.

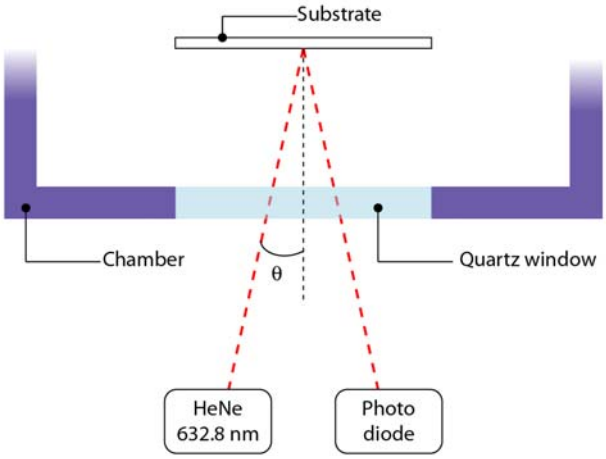

Figure 12 Sketch of the reflectometry setup.

The periodical variation of the measured intensity is proportional to the thickness of the film. The thickness d can be expressed as: $d = \frac{\lambda \cdot \cos\theta}{2n \cdot T} t$, where λ is the

wavelength, θ is the incident angle, n is the refractive index of the film, t is the deposition time and T the period of the intensity signal.
In order to control the thin films growth process, the in situ reflectometry signal can be fitted in real time with the relation (R) presented below [89]. In this way, the refractive index and the thickness of the layer can be calculated during the process. These approximated values can be very useful to control perfectly the thickness and the refractive index of the layer. Indeed, many optical applications, as anti reflection coatings which are constituted of several layers of given thicknesses and indices, need a perfect control of the optical properties of the deposited material.

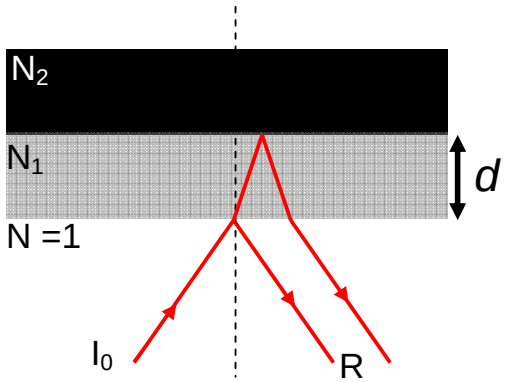

Figure 13 Reflectometry system for a thin film deposited on a substrate.

The normal incidence reflection coefficient R for bilayer system made of a film of thickness d and refractive index $N_1 = n_1 + k_1$ growing on a substrate of refractive index $N_2 = n_2 + k_2$ is given by: $R = R_a R_a^*$ (R)

Where $R_a = \frac{r_{01} + r_{12} \cdot e^{(-2id\beta)} \cdot e^{(-\alpha d)}}{1 + r_{01} r_{12} \cdot e^{(-2id\beta)} \cdot e^{(-\alpha d)}}$, $r_{ij} = \frac{(N_i - N_j)}{(N_i + N_j)}$, the absorption coefficient $\alpha = \frac{4\pi \cdot k_1}{\lambda}$, the phase angle $\beta = \frac{2\pi \cdot n_1}{\lambda}$ and λ the wavelength of the light source.

The equation (R) is fitted using Matlab software for the parameters n_1, k_1 and d according the recorded signal on the photodiode. In Graph 1, the recorded signal and the fit are represented with black circles and red line, respectively.

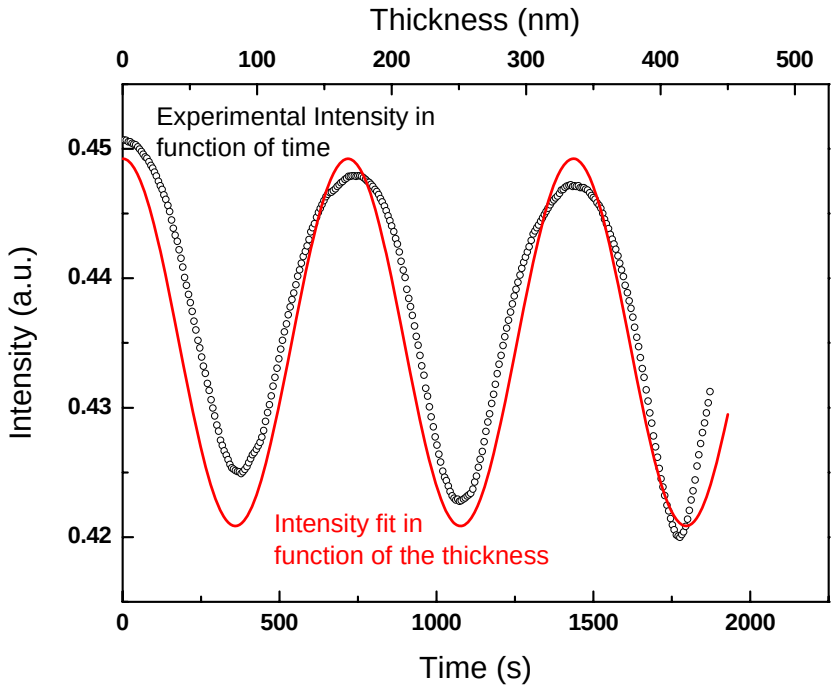

Graph 1 Intensity fit and recorded signal of the reflectometry system.

The validation of this in situ characterization tool of the growth rate is presented in the paragraph 3.3.4.

3.2.5. External beam illumination of the substrate

The possibility to add on the HV-CVD system an external energy beam for local structuring has influenced all the design of the machine. In particular, the gas distribution system, called effusing source, composed of rings is designed to minimize the distance substrate-chamber. The reactor has an opening at the bottom of the chamber with a special flange to connect a window or an electron source.

The first energy source selected is a 248 nm wavelength excimer laser (Lambda Physik LPX) with maximum impulsion energy of 300 mJ and a maximum repetition rate of 400 Hz. A quartz window, transparent to UV (see specification in appendix 9.2), is connected to the reactor and an optical setup composed of different mirrors and lenses allows to illuminate perpendicularly the substrate, see Figure 14.

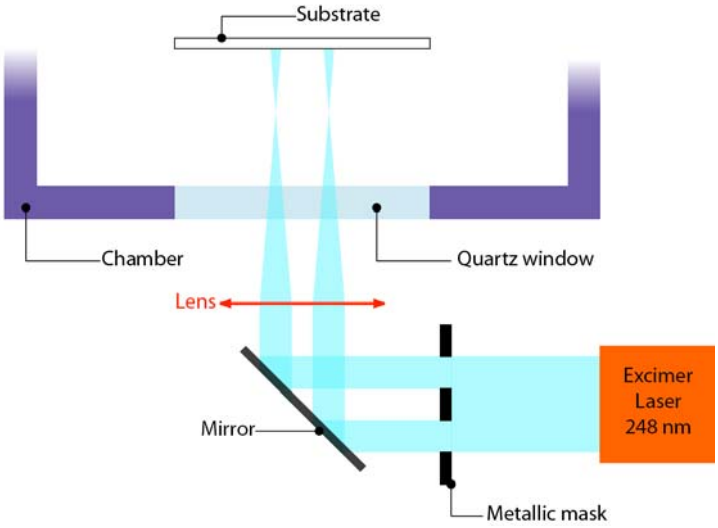

Figure 14 Schematic representation of the optical setup for laser induced HV-CVD.

Different areas of the substrate can be irradiated with the laser light thanks to two mobile mirrors. A projection mask system is installed in order to deposit local structures on the substrate; the performance of this laser induced HV-CVD setup is presented in the paragraph 3.3.5.

An electron beam can also be directly connected to the deposition machine. An electron gun, EGG-3H from Kimball Physics, can be installed instead of the quartz window and emits with energies of 100 eV to 10 keV and beam currents from 0.2 mA to 10 mA.

The results of beam assisted HV-CVD are presented in Chapter 6.

3.3. Simulations, performances and limitations

3.3.1. Heating system

The substrate temperature is an important variable in deposition process, having profound effects on the structure, composition of the films and the growth rate. Heat transfer and temperature measurement are complex, especially in vacuum where thermal coupling is poor. Indeed heat transfer under vacuum can occur only by radiation and conduction. But good heat conduction provided by the solid phase can only take place where there is atomic contact to transfer the heat by phonon vibrations and by electrons, in the case of metals [2].

Unfortunately, most surfaces are not atomically flat; intimate atomic contact occurs only at a few points with a total surface which is almost negligible on the whole substrate, as illustrated on Figure 15. So heat transfer under vacuum between two surfaces is dominated by radiation.

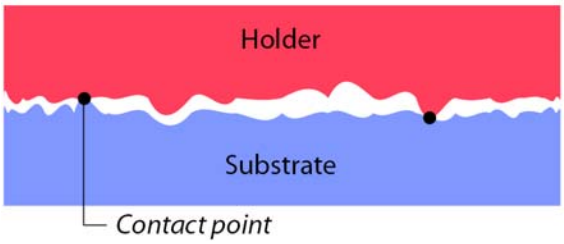

Figure 15 Microscopic schematic view between substrate and holder.

The maximum amount of radiation flow which can be emitted by a surface is given by the Stefan-Boltzmann blackbody radiation law: $\Phi_b = \tilde{n}^2 \sigma T^4$, where $\tilde{n}$ is the index of the medium over the surface, T the temperature of the surface and σ Stefan-Boltzmann constant. Real surfaces emit only a fraction ε_λ of that amount, where ε_λ is the emissivity and is a function of the radiation wavelength λ and also absorb only a fraction α_λ of the incident radiation. In the following, to solve the heat transfer problems of the heating system, the gray body assumption is made. Indeed, ε_λ and α_λ are considered constant (independent of λ) and equal: $\varepsilon_\lambda = \alpha_\lambda = \varepsilon$. As we know from the Wien's displacement law, this hypothesis is not completely true but helps to calculate a good estimation of the delta temperature between holder and substrate.

As detailed in the appendix 9.3, we can calculate theoretically the temperature of a substrate heated only by radiation in an enclosure [90]. The substrate temperature T_3 is given by:

$$T_3 = \left[\left(T_2^4 - T_1^4\right) \frac{\frac{1}{\varepsilon_1} + \frac{1}{\varepsilon_{31}} - 1}{\frac{1}{\varepsilon_1} + \frac{1}{\varepsilon_2} + \frac{1-\varepsilon_{31}}{\varepsilon_{31}} + \frac{1-\varepsilon_{32}}{\varepsilon_{32}}} + T_1^4 \right]^{1/4}$$

Where T_1 is the heater temperature, T_2 is the chamber temperature and ε_1, ε_2, ε_{31}, ε_{32} are respectively the emissivity of the heater, the chamber, the backside of the substrate and the front side of the substrate. The heater, substrate and chamber wall are considered as parallel semi-infinite layers.

From this approximation, we can predict the importance of the different parameters in order to have the maximum substrate temperature. In the following results we have considered an experimentally measured chamber temperature of 50 °C during operation and an estimated emissivity of the stainless steel chamber of 0.55.

It is clear that increasing the heater temperature is the best way, due to the power four, to increase the substrate temperature but we are limited, for technical reasons, to 1100 °C for the heater temperature. As presented below, we observe that increasing the emissivity of the heater and/or the backside of the substrate leads to a higher temperature of the substrate, as well as decreasing the front side emissivity of the substrate. In Graph 2, the temperature ratio represents the ratio between substrate temperature and heater temperature.

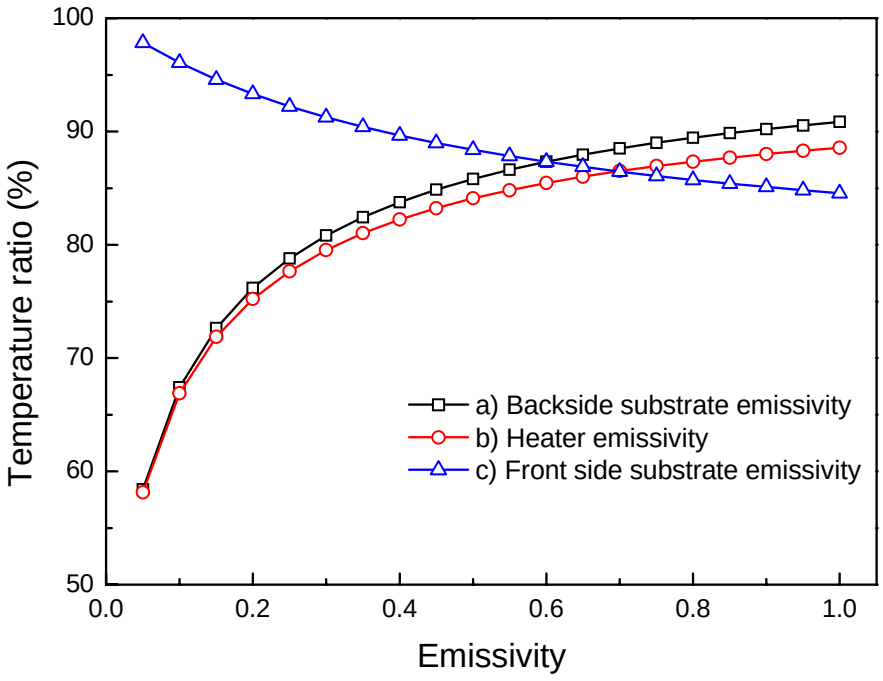

Graph 2 Simulation of emissivity influence on substrate temperature
Heater temperature = 500 °C, Chamber temperature = 50 °C, Chamber emissivity = 0.5
a) Heater emissivity = 0.8 and front side substrate emissivity = 0.6 b) Backside and front side substrate emissivity = 0.6 c) Heater emissivity = 0.8 and backside substrate emissivity = 0.6.

Decreasing the front side emissivity of the substrate is inconceivable because the properties of this surface is primordial for the thin films growth and after the beginning of the CVD process the emissivity is strongly influenced by the deposited film. In brief, higher is the emissivity of the heater and the back of the substrate higher is the substrate temperature.

We tried different heating block with different emissivity (see appendix 9.4) and different substrate as well; the results of the heat transfer between heater and substrate, and the comparison with the empirical model are now discussed.

Working with silicon wafer involves that the emissivity of the substrate back side is already ε_{Si}=0.6. As illustrated on Graph 3, increasing the emissivity of the back of the

silicon substrate has not a really important impact on the substrate temperature. On the other hand the heater block emissivity can be improved in a larger manner. Indeed polished molybdenum has an emissivity of ε_{Mo}=0.13 thus a high emissive coating on the heater can help to reach significantly higher substrate temperature.

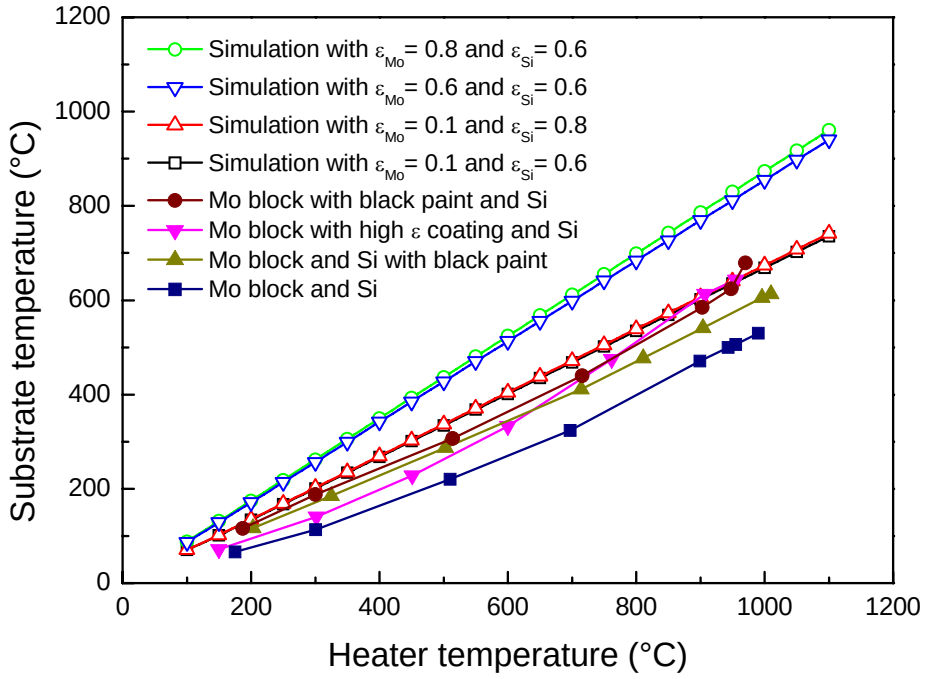

Graph 3 Substrate temperature versus heater temperature.
Open symbols represent simulations (empirical model) for different emissivity, plain symbols are measured values for different heating block and substrate.

The Graph 3 shows that the empirical model, without any considerations about geometry and conduction losses in the holder, does not represent the reality; indeed the simulation overestimates the substrate temperature. That is the reason why we developed a more sophisticated numerical model and simulations based on finite elements in Comsol multiphysics software. The geometry of all the pieces and the losses are included. Two and three dimensional models are proposed.

First the two dimensional model includes the geometry of: the chamber, the effusing source, the heating block, the horse shoe holder, the silicon wafer and the support pieces. The thermal properties of the different material are applied to the heat transfer model of Comsol and are listed in the table below. The heating block is fixed at the set temperature, the effusing source is kept at 150 °C and the other pieces are initially at room temperature.

Material	Density ρ [kg/m³]	Heat capacity C_p [J/g·K]	Thermal conductivity λ [W/m·K]	Emissivity ε
Steel AISI	7850	475	44.5	0.55
Molybdenum	10280	250.78	138	0.13
Silicon	2330	703	163	0.6
Quartz	2640	1050	9	0.3

Table 6 Material properties for heat transfer simulation.

The thermal simulation of the HV-CVD reactor is presented on Figure 16. We can observe that the heat is mainly lost by conduction in the support piece of the heating block and through the horse shoe and its support pieces. The chamber is heated by radiation. With an emissivity of 0.13 for the Molybdenum block and 0.6 for the silicon wafer we calculate a substrate surface temperature of about 60% of the block temperature.

Simulations were also done for different emissivity of the contact facet of the heating block and the back side of the wafer. The results are plotted in Graph 4 and compared with the same set of measurements as in Graph 3.

For this model, including the conduction losses and the geometry of the system, the results are in much better adequacy with the experimental data.

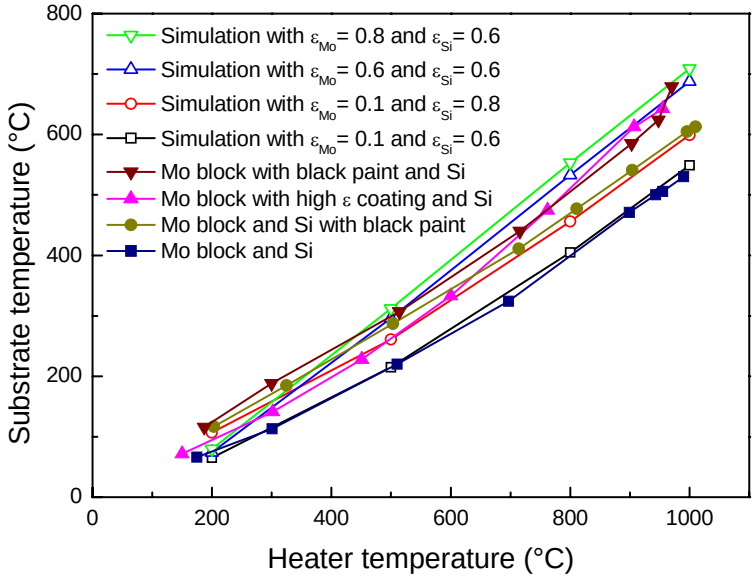

Graph 4 Substrate temperature versus heater temperature.
Open symbols represent simulations (Comsol model) for different emissivity, solid symbols are measured values for different heating block and substrate.

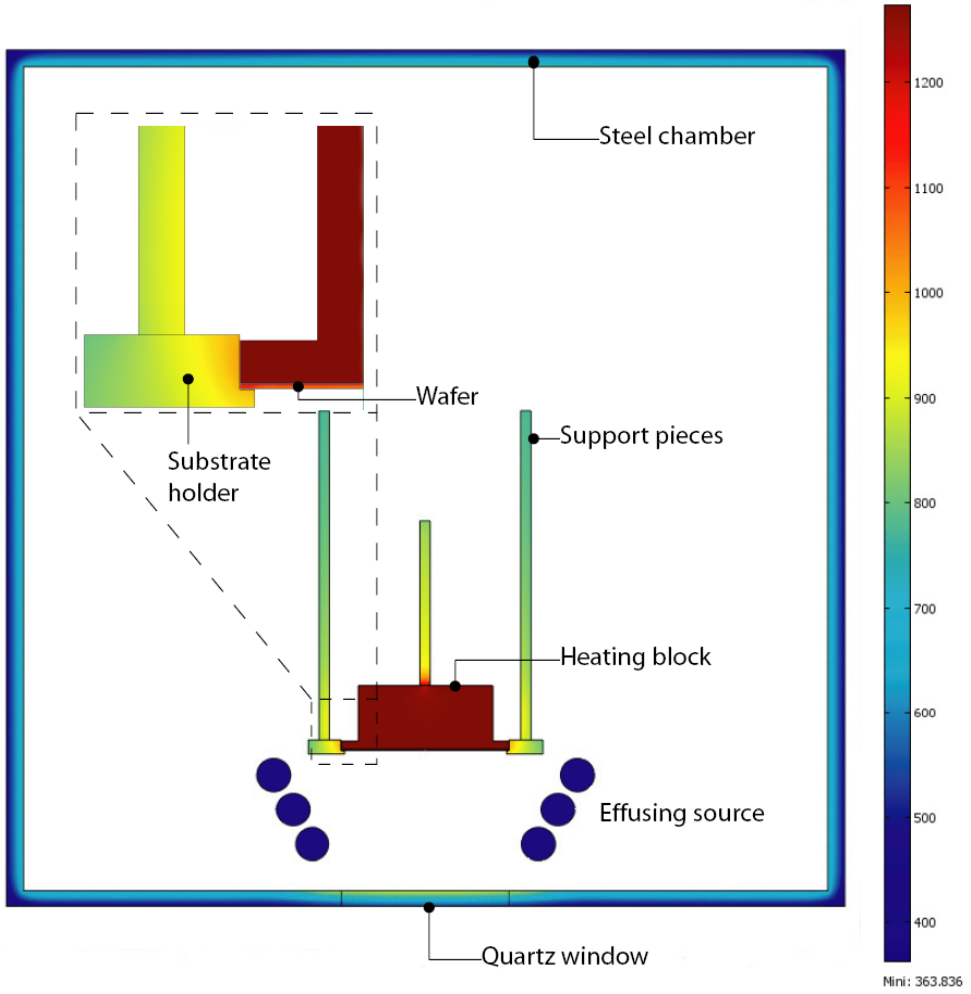

Figure 16 2D Representation of the heat transfer by radiation and conduction in the HV-CVD reactor for the heating block at 1000 °C (scale in Kelvin on the figure).

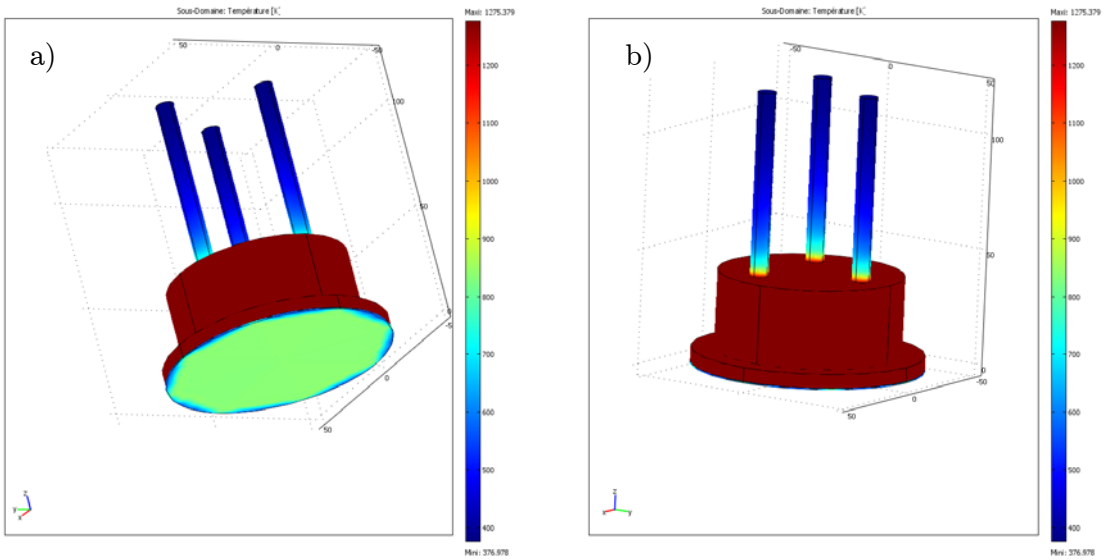

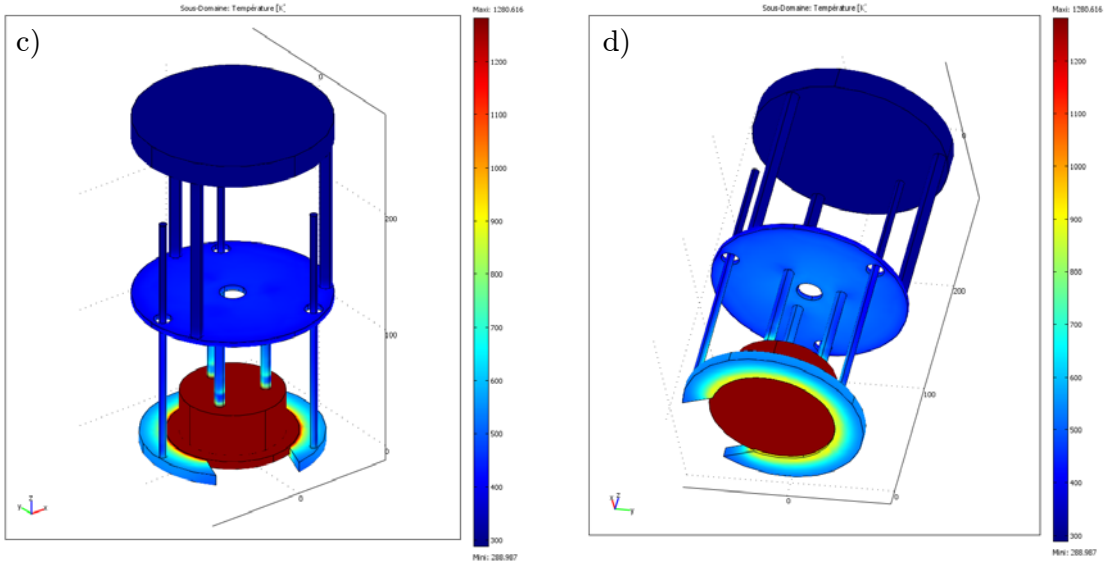

Figure 17 3D representation of the heat transfer in a) and b) the heating block at 1000 °C and silicon wafer, c) and d) all the heating system without wafer.

In conclusion, the model developed with the help of Comsol multiphysics software and considering the geometry and losses is in good adequacy with the experimental measurements. The best way to reach, in such high vacuum system, high substrate temperature is first to increase the temperature of the heating block and then have a high emissive surface of the heating block. Indeed increasing the emissivity of the back of the wafer helps but is almost negligible when the substrate has already an emissivity of 0.6 or higher.

Practically, the maximum temperature reached at the surface of silicon wafer at $5 \cdot 10^{-7}$ mbar is 700 °C for a temperature of 1100 °C of the heating block coated with a high emissive layer; thus the temperature ratio is 64%.

The limitations are understood and the temperature have been simulated with a simple model and confirmed by measurements. Furthermore, this range of temperature allows depositing good quality amorphous alumina with competitive growth rate (in the order of 50 nm/min). So in consequence, the heat transfer to the substrate will be not studied in further more detail.

Because of inevitable delta temperature always develops between the heater and the substrate whenever radiation is the main mode of heat transfer, it is best to monitor during deposition directly the substrate temperature. In that manner an evolution with time of the emissivity will be also overcome.

3.3.2. Gas transport

The precursor flow is an important parameter is CVD processes in order to obtain reproducible and reliable results. Constant flow over a certain period of time must be possible as well as regulation of the flow to study its influence. From the pressure control system installed on the reactor we can regulate the precursor pressure in the line. This pressure is directly linked to the precursor flow. So we measured the precursor weight loss in the reservoir heated at 130 °C after fifteen minutes of pumping on the precursor in standard deposition conditions at a given and regulated pressure. In that manner a certain pressure (mbar) in the line gives a certain quantity of precursor (mg/min) that has left the reservoir for the same period of time. Finally, in the approximation monolayer evaporation, we can express the precursor flow (molecules/s·cm^2) impinging on the surface substrate in function of the pressure, see Graph 5. The relation can be described, in this pressure range, by the equation: y = a + b·x, where y is the precursor flow, x the pressure, a = -3.4·10^{15} and b = 6.9·10 ^{16}. This relation will be use in this thesis as calibration for the precursor flow.

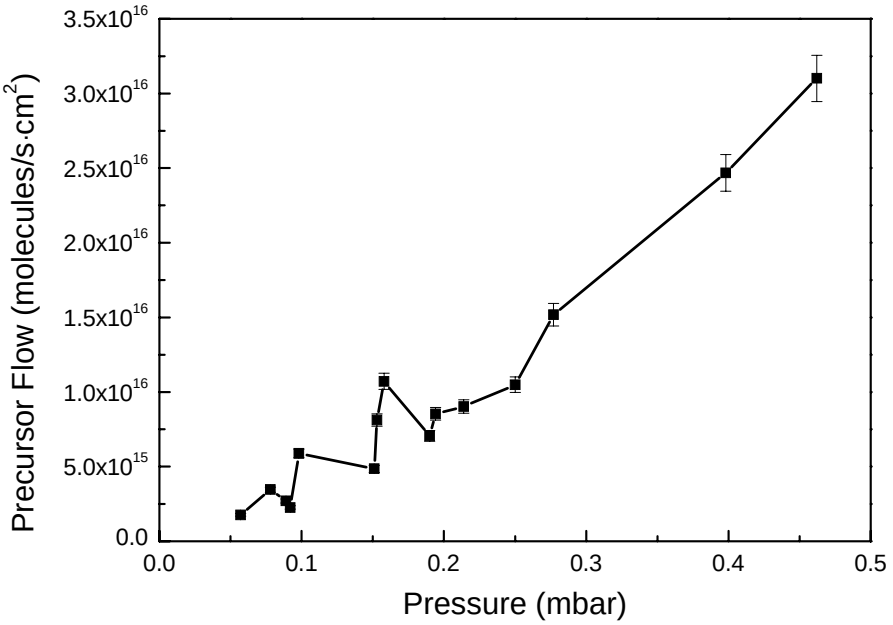

Graph 5 Relation between precursor flow and pressure.

As already mentioned, all the gas lines in which the precursor is transported must be heated slightly higher than the precursor reservoir to avoid condensation of the precursor on the walls. Nevertheless some cold spots can be present and accumulate condensed precursor. In consequence clogging (see Picture 5 and Picture 6) of the

pipes can take place and influence the transport, i.e. the precursor flow. Homogenous heating of the pipes helps to avoid clogging effect but due to the precursor sticking coefficient and residence time, precursor likes to stay on the walls.

Picture 5 Clogging in a valve.

Picture 6 Clogging in a vacuum connection.

So, the precursor flow can be controlled and measured from the pressure inside the prechamber in a reliable way. Indeed controlling the precursor flow only with the temperature of the precursor reservoir is not sufficient due to the possible variations of the precursor vapor pressure with time, see Chapter 4. Cold spots along the precursor path must be absolutely avoided.

3.3.3. Effusing source

The effusing source presented in 3.2.3 will be now discussed in more detail. This device allows depositing thin films with thickness uniformity better than 95% on four inch diameter substrates, without substrate movement. Indeed, the effusing source distributes homogenously the precursor molecules on the substrate surface and then the molecules can be decomposed during the High Vacuum Chemical Vapor Deposition (HV-CVD) process to form uniform films.

The effusing source is made of three independent rings, each of them consisting of 25 holes with a diameter of 500 μm. The combination of all the holes of one ring gives a uniform molecular distribution on the substrate. Each hole acts as a Knudsen effusor. In order to guarantee the higher uniform distribution, the geometry of the effusing source is critical. The diameter of each ring, the distance of the rings to the substrate, the diameter of the holes and the wall thickness of the orifice influence all the final distribution on the surface.

For a better understanding, we propose in a first time to focus on what is happening to a single hole and then to simulate the distribution obtained with 25 holes. Finally, the simulations will be compared with the experimental results to confirm our calculations and prove that high thickness uniformity on 4 inch substrates can be reached.

In order to consider a hole as a Knudsen effusing cell, it must fulfill some criteria and some approximations have to be discussed as well. In Knudsen theory, evaporation occurs as effusion from an isothermal enclosure with a small orifice, called a Knudsen cell. The diameter of the orifice must be about one-tenth or less of the mean free path of the gas molecules at equilibrium pressure and the wall around the orifice must be vanishingly thin so that gas molecules leaving the enclosure are not scattered or adsorbed and desorbed by the orifice wall [91]. Under these conditions, the orifice constitutes an evaporating surface with the evaporant pressure P but without the ability to reflect vapor molecules. The gas pressure inside the cell must be much higher than the pressure of the chamber, in our case high vacuum. The total number of molecules effusing from the Knudsen cell into the vacuum per unit time called total effusion rate is given by: $Q \equiv 8.33 \cdot 10^{22} \frac{P \cdot S}{\sqrt{M \cdot T}} \left[\frac{molecules}{s} \right]$, where S is the orifice area, T is the temperature and M is the molecular weight of the evaporating species [91]. As we are in high vacuum, the pressure chamber where the evaporation takes place is approximated to zero.

Consider the geometry of Figure 18, where material is being evaporated from a disc source (hole) of diameter r centered at point A onto a flat substrate situated at perpendicular distance r_0 away.

First, we want to determine the evaporant flux J_1 at radius r_0 from the source and at some angle θ from the vertical (point C) compared to flux J_0 at the vertical (point B). The projected area of the hole from point C changes from a circle (point B) to an ellipse according to the angle θ; so we can express $J_1 = J_0 \cos(\theta)$ (1), this is known as cosine flux distribution

.

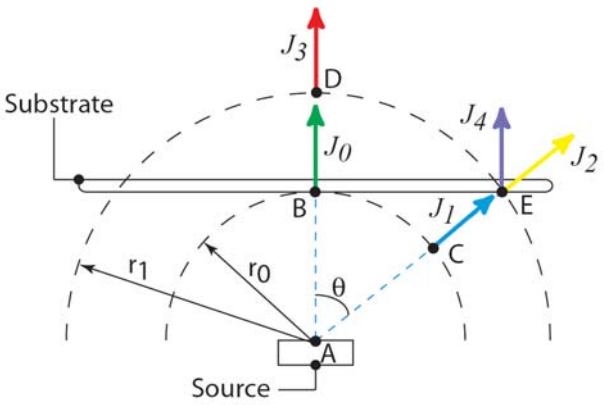

Figure 18 Schematic representation of the cosine distribution from a disc source in direction to a flat substrate.

By integrating J_1 over the hemisphere of evaporation and by mass conservation this integral must be equal to the total evaporation rate Q, thus we have [2]:

$$Q = \int_0^{\pi} J_0 \cos\theta \cdot 2\pi r_0 \sin\theta \cdot r_0 d\theta = \pi r_0^2 J_0 \qquad \text{or} \qquad J_0 = \frac{Q}{\pi r_0^2}$$

From the cosine distribution, we can now determine the flux on the flat substrate at the point E. In this case the flux is attenuated because the point E is at radius r_1 rather than at r_0. From the equation above, we have $J_0 = \frac{Q}{\pi r_0^2}$ and $J_3 = \frac{Q}{\pi r_1^2}$ then from the trigonometric relation $r_1 = r_0/\cos(\theta)$, we can replace J_3 and r_0 in the following proportional relation $\frac{J_3}{J_0} = \frac{J_2}{J_1}$ to obtain $J_2 = J_1 \cos^2(\theta)$

But the flux J_4 that determines the deposition rate is the flux perpendicular to the substrate at point E. So the flux is reduced from J_2 by another $\cos(\theta)$ factor as shown in Figure 18. Expressing J_2 in function of J_0 we finally have $J_4 = J_0 \cos^4(\theta)$.

In that configuration, we notice that from the $\cos^4(\theta)$ factor, there is always a trade-off between non-uniformity at short distances and evaporant waste at large distances. That is the reason why we propose a refined geometry of the effusing source with tilted angles in order to improve the uniformity at short distance, indeed we need to keep the distance substrate-effusing source as short as possible for the laser illumination setup. Moreover with this configuration the flux is more oriented in direction of the substrate and avoids wasting precursor.

Practically the holes of our effusing source are tilted by an angle of 78°, 57° and 35° for the upper ring, middle ring and lower ring respectively, as described in Figure 19.

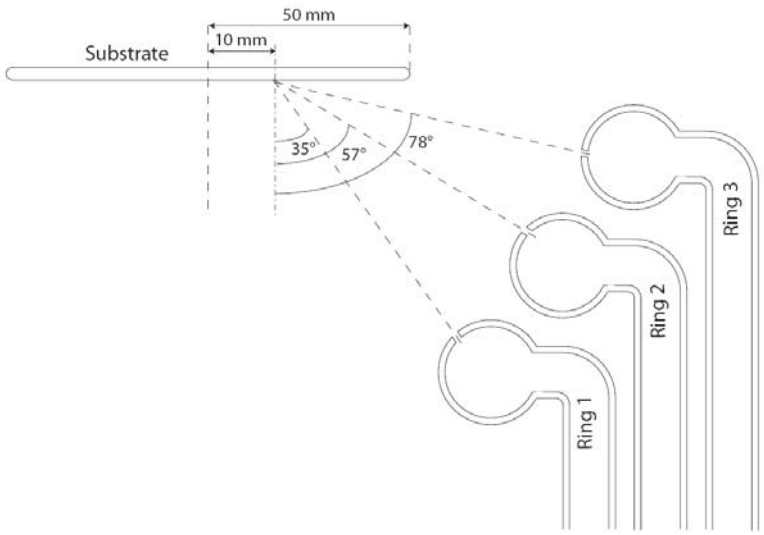

Figure 19 Schematic view of the effusing source composed of three rings with holes tilted under 78°, 57° and 35° angle.

Consequently, the final flux on the substrate must be corrected by a cos(φ) factor, where φ can be 78°, 57° or 35° according to the ring of interest.
Thereby the final flux is: $J_S = J_0 \cos^4(\theta)\cdot\cos(\varphi)$ (J)

The principal problem with this Knudsen approach is that an ideal cell with infinitely thin wall holes yielding free molecular flow can only be realized approximately. In practice, orifices of finite thickness are used which necessitates the application of corrective terms in the effusion equation.

The effusion cells are basically a cylinder with a small circular orifice and are considered as near ideal Knudsen cell. Clausing gave a theoretical analysis of near-ideal cylindrical cells who assumes a random return of molecules to the gas reservoir from the orifice walls according to a cosine law of return [92]. Correction factor W_a called the orifice transmission factor should multiply the effusion equation (J) this factor has the meaning of the probability that a molecule which enters the orifice goes directly in the chamber without having been back. Clausing's factor W_a depends only on the geometry of the hole and reduces only the flux intensity without influence on the distribution. In our configuration, we have 0.5 ratio between 250 µm wall thickness and 500 µm hole diameter thus the factor is W_a = 0.6720 [91]; the W_a factors for other L_0/d_0 are listed in appendix 9.5.

For real effusion cell, the cosine law (1) is not valid exactly. According Clausing theory [92] and Dayton [93] calculations, the power of the cosine term should be adapted in function of the ratio between thickness and diameter of the effusion orifice. In Figure 20, the effusion distribution is represented for different L_0/d_0 ratios, with a purely cosine shape for an infinitesimally thin wall (L_0=0) and more focused beam for higher ratios. Nevertheless with a ratio of 0.5 the distribution is considered close enough of the cosine law and the formula (J) is directly introduced in our simulations.

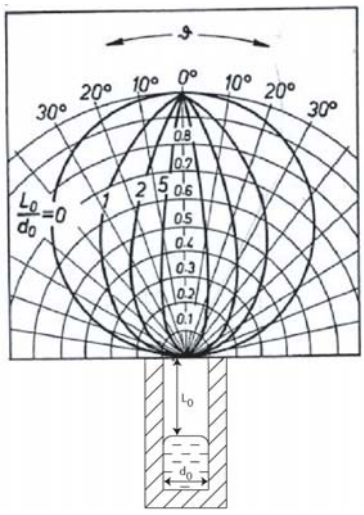

Figure 20 Different beam distributions for different L_0/d_0 ratios.

To reach high uniformity of the flux on the substrate, we need the combination of the twenty five holes of one ring. On each point of the substrate we have to consider the

contribution of each hole separated by an angle of 14.4° in the ring plan. To simulate the flux distribution on the surface of the substrate we developed with Matlab software a program (see appendix 9.6) able to calculate and to plot the flux based on the equation of the final flux J_S. For simplification and as we are interested in the uniformity we decided to set J_0 to one for the simulation.
The results of the simulation for our effusing source design are presented in Figure 21 to Figure 26. The three dimensional plot of the flux distribution intensity on a four inch substrate is represented with beside a diametric profile for the three independent rings. The thickness uniformity and the impinging rate efficiency are calculated from the equations below and can be as high as 98.2% and 23% respectively.

The homogeneity of the layer thickness can be defined by the following homogeneity coefficient: $\Gamma = \sqrt{\frac{\sum_{i,j}\left(e_{i,j} - m\right)^2}{N}}$, where $m = \sum_{i,j}\frac{e_{i,j}}{N}$ = average thickness, e point thickness and N number of measurements points.
And the precursor impinging efficiency is defined by the quantity of precursor that impinges on the substrate surface area compared to the total flow of precursor through the effusion holes.

(1) Upper ring: 181 mm diameter, tilt angle of 78°, distance to substrate 15 mm
Flux distribution uniformity: 95.3%
Impinging efficiency: 6.5%

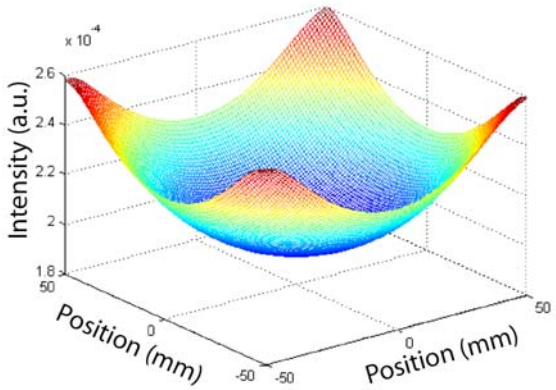

Figure 21 3D representation of the flux intensity for the upper ring.

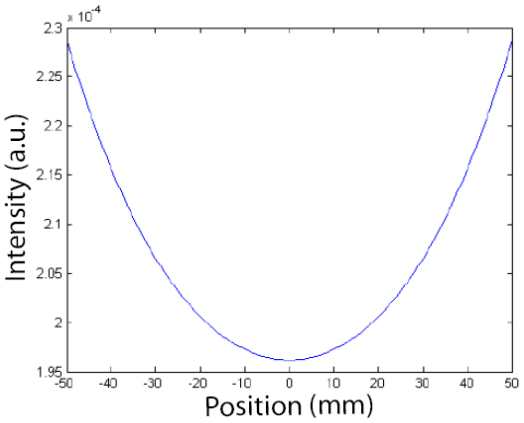

Figure 22 Diametric profile of flux intensity for the upper ring.

(2) Middle ring: 158 mm diameter, tilt angle of 57°, distance to substrate 36 mm
Flux distribution uniformity: 98.2%
Impinging efficiency: 18%

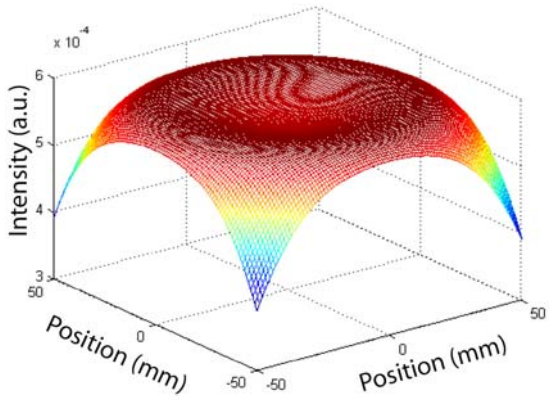

Figure 23 3D representation of the flux intensity for the middle ring.

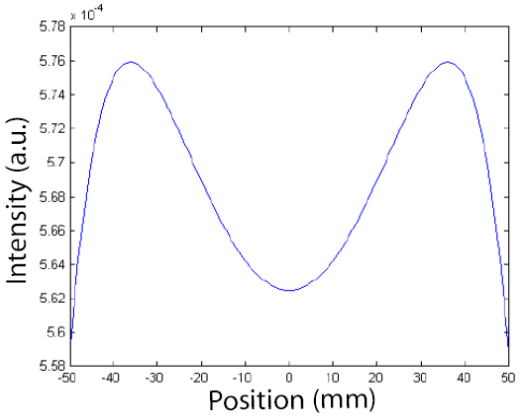

Figure 24 Diametric profile of flux intensity for the middle ring.

(3) Lower ring: 135 mm diameter, tilt angle of 35°, distance to substrate 57 mm
Flux distribution uniformity: 95.2%
Impinging efficiency: 23%

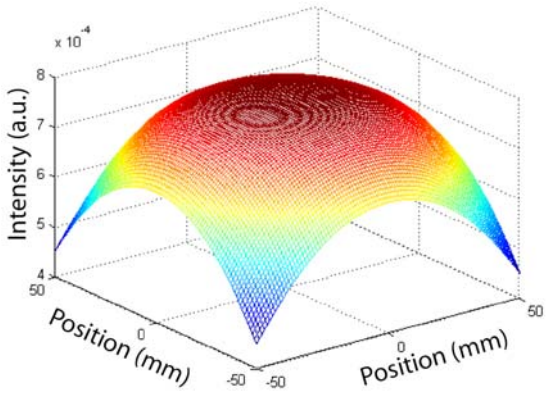

Figure 25 3D representation of the flux intensity for the lower ring.

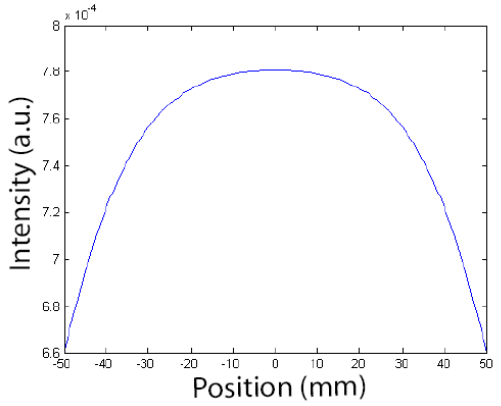

Figure 26 Diametric profile of flux intensity for the lower ring.

The thickness uniformity and the impinging rate efficiency have been simulated for different angle, see Figure 27 to Figure 32, the red lines indicate the angle chosen in our effusing source design. Having in the same time the best thickness uniformity with the maximum impinging rate efficiency is not possible, a compromise between these two values is necessary. In our case, we decided to have the uniformity better than 95% for a given geometry of the effusing source. The diameter of the rings and the distance between source and substrate are also determined by technical reasons

and by the fact that the substrate must be as close as possible to the bottom of the chamber for the external beam illumination system. In these conditions, the impinging rate efficiency is not optimized but is relatively high for this kind of deposition system; and allows saving some precursor even so the aluminum isopropoxide mainly used as precursor during this work is considered as cheap.

The flux intensity distributions for different powers of the cosine have been simulated (see appendix 9.7) but the flux equation (J) already gives distribution in good adequacy with the measured uniformity of the films, as presented below. Indeed our ratio $L_0/d_0 = 0.5$ can be approximated by a quasi-Knudsen cell.

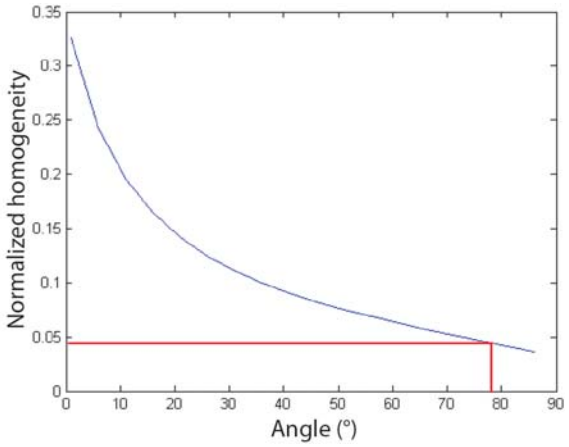

Figure 27 Homogeneity versus source angle for the upper ring.

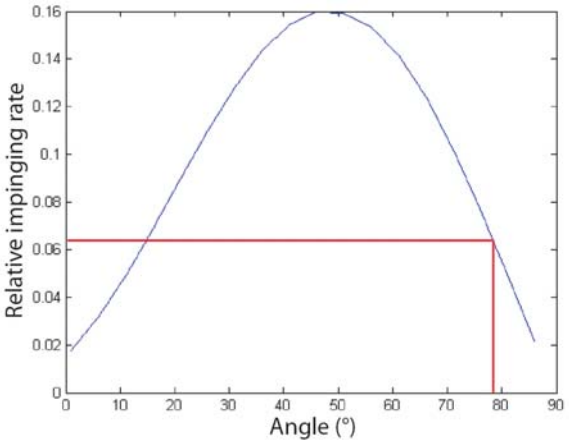

Figure 28 Impinging rate efficiency versus source angle for the upper ring.

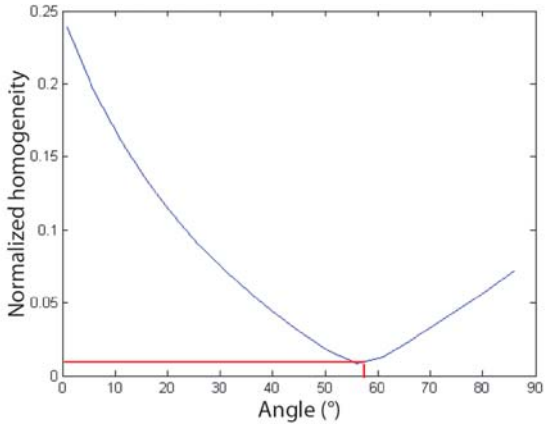

Figure 29 Homogeneity versus source angle for the middle ring.

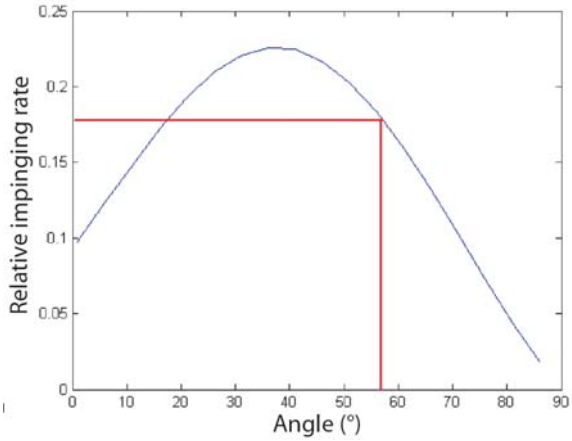

Figure 30 Impinging rate efficiency versus source angle for the middle ring.

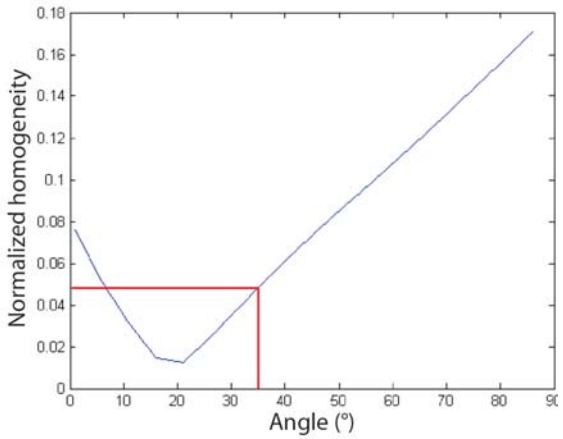

Figure 31 Homogeneity versus source angle for the lower ring.

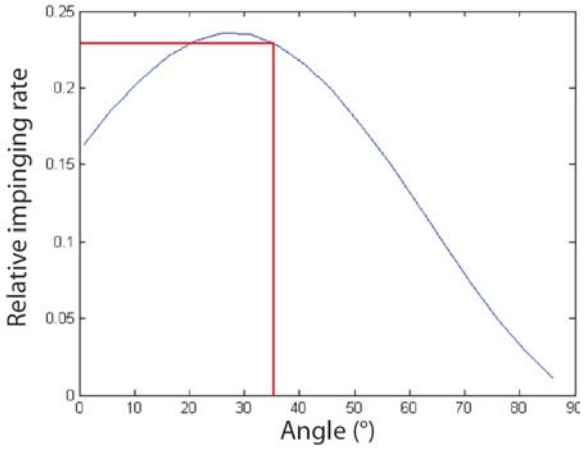

Figure 32 Impinging rate efficiency versus source angle for the lower ring.

In order to verify our simulation experimentally, we measured the thickness uniformity of different layers deposited in the mass transport limited regime. Indeed in this regime the growth rate is not influenced by temperature, thus substrate temperature variations will not affect the thickness of the layer; or in other words only differences in the number of molecules impinging on different points of the substrate can induce thickness variations between these points in a first approximation.

The thickness characterization of two different films deposited with the middle ring (higher uniformity) is presented here to illustrate the uniformity, but all the layers deposited in the mass transport limited regime present the same thickness distribution. The thickness is measured by spectral reflectometry based on the values of the refractive index n and the extinction coefficient k which have been measured by spectral ellipsometry. The thickness is measured at fifty single different places on 4 inch substrate and is interpolated in between with the help of the linear interpolation function in Matlab; the values are presented in the Figure 33 and Figure 34. The deposition conditions are: 1) chamber pressure during deposition of $8.7 \cdot 10^{-7}$ mbar, substrate temperature of 436 ºC, deposition time of 20 min and a precursor flux of $1.2 \cdot 10^{16}$ molecules/cm^2·s and 2) chamber pressure during deposition of $1.88 \cdot 10^{-6}$ mbar, substrate temperature of 407 ºC, deposition time of 20 min and a precursor flux of $1.6 \cdot 10^{16}$ molecules/cm^2·s.

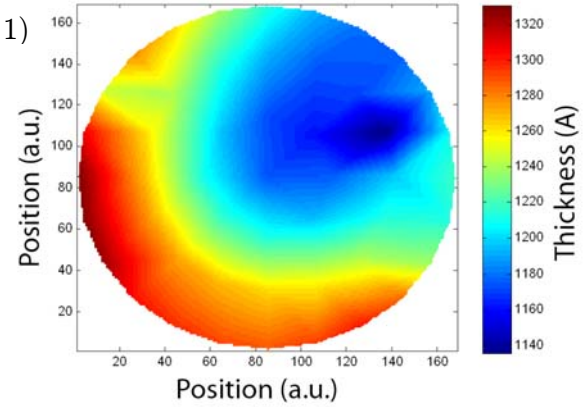

Figure 33 Thickness distribution of alumina thin film deposited with the middle ring at 436 °C and a precursor flux of $1.2 \cdot 10^{16}$ molecules/cm^2·s.

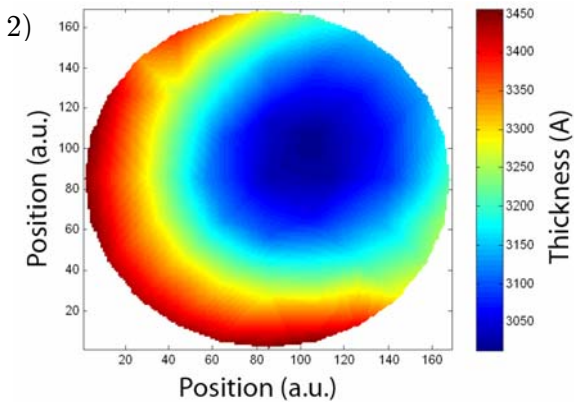

Figure 34 Thickness distribution of alumina thin film deposited with the middle ring at 407 °C and a precursor flux of $1.6 \cdot 10^{16}$ molecules/cm^2·s.

The measured thickness uniformities are 1) 95.2 % and 2) 93.8%. These experimental uniformity values are slightly lower than the theoretical values for the middle ring (98.2%). The measurement error for these uniformities is approximately 4%. Provided that, we are in good adequacy with the distribution simulation and the high uniformity obtained is clearly sufficient for future applications.

We observe that the thickness distribution of the films is not perfectly symmetric, indeed it is little bit shifted out of the center. This can be explained by a misalignment between the center of the substrate and the center of the effusing source due to too large tolerances of the substrate holder positioning. However the shape of the distribution corresponds to the simulation as show in Graph 6 by comparing (after normalization and re-centering of the experimental values) the simulated profile distribution in red and the measured points in black.

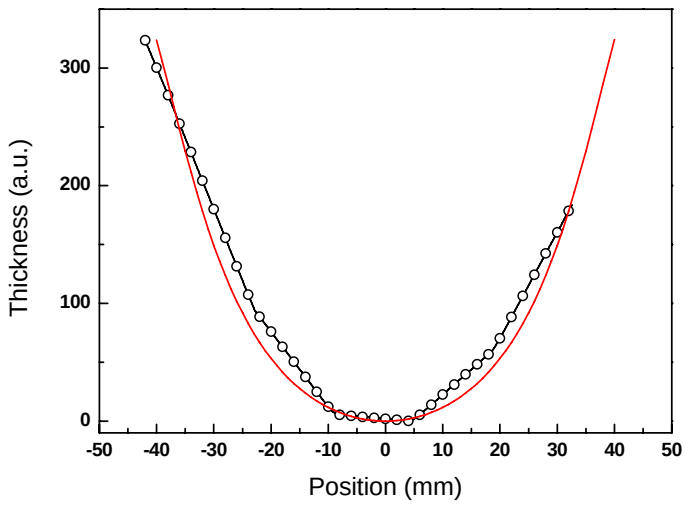

Graph 6 Comparison of the thickness profile for a simulated precursor flux distribution (red) and the real thickness measured after deposition (black).

By setting the effusing source at too low temperature and exposing it at air accidently the precursor condensed near the holes and decomposed by reaction with water present in the atmosphere inducing clogging of the holes. This alumina deposit in the orifices changed the L_0/d_0 ratio and, as developed above, focused the molecular beam. The effusing flux followed a cosine law with a higher power as represented in Figure 35.

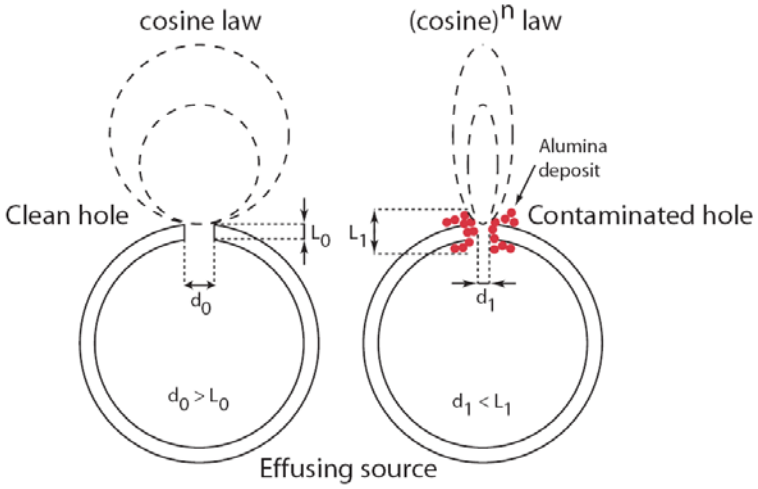

Figure 35 Flux effusion for different L/d ratios induced by clogging effect.

The deposits done with this hole shape demonstrate clearly the focusing of the molecular beam as illustrated on Figure 36 and Figure 37, where non uniform deposits show the presence of thicker areas on the substrate. Indeed, we recognize on the wafer surface the effect of the twenty five holes. By focusing the molecular beam we changed the flux distribution and more precursors hit the substrate at a given area inducing thicker deposits. The example below where deposited at 480 °C and 350 °C respectively. Again that illustrates perfectly the importance of the precursor flux in the mass transport limited regime.

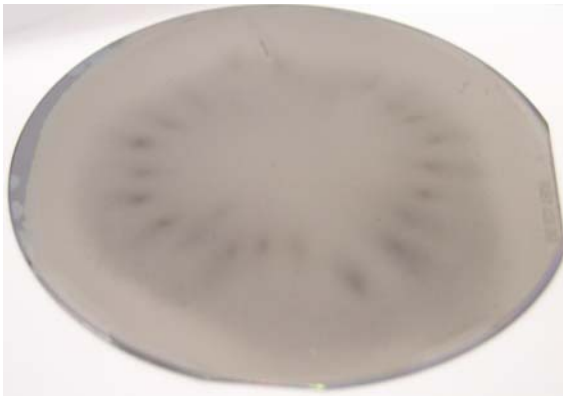

Figure 36 Non uniform Alumina deposit at 480 °C, influence of focalized molecular beam is observed.

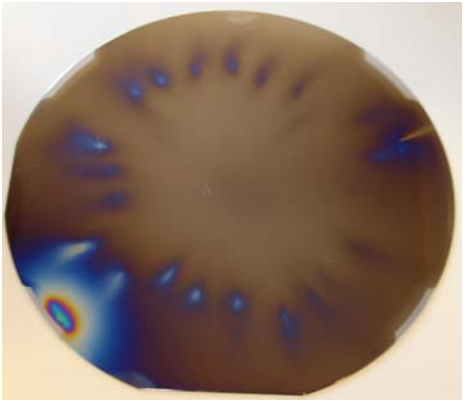

Figure 37 Non uniform Alumina deposit at 350°C, influence of focalized molecular beam is observed.

A second effect observed during the deposition tests with the upper ring is the shading effect of the substrate holder, see Figure 39. The angle of effusion for the upper ring is 78° and can be already considered as grazing angle. The substrate holder masks a part of the substrate from the precursor beam; basically the holder (see Figure 39) blocks some precursor molecules. In brief the part near the holder receives fewer precursor molecules and in consequence the deposit is thinner as proven in Figure 38; we can clearly observe the shade of the holder on the deposit. The deposit in the shadow is 70 nm thinner than in the center and was induced by the decomposition of the molecules coming from the opposite side of the effusing source. This confirms that we have molecular beam coming out from the holes and each hole contributes to the precursor distribution on the substrate surface.

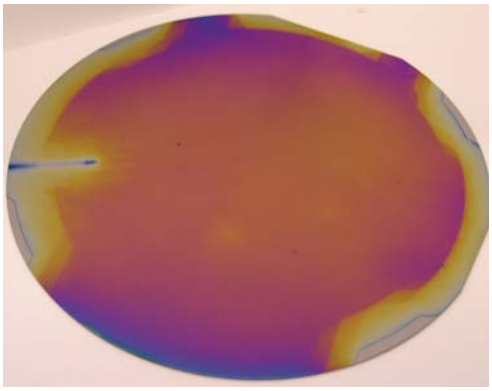

Figure 38 Alumina thin films deposited with the upper ring in the mass transport limited regime at 450 °C where the holder induced a shading effect.

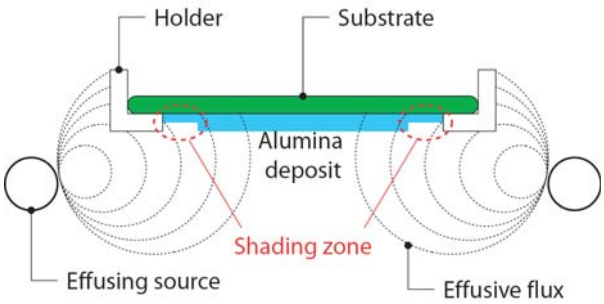

Figure 39 Sketch of the shading effect induced by the holder and the upper ring of the effusing source.

In conclusion, the original design of the effusing source gives high uniform precursor distribution on the substrate surface, as illustrated by the measurements of high uniform thickness of the alumina films with the different rings of the effusing source. Moreover, the distribution simulations are in good adequacy with the measurements and prove that Knudsen effusion take place at the exit of the holes. So, different and new effusing source designs could be imagined and simulated to induce for instance thickness gradient or composition gradient when two or three precursors are used in the same time.

3.3.4. In situ reflectometry

In order to calibrate and prove the reliability of the in situ thickness measurement setup, we deposited alumina thin films under HV-CVD conditions and the reflectometry signal was measured in function of time. The thickness was then calculated from the period of the signal and compared with SEM pictures of a side view of the deposit.

The alumina thin films were deposited from the decomposition of aluminum isopropoxide on silicon substrate heated at 428 °C ± 5 °C for 50 min ± 0.5 min (1%) with a chamber pressure of $4.2 \cdot 10^{-6}$ mbar. The in situ reflectometry signal recorded during the deposition is plotted on Graph 7; the average period is 153 s ± 4 s (2.6%). The thickness e can be calculated now from the equation presented in the section 3.2.4 with 1.4 as refractive index of amorphous alumina (see 5.1.5): e = 3673 nm ± 132 nm (3.6%). On the other hand, we have measured the thickness of the deposit from the side view of SEM Picture 7 of the same deposit; the thickness e' = 3820 nm ± 75 nm, this is the average of 10 measurements at different places with the corresponding statistical error. The two thickness values are in very good adequacy and prove that the in situ system is reliable.

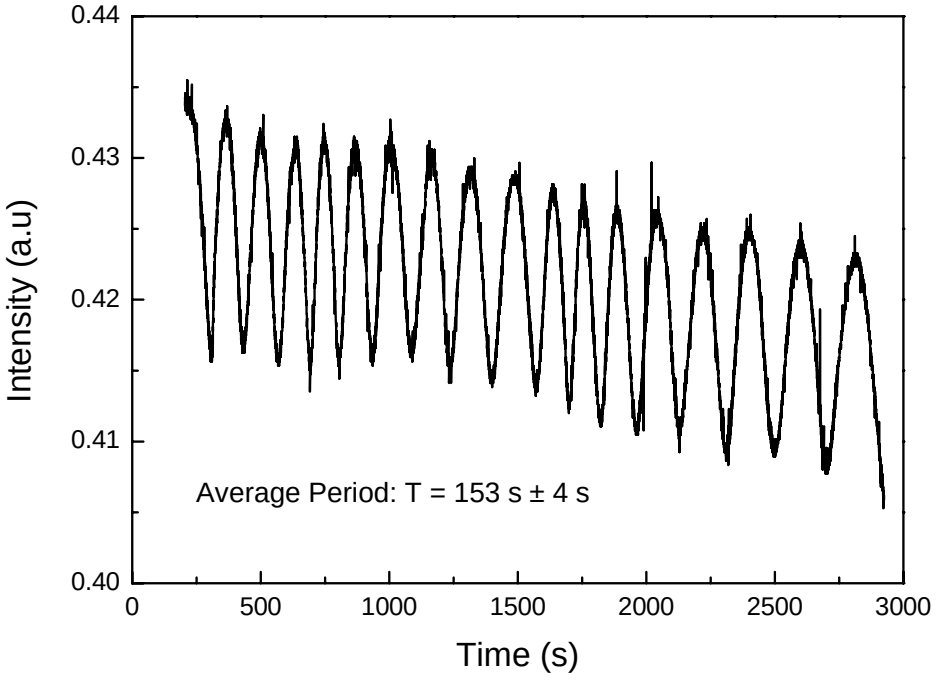

Graph 7 In situ reflectometry signal recorded during alumina growth.

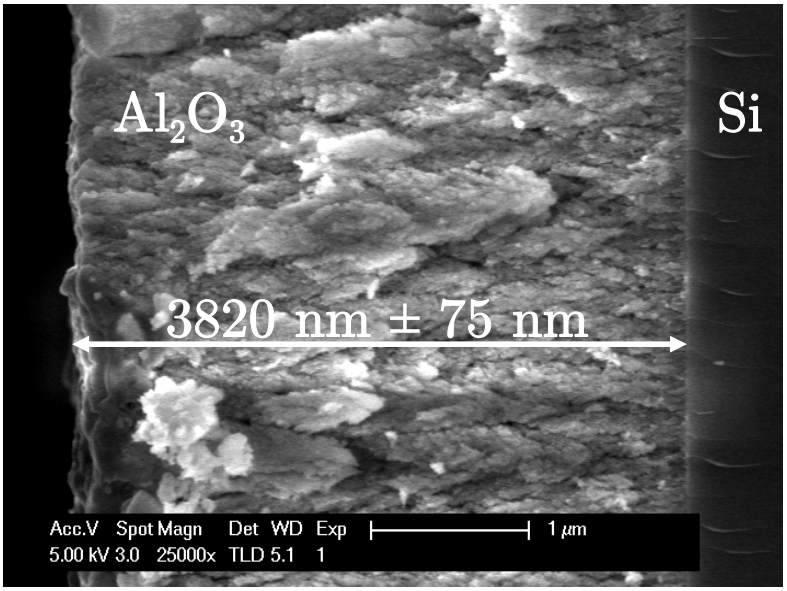

Picture 7 Side view of alumina deposit.

However, the calculated thickness from the reflectometry signal depends of the refractive index and a constant refractive index in the film is assumed; a variation of 0.1 in the refractive index induces about 6% variation on the thickness. So the precision of the thickness measured by in situ reflectometry could be about 10% in the worst case.

But the reflectometry system allows to control the thin film thickness or to follow variations of growth rate during the deposition. For instance, in Graph 8, we can observe that before the opening of the precursor reservoir no deposition takes place; this corresponds to a constant reflectometry signal, in the limit of the noise induced by the radiation of the heater. Then the deposition starts immediately when the precursor molecules reach the substrate surface and according to the temperature the period of the signal changes: in this case 350 °C ⇒ 684 s and 400 °C ⇒ 508 s, all the details about this period variation are explained in 5.1.2.

In Graph 9, the film thicknesses obtained from the in situ reflectometry signals are compared to the thicknesses of the layers measured ex situ. The good adequacy between the measurements proves that the in situ reflectometry signal is reliable for the thickness and allows having a better control of the films during deposition.

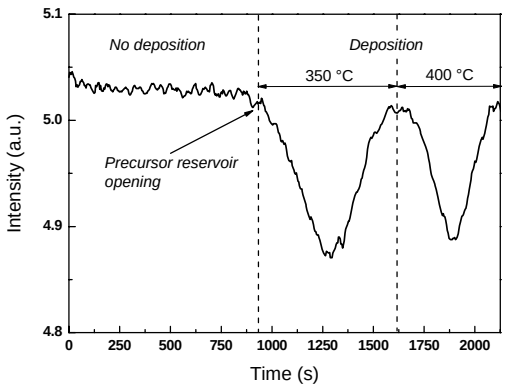

Graph 8 In situ reflectometry signal during the growth of alumina.

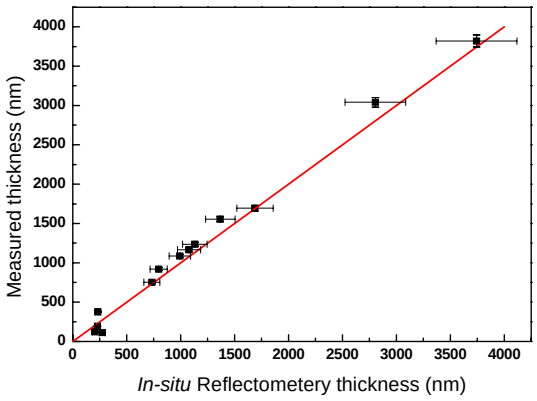

Graph 9 In situ reflectometry film thickness versus ex situ measured thickness.

Nevertheless, in order to control precisely the thickness of a film, the operator must be aware that the film keeps growing for about three minutes after closing the precursor reservoir due to the remaining precursor in the pre-chamber and connecting pipes. Adding a shutter would avoid this effect.

3.3.5. Optical mask projection system

The optical system for mask imaging installed on the machine is very simple. Different mask shapes are available and allow to illuminate the substrate with laser light under different patterns. The Figure 40 represents schematically the optical design of the projection system.

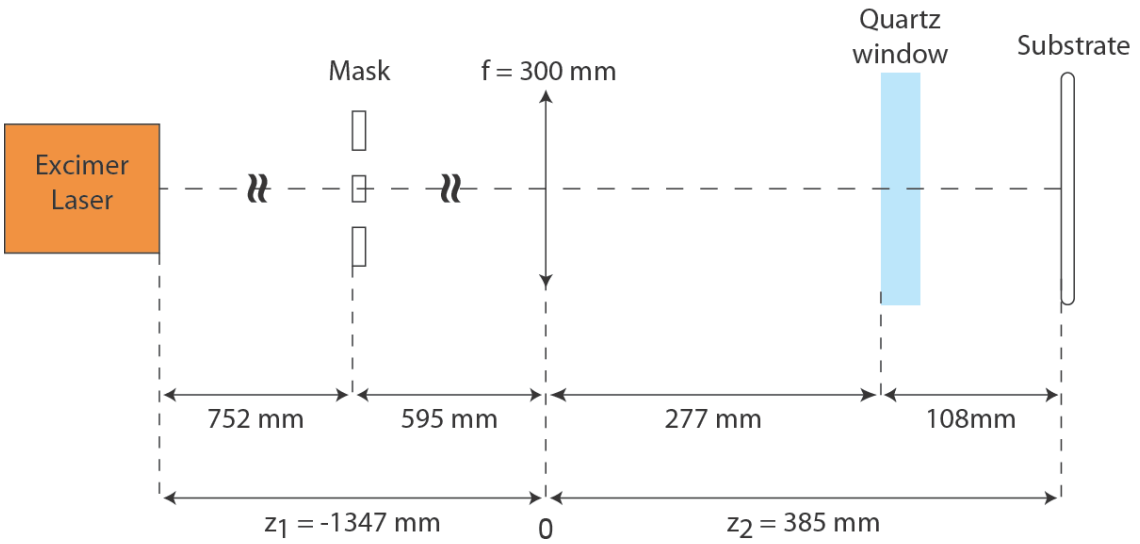

Figure 40 Sketch of the optical path of the optical mask projection system.

Each point of the mask (object) is imaging onto a corresponding point (image) with the magnification factor M and following the imaging equation:

$$\frac{1}{z_1} + \frac{1}{z_2} = \frac{1}{f}$$

$$M = -\frac{z_2}{z_1}$$

In our case we have: z_1 = -1347 mm, z_2 = 385 mm, f = 300 mm thus M = 0.3.

The Picture 8 and Picture 9 prove experimentally that the image obtained on the substrate is 3.3 smaller than the mask. Indeed with a mask width of 3.00 mm ± 0.05 mm (1.7%) we deposit alumina structure of 0.822 mm ± 0.005 mm (0.61%); in consequence the experimental magnification factor is 0.27 ± 0.01 (2.31%). The difference between the theoretical magnification and the measured one, can be explained by the precision of the distance between the optical elements. And also by the fact that the shape of the alumina structure, deposited by laser, could be influenced by unexpected side effects. The alumina structure was deposited by laser induced HV-CVD with a fluence of 200 mJ/cm^2 and a repetition rate of 300 Hz for 30 min. The deposit is formed from the decomposition of ATI on Si substrate kept a room temperature and with a chamber pressure of $5 \cdot 10^{-6}$ mbar.

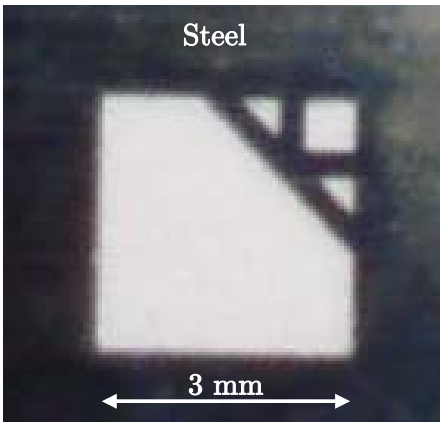

Picture 8 Metallic mask for optical projection system.

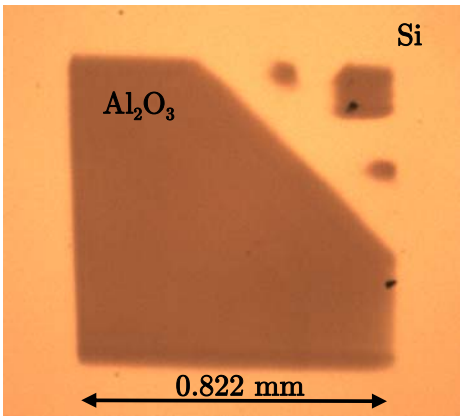

Picture 9 Laser induced HV-CVD alumina deposit.

We can observe that the deposit shape is well defined and the smallest detail is about 80 µm as confirmed on the SEM picture below. So the deposition of microstructures with this setup is demonstrated.

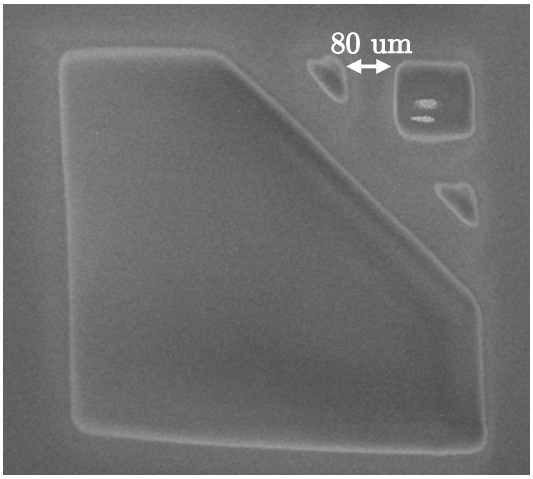

Picture 10 SEM image of alumina deposited by laser induced HV-CVD.

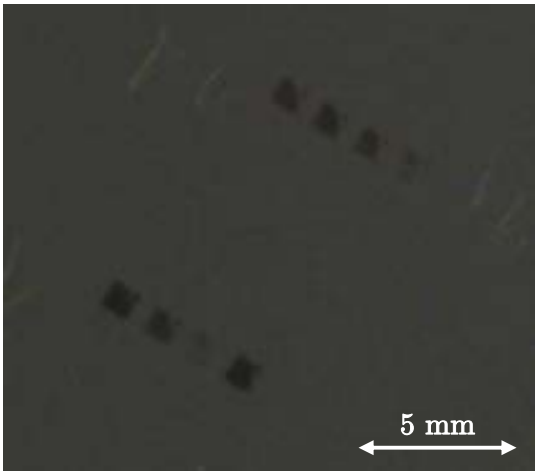

Picture 11 Array of alumina deposits.

Two mobile mirrors were installed in order to illuminate different substrate areas. An array of eight deposits can be created by moving the two mirrors between each deposit. This is illustrated on Picture 11 by eight alumina structures, deposited under different beam conditions on silicon.

The limit of resolution was not experimentally reached during this work. But a theoretical approach was done is order to evaluate the capabilities of the setup to deposit sub micrometric structures. In the following, a design for sub micrometric structures, based on Figure 41, is proposed.
The mask can be fabricated by standard technique in clean room with features of 1.5 μm dimension, so we can create a periodic structure of m = 3 μm.
Through our optical projection system we want to obtain on the substrate a sub-micrometer structure so we choose a magnificence of 5 in order to obtain 0.3 μm pattern on the substrate. This value is the critical dimension to determine the cut-off.

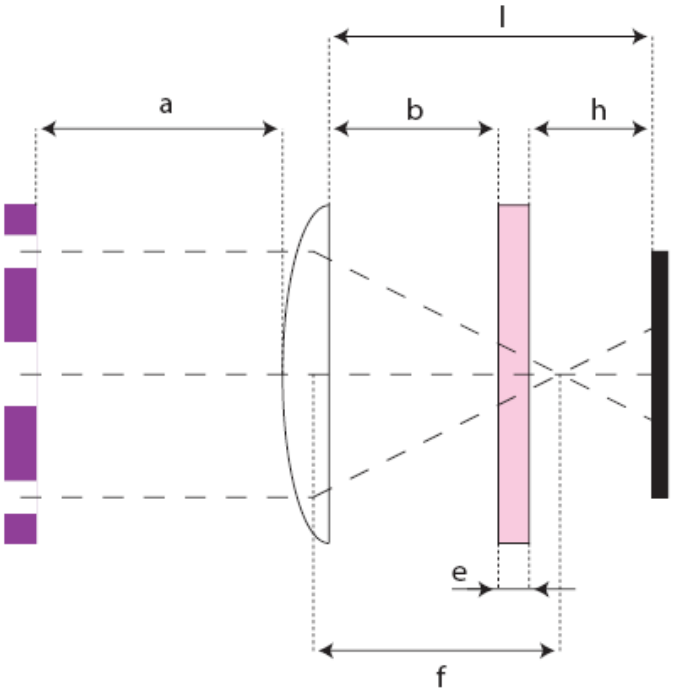

Figure 41 Optical design for sub micrometric structures deposition.

We can now calculate the numerical aperture (λ = wavelength):

$$NA = \frac{\lambda}{2m} = \frac{248nm}{6\mu m} = 4.13 \cdot 10^{-2}$$

We can determine the acceptance angle:

$$\alpha = \arcsin\frac{NA}{n} = 2.37^{\circ}$$, where n = 1 = refractive index of the air

So the distance mask to lens is (d = lens diameter):

$$a = \frac{d}{2\tan\alpha} = \frac{100\,mm}{2\tan 2.37} = 1208.64\,mm$$

The imaging equation of a lens is:

$$\frac{1}{f} = \frac{1}{a} + \frac{1}{l}$$

For a lens with the following characteristics (d = 100 mm and f = 200 mm) we can determine l = 239.66 mm.

If we consider that the thickness e of the reactor window is 3 mm we can determine the distance lens to reactor window b = 125.41 mm.

By changing the lens and modifying the geometry of the optical projection setup it should be possible to deposit sub micrometric structures.

Finally, we calibrated the average laser power P_s on the substrate, after all the elements of the optical setup, in function of the output laser power P_0. The linear

relation measured is presented on Graph 10 and allows to determine directly the fluence F on the substrate from the output laser power for a giving repetition rate f and a the area of illumination s ($P_0 \rightarrow F = P_s/f{\cdot}s$). The maximum fluence obtained with this setup at the surface of the substrate is 400 mJ/cm^2.

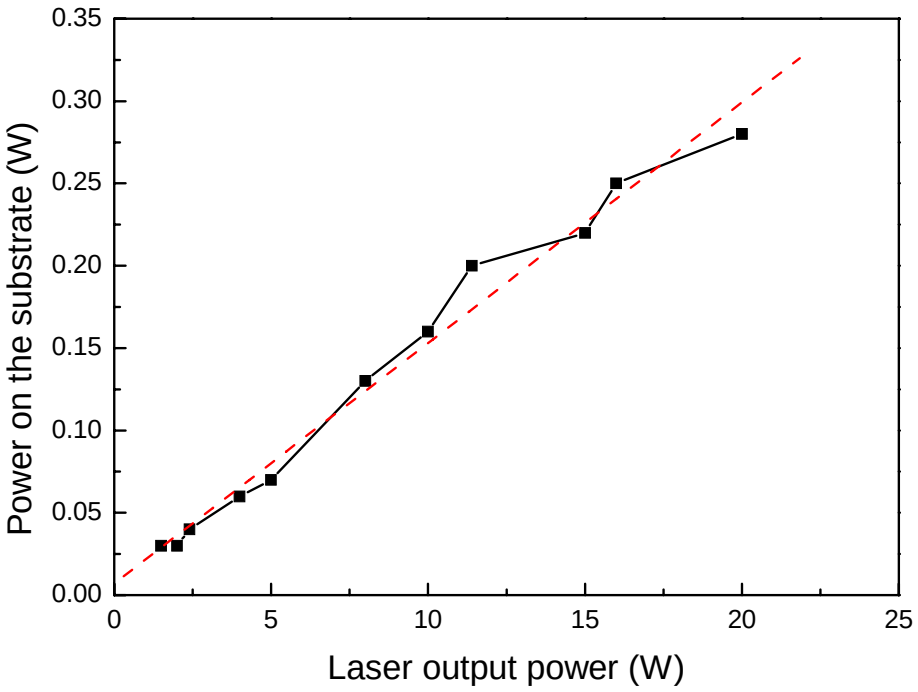

Graph 10 Power on the substrate versus laser output power.

3.3.6. Laser local heating

In CVD processes, the assistance of a laser can have two different effects: photolytic or pyrolitic. In this section we focus on the second one and propose to simulate the local increase of temperature induced by 248 nm excimer laser beam. We will study the delta temperature obtained on silicon substrate for different fluences of the laser, the role of the repetition rate and the influence of alumina growing film on the substrate.

The laser parameters are: the fluence on the substrate (maximum 400 mJ/cm^2), the repetition rate (maximum 400 Hz) and the pulse duration (25 ns), moreover we made the approximation that the laser pulse has a rectangular shape, i.e. the fluence is constant during the pulse.

To simulate the increase of temperature we use a software developed by F. Wagner and E. Halary-Wagner [94], based on the equation presented in section 1.3.6. This numerical approach includes the calculation of the incident light intensity, the calculation of the incident light profile in a film and in the substrate, the calculation of the light absorbed and finally the balance between heat generated by light absorption and heat loss by conduction. Three hypotheses are made: 1) Absorbed light is instantaneously transformed into heat, 2) Heat is lost only by conduction and 3) No phase change or non-uniformity of the material is considered.
The material properties, as for example thermal diffusivity and heat capacity, are considered constant in function of the temperature.
The material properties needed for such simulations are listed in the Table 7.

Material	Thermal diffusivity D [cm^2/s]	Heat capacity C_p [J/g·K]	Density ρ [g/cm^3]	Absorption coefficient α [1/cm]	Refractive index n
Silicon	0.85	0.71	2.32	$1.67 \cdot 10^6$ (@ 250 nm)	1.68 (@ 248 nm)
Alumina	0.12	0.9	3.99	30-70 (@ 250 nm)	1.65 (@ 250 nm)

Table 7 Thermal properties of Si and Al_2O_3 [95].

The first thing we observed is that there is no heat accumulation into the substrate that means that the heat effect necessary for the deposition can not be accumulated to reach higher temperature, thus each pulse helps independently to heat the substrate even with the highest fluence. Indeed, with the maximum repetition rate of 400 Hz, the time during two laser pulse is $2.5 \cdot 10^{-3}$ s or in other words $25 \cdot 10^5$ ns. This long time, compared to the pulse duration allows the substrate to cool down to the initial temperature, as simulated on Graph 11 for a fluence of 200 mJ/cm^2 on silicon. In these laser illumination conditions of Si, the substrate needs about $1.3 \cdot 10^{-5}$ s to decrease its surface temperature by 99% of the induced ΔT. This time is much shorter than the time between two pulses and no heat accumulation takes place. Anyway for a typical laser assisted deposition of one hour, the heat transfer from the radiation of the pre chamber heated at 150 °C is larger than the heat accumulation due to the laser irradiation.

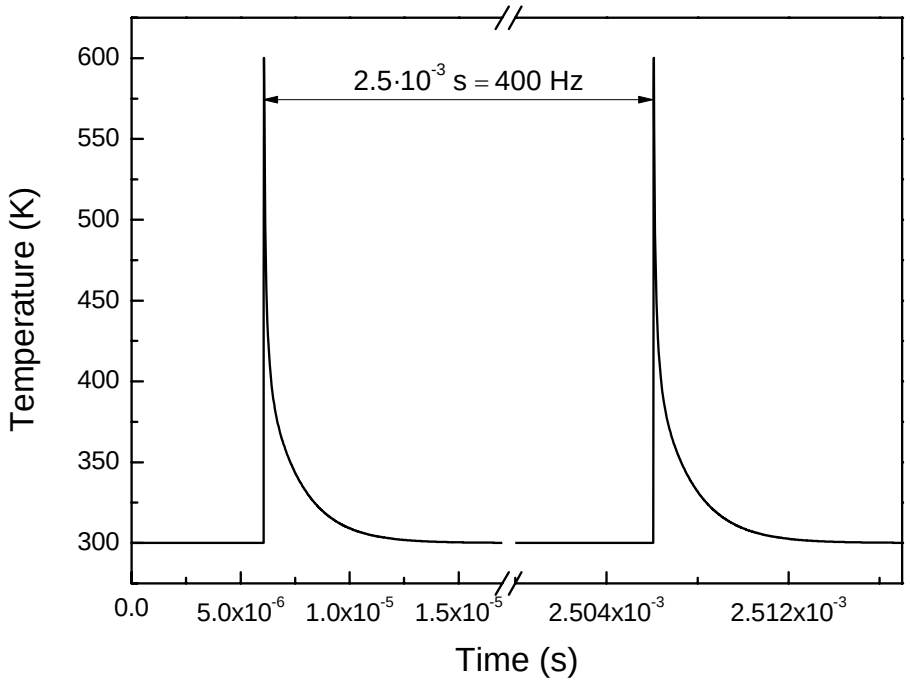

Graph 11 Temperature increase on silicon surface under irradiation of two 200 mJ/cm² laser pulses separated by 2.5 10^{-3} s (400 Hz).

From that observation, we also deduct that the substrate is illuminated for a very short period. For instance in HV-CVD conditions, one hour of laser induced deposition with a repetition rate of 400 Hz is, in fact, only 36 ms of real illumination and the thermal effect is present less than 20 s.

In Graph 12, the temporal profile of temperature on silicon substrate surface is presented for different fluences. The initial temperature of the substrate is 300 K. The dashed black line represents the theoretical shape of the 25 ns laser pulse. The other curves represent the temporal evolution of silicon surface temperature, we observe that the maximum temperature is reached at the end of the laser pulse and that the substrate cool down rapidly after the end of the illumination.

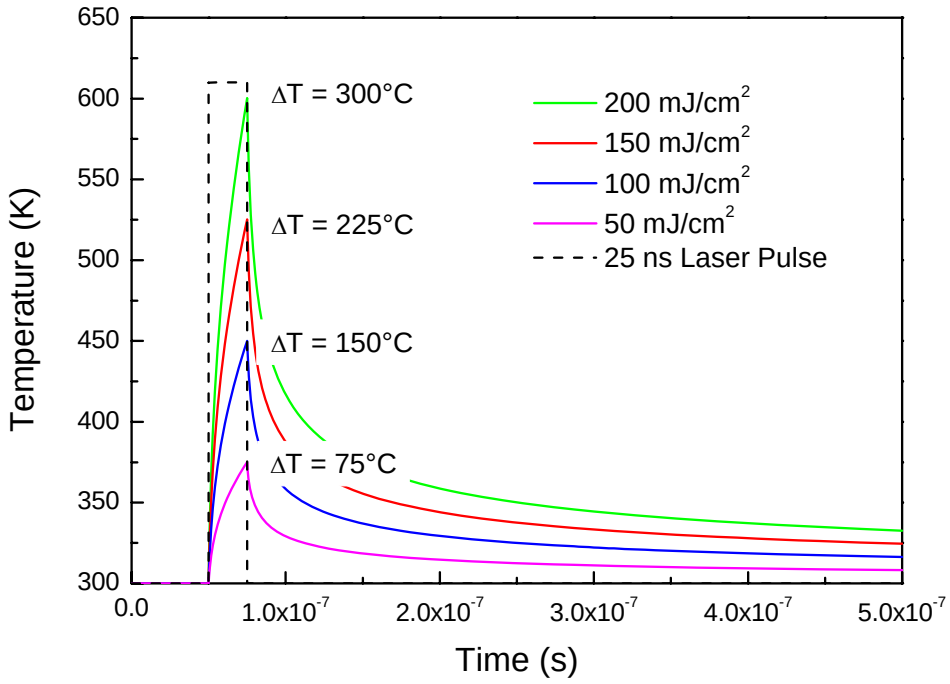

Graph 12 Temporal profile of temperature at the surface of Si for different laser irradiation.

The aim of the excimer laser irradiation is to deposit locally thin films. So the film growing under the laser beam can influence the delta temperature obtained on the substrate. Indeed at the beginning the local heating effect is on the substrate (here Si) but then the optical and thermal properties of the film material change the temperature at the surface where the deposition takes place. The temporal profile of temperature for different thickness of alumina is presented on Graph 13. We observe that for the same laser conditions (200 mJ/cm^2) the delta temperature decrease with the thickness of the deposited alumina film but the time necessary to cool down is larger. This is due to the small absorption coefficient and the small thermal diffusivity of the alumina respectively.

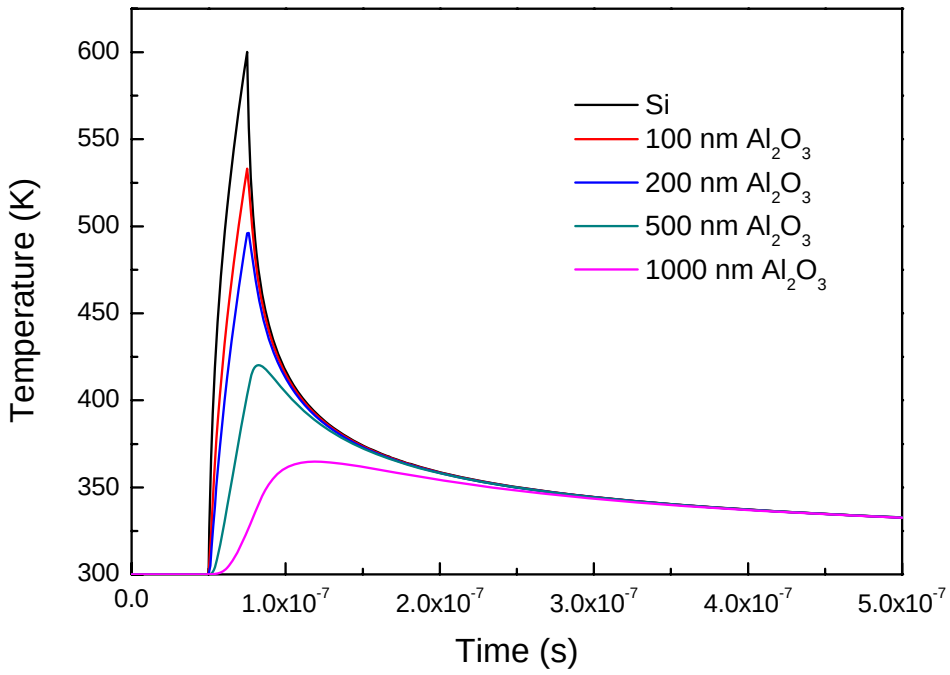

Graph 13 Temporal profile of temperature at the surface of Si and different alumina thickness for 200 mJ/cm² irradiation (25 ns pulse).

Due to the approximation of rectangular shape of the laser pulse (in reality: nearly Gaussian shape with lower maximum and larger width), the maximum temperature reached is overestimated and the time to cool down would be longer. However, the heat accumulation at the substrate surface between two laser pulses is negligible compared to the heat that the effusing source (usually at 140 °C) can transmit to the substrate by radiation.

3.4. Characterization setups

3.4.1. High resolution imaging

High resolution imaging was done with field emission Scanning Electron Microscope (SEM), FEI XL30 SFEG, available in the Interdisciplinary Centre for Electron Microscopy (CIME) at EPFL. The in-lens Secondary Electron (SE) detector can reach a maximum resolution of 2.5 nm at 1 kV and sample tilt and rotation are possible.

For higher resolution imaging Transmission Electron Microscope (TEM) facilities are available at CIME; samples preparation and investigation were performed by CIME's staff. The Philips CM300 TEM offers a resolution of 1.7 Å at 300kV.

3.4.2. Chemical composition

Electron Dispersive X-ray spectroscopy (EDX) can measure the chemical composition of samples. An Inca system is installed on the SEM and can easily quantify the atomic percentage of an element present in the sample under investigation with a precision of about 5%. The volume of analysis depends on the acceleration voltage of the incident electron beam thus the depth of analysis can be adjusted but the acceleration can not be decreased too much in order to generate enough x-rays.
For more precise chemical composition analysis we have X-ray Photoelectron Spectroscopy (XPS) which is a chemical surface analytic technique. The analyzed depth is typically between 1 to 10 nm according to the x-rays energy and the angle of measurement; depth profiling can be carried out using sputtering of the surface with energetic ion.

3.4.3. Thickness homogeneity

Thin films thickness can be measured by NanoSpec 6100 system which is an automated film thickness measurement system based on the principle of spectral reflectometry (480 - 800 nm) and designed to measure the thickness of films deposited on various substrates. Wafers up to 200 mm diameter with films thicknesses of 100 Å to 20 μm can be measured. Thickness cartography and homogeneity can be calculated from the sample refractive index given as function of the wavelength.

3.4.4. Surface topography

Thickness line profiles could be measured by Tencor Alpha Step 200 stylus profilometer. The stylus has a diameter of 12.5 μm and the claimed vertical resolution is 5 nm.
Three dimensional accurate topography imaging of an area smaller than 100×100 μm^2 can be performed with a Nanosurf Atomic Force Microscope (AFM). The axial resolution is 1 nm and only contact mode can be performed with this tool.

3.4.5. Crystalline structure

X-ray Diffraction (XRD) allows crystalline structure and phase identification. Monochromatic x-rays are reflected by the atomic planes of crystals; the possible diffraction peaks due to constructive interference are obtained for an angle corresponding to the specific distance between two planes according the Bragg's law. The measurements were done in the Ceramics Laboratory at EPFL on a 2 theta Siemens Diffractometer D500.
The crystalline structure of a material can also be analyzed from TEM diffractive pattern.

3.4.6. Optical properties

The optical properties of thin films can be investigated with the help of a spectral ellipsometer, indeed refractive index (real and imaginary parts) in function of wavelength and film thickness can be obtained by this technique. We have at disposition in our clean room facilities (Center of MicroNanotechnology) a Sopra GES 5E spectral ellipsometer working from 185 nm to 2500 nm wavelength, under 20º to 90º incidence angle and with a spectral resolution < 3 nm.

3.4.7. Infrared and Raman spectroscopy

Fourier Transform Infrared spectroscopy (FTIR) was performed with a Perkin Elmer 300 system. The wavenumber range available is 500 to 4000 cm^{-1} and the tool was used in Attenuated Total internal Reflection (ATR) mode. Each spectrum was acquired with an average of 64 measurements.
Raman analysis was performed in the Swiss federal laboratories for materials testing and research (EMPA) in the range of 1000 to 3000 cm^{-1}. The measurements were carried out with a confocal, reflective-type triple monochromator micro-Raman spectrometer (Dilor XY 800). An argon ion laser operating at 514.5 nm wavelength was used as the excitation source (Coherent Innova 90) and a liquid-nitrogen cooled CCD was used as a detector (Wright Instruments).

3.4.8. Waveguiding properties (OLCR)

Optical low-coherence reflectometry (OLCR) is an interferometric technique that allows measurements of the amplitude and the phase of the light reflected from the device under test. It is based on a broadband light source, a Michelson interferometer, and on coherent signal detection. OLCR is an efficient tool for

measuring optical reflectivity as a function of distance and has demonstrated both high spatial resolution (< 20 μm) and reflection sensitivity (< -160 dB).

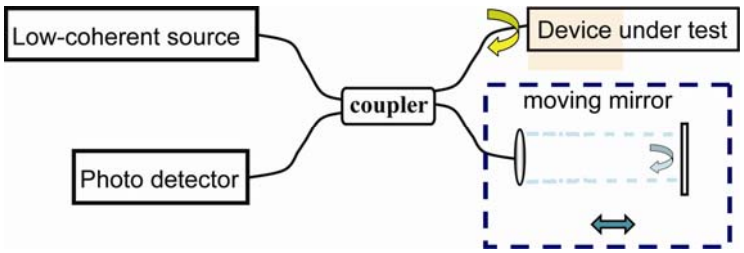

Figure 42 OLCR setup.

As shown in Figure 42 , the low-coherence source signal is divided between the reference and test arms. The optical delay (light propagation time) in the reference arm can then be varied by movement of the reference mirror. The reflected signals from each arm travel back through the coupler, where they are recombined and received at the photodiode. By nature of the coupler, half of the reflected power will be directed back to the source where it is attenuated by the isolator. From the arrangement shown above, an interference signal will appear at the photodiode if the difference in optical length between the reference and test arms is less than a coherence length.

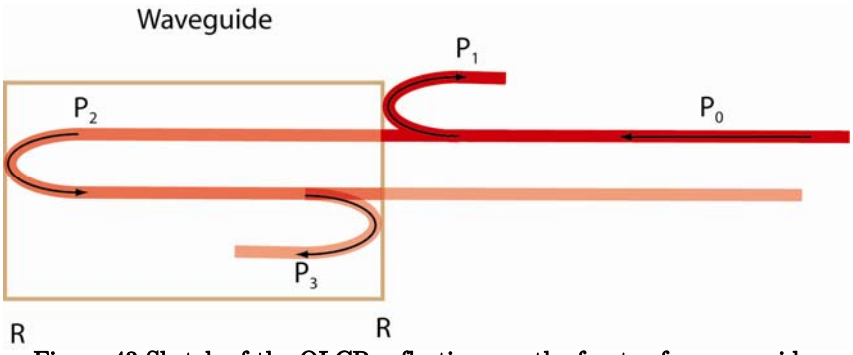

Figure 43 Sketch of the OLCR reflections on the facets of a waveguide.

The waveguide net propagation loss coefficient is given by: $\alpha = -\frac{1}{2L} ln(\frac{1}{R_f^2}\frac{P_3}{P_2})$,

Where L is the length of the waveguide, R the Fresnel reflection coefficient and P_i the reflection peaks. The main advantage is that the loss measurement is independent of the coupling efficiency. But the waveguide facets must be parallel and polished.

The waveguides were characterized with a HP OCLR at 1.55 μm wavelength.

3.5. Summary and conclusion

A functional high vacuum CVD reactor (10^{-7} mbar background pressure) has been realized and characterized. Heater with high emissivity is needed to reach the maximum substrate temperature; the maximum substrate temperature obtained is 700 °C. This limits the deposition to amorphous alumina. The precursor flow is set by controlling the pre-chamber pressure. A reliable in situ reflectometry system allows to follow in real time the growth rate of the deposition. Alumina thin films with 95% thickness uniformity are deposited with the help of the original design of the effusing source. Simulations and measurements are in good adequacy.

The substrate can be locally irradiated with a 248 nm laser, the maximum fluence is 400 mJ/cm^2 and the maximum repetition rate is 400 Hz. Microstructures with 80 µm resolution are demonstrated.

Reproducible alumina thin films can be deposited under different conditions in high vacuum and local microstructures can be induced by laser or electron beam.

Chapter 4 Precursors

4.1. Introduction

In order to control perfectly a CVD process, the behavior of the precursor should be understood and predictable. That is the reason why in the following paragraphs we study the chemical and physical properties of the chemical compounds used in this work, as well as the temporal evolution of precursor properties for different precursor thermal history. We focus on vapor pressure and decomposition of the precursors.

4.2. Aluminum isopropoxide (ATI)

The ATI is a cheap but water sensitive alkoxide precursor able to form pure alumina films in CVD conditions, see Chapter 2.

Name	CAS	Formula	Simplified Structure	State	Price (50 g)
ATI	555-31-7	$Al[OCH(CH_3)_2]_3$	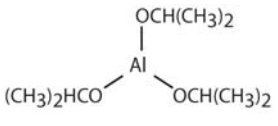	White solid (@ RT)	273.5 CHF (99.99%) or 23.8 CHF (98%)

Table 8 ATI general information.

Some properties are listed in Table 9 below.

Molecular weight (AMU)	Density (g/cm^3) @ 20 °C	Boiling point (°C) @ 10 Torr	Melting point (°C)	Flash point (°C)
204.25	1.035	135	138-142 (99.99%)	16

Table 9 ATI properties.

The ATI has a molecular structure made of oligo-nuclear units $[Al(O^iPr)_3]_n$. The degree of association n varies with physical state, thermal history and storage conditions [96]. The presence of trimeric and tetrameric molecules in the gas phase of ATI depends also of the thermal history and if the vapor is obtained by sublimation or by evaporation from the melt.

Measurements of the molecular weight of solid aluminum isopropoxide in benzene solution show that the precursor has the tetrameric form, see Figure 46 [97]. Bradley

suggests as well that an alkoxide undergoes the minimum degree of polymerization consistent with the attainment of the maximum covalency of the metal, leading in these conditions to the tetrameric structure in the case of the ATI [98].

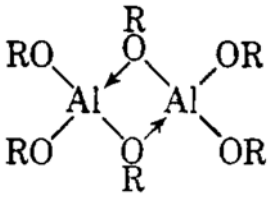

Figure 44 Dimeric structure of ATI.

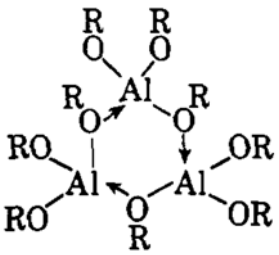

Figure 45 Trimeric stricture of ATI.

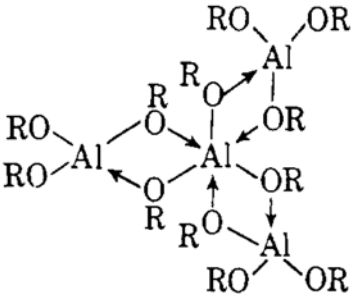

Figure 46 Tetrameric structure of ATI.

Where R is isopropyl group

The tendency of molten aluminum isopropoxide to supercool, giving a viscous liquid which is stable for several days at room temperature before undergoing slow crystallization, has been observed during the experiments of this work and has been previously recorded [99]. However, measurements of the molecular weight of molten aluminum isopropoxide dissolved in benzene show that the average degree of polymerization is 2.83, suggesting that it is mainly trimeric, see Figure 45. Other polymers can certainly exist in the melt, but this confirms the observation of Mehrotra [100] that freshly distilled ATI is trimeric, but slowly rearranges to the tetramer.
Finally, the dimer (Figure 44) has been shown to exist, though observed only in the vapor phase [97].

Concerning the vapor pressure, several studies report ATI vapor pressure against temperature but the results differ slightly as reported on Graph 14. In 1957, Wilhoit reported that the ATI vapor pressure is time dependant [101]. Moreover, the vapor pressure of ATI is a complex function of its thermal history and can decrease gradually [78].

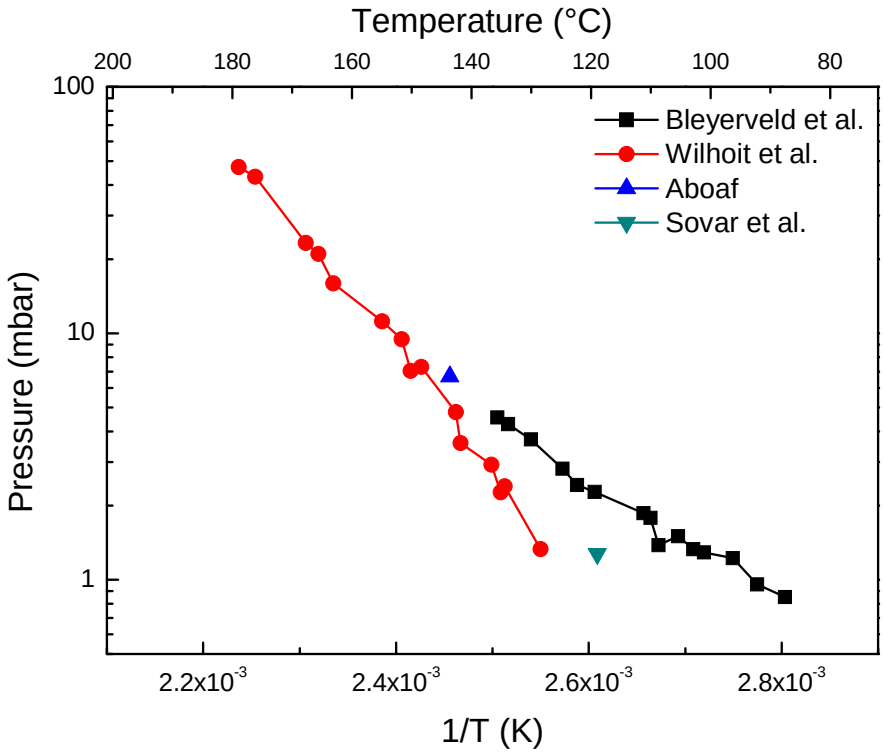

Graph 14 ATI vapor pressure in the literature [31, 96, 101, 102].

Despite that aluminum isopropoxide can be used to deposit alumina thin films with good reliability, any attempt to derive quantitative values of vapor pressure and vaporization rate will stay dependent of the technique, the equipment, the procedure and particularly the history of this precursor.

We also observed in our experiments that the vapor pressure of ATI decreases according to the time and can influence the growth rate of alumina thin films. Indeed, a glass reservoir was filled in a glove box (purged with nitrogen, relative humidity $5.1 \cdot 10^{-3}$ % at 20 °C) with fresh aluminum isopropoxide, then connected to our HV-CVD reactor and heated to 140 °C (all the connecting pipes are heated to 150 °C to avoid precursor condensation). We pumped continuously on the reservoir and the pressure in the precursor line was recorded versus the time. We observed that the pressure was not constant and decreased with time as represented by the two square symbol series of measurements on Graph 15.

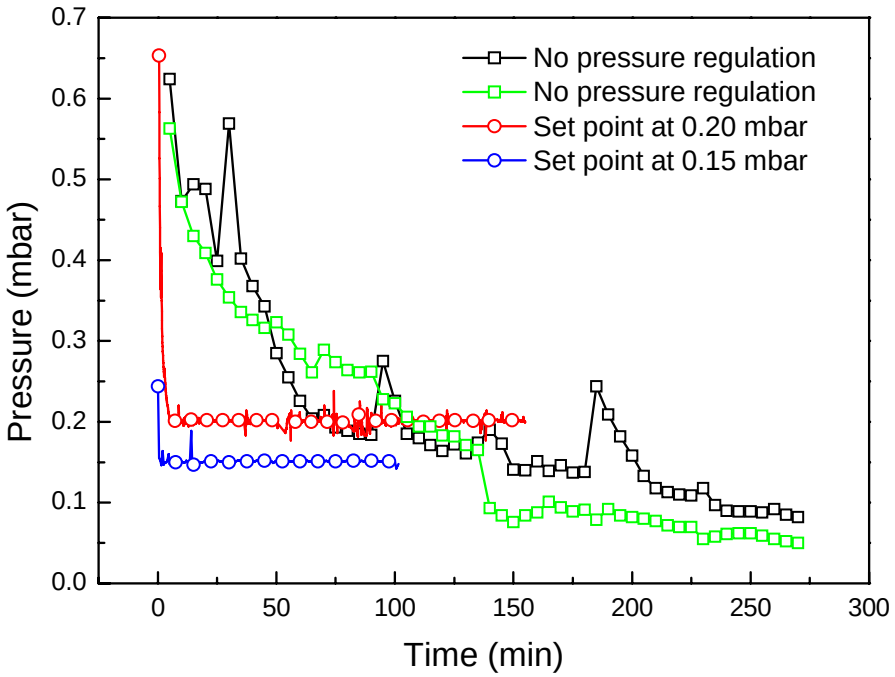

Graph 15 Evolution of the pressure versus time in the precursor line for ATI at 140 °C, in black and green: normal evaporation, in red: with regulation and a set point of 0.20 mbar and in blue: with regulation and a set point of 0.15 mbar.

We know from section 3.3.2 that the precursor pressure is proportional to the precursor transport. If the pressure decreases, i.e. the flow of precursor molecules decreases, and we are working in the mass transport limited regime the growth rate will be influenced. To avoid growth rate variations, we have to guarantee a constant flow of precursor. That is the reason why we installed a regulation system, described in the section 3.2.3, to control the pressure and in the same time to regulate the precursor flow. In that manner, an evolution of the vapor pressure of the precursor due to its thermal history can be overcome. The influence of the precursor flow on the deposition is studied in 5.1.2 and proves the importance of the pressure control setup. The pressure can be controlled for several hours, 0.20 mbar is a typical pressure used for the deposition of alumina; that corresponds to a precursor flux of $1 \cdot 10^{16}$ molecules/s·cm^2, based on measured mass loss. In these conditions, alumina growth rates of 30-60 nm/min can be obtained in function of the deposition temperature.

From all the publications about aluminum isopropoxide it becomes clear that aging effect influences the precursor properties. Sovar et al. [96] demonstrated by FTIR measurements the modification of ATI after a long period in air; already after two

weeks the peaks due to the alkyl part of the isopropanol have disappeared and a peak indicating the presence of aluminum oxide or aluminum hydroxide appeared. So, exposition in air (especially to water) and aging change the precursor composition and its volatility due to formation of oxide and release of volatile species. Then, in order to check the influence of the temperature on this chemical compound, Sovar et al. also measured by Thermal Gravimetric Analysis (TGA) and Differential Thermal Analysis (DTA) the behavior of ATI with a heating rate of 2 °C/min in the temperature range of 25-550 °C and a nitrogen gas flow of 1.5 l/h.

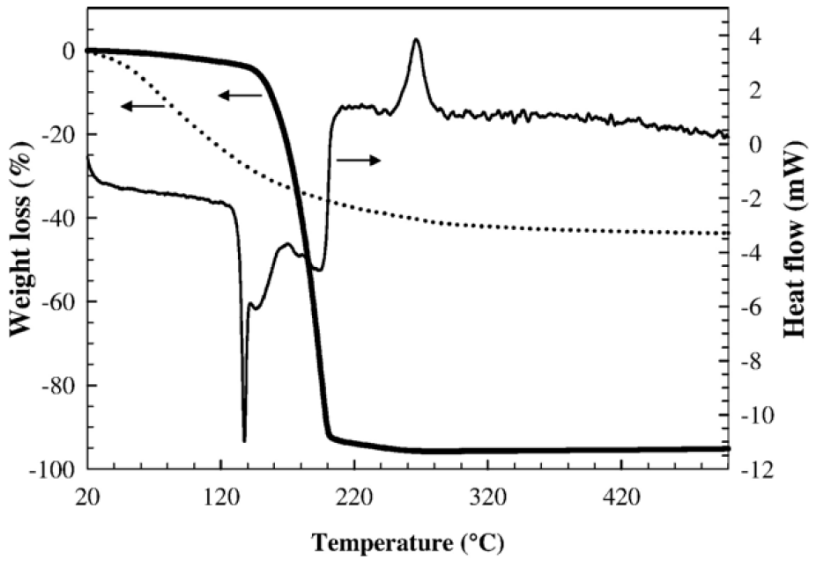

Graph 16 Arrows to left: Thermal Gravimetric Analysis (TGA) of ATI, the black line describes the thermal evolution of fresh ATI and the dotted line of ATI maintained at 110 °C for 15h in nitrogen. Arrow to right: Differential thermal analysis (DTA) curve of fresh ATI [96].

In Graph 16, for fresh ATI, we observe, in the weight loss versus temperature, that the weight loss starts from the beginning of the heating process. The loss between room temperature and 137 °C can correspond to the vaporization of volatile species such as propanol. Then 90% of the weight is lost between 137 °C (melting point) and 200 °C by evaporation of the precursor. Finally a small weight loss occurs between 200 °C to 250 °C that can be explained by decomposition of residual species in alumina. The chosen parameters of the TGA measurements are commonly used, nitrogen flux and atmospheric pressure except the heating rate of 2 °C/min that may promote decomposition compared to the standard rate of 5 °C/min usually used to avoid or decrease decomposition.

It is obvious on this graph that the precursor with a thermal history behaves differently in terms of weight loss (see dotted line).

Oligomerization of the precursor takes place from thermal treatment and influences the transport capabilities of ATI.

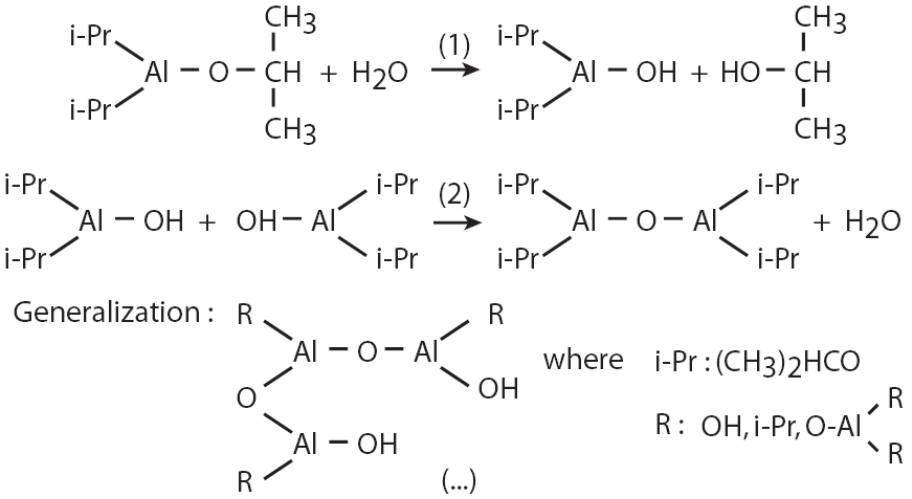

Figure 47 Possible reaction of aluminum isopropoxide with water to form oligomer chains.

Indeed, as illustrated in Figure 47 (1), an ATI molecule can react with water to produce isopropanol and form a hydroxyl group on the aluminum atom. Then two hydroxylated molecules can interact to form an Al-O-Al bond by condensation reaction, see reaction (2). In that manner, we can generalize the process to finish with chains of …Al-O-Al-O-Al… ended with different possible group: -OH or isopropyl groups for instance. This polycondensation can happen in three dimensions and explain that the precursor, initially a white powder, remains as yellowish viscous liquid after heating and pumping on it, as well as the diminution of the precursor transport in the deposition system.

The DTA curve shows four endothermic peaks: the first one at 137 °C corresponds to ATI melting. Then the broad peak is due to vaporization of volatile organic compound; from 170 to 210 °C, there is a peak that may be associated with the 90% weight loss due to precursor evaporation. Finally, the exothermic peak around 270 °C can come from partial decomposition of the precursor to Al_2O_3.

According to Graph 16 a precursor temperature of 130 to 150 °C is recommended to transport the precursor by evaporation, indeed the weight loss is high enough and no decomposition takes place. For the major part of our experiments we heated the precursor to 140 °C, which corresponds to a vapor pressure of about 7 mbar according to Graph 14, large enough to transport efficiently the precursor in direction of the substrate in the HV-CVD machine.

Concerning the thermal decomposition of the aluminum isopropoxide, we are interested in the molecule bonds Al-O and O-C in particular, because to form Al_2O_3

we have to separate the organic part of the molecule. Al-O with an energy of 511 kJ/mol [74] are stronger than O-C with an energy of 200-300 kJ/mol [11], so it is easier to separate the propyl chain than to break the aluminum-oxygen bond considering only the thermodynamic bond energies.

Several precursor decomposition models are proposed in the literature but none is properly experimentally demonstrated or proven.
Shulman et al. [103] proposed the following mechanism:

$$Al(OC_3H_7)_3 \rightarrow Al(OH)_3 + 3\,C_3H_6 \quad (1)$$
$$Al(OC_3H_7)_3 + 3\,H_2O \rightarrow Al(OH)_3 + 3\,C_3H_7OH \quad (2)$$
$$2\,Al(OH)_3 \rightarrow Al_2O_3 + 3\,H_2O \quad (3)$$
$$3\,C_3H_7OH \rightarrow 3\,H_2O + 3\,C_3H_6 \quad (4)$$

The alkoxide precursor is decomposed by pyrolysis to hydroxide and propene (1) or by hydrolysis to hydroxide and propanol (2). The hydroxide produced by (1) and (2) is dehydrated to form aluminum oxide in the reaction (3). Finally the propanol alcohol can be decomposed into water and propene (4). Notice that the water produced in (3) and (4) participates in (2). In brief the system produces alumina, water and propene.
This relative simple model considers, in reaction (2), that each isopropyl group reacts with a water molecule. So we have a complete decomposition to alumina, however the same reactions as presented in Figure 47 can take place and hydroxylated forms of alumina can be incorporated in the film, as shown in Chapter 5.

The second model, developed by Morssinkoff [35] but already suggested by Barybin et al. [32] in a simplest way, is based on the β-hydride elimination mechanism.

$$Al(OC_3H_7)_3 \rightarrow C_3H_7O - Al = O + C_3H_7OH + C_3H_6$$
$$C_3H_7O - Al = O \rightarrow AlO(OH) + C_3H_6$$
$$2\,AlO(OH) \rightarrow Al_2O_3 + H_2O$$

The final products are also alumina, water and propene. Morssinkoff claims that ATI decomposition takes place above 225 °C and $Al(OH)_3$ can not exist at that temperature, thus the presence of AlO(OH) is most probable. This reaction path can partially explain the presence of OH-group in the deposited film. Indeed low deposition temperature can induce the incorporation of hydroxyl and will be discussed later.
In presence of oxygen, aluminum isopropoxide can be decomposed following this reaction: $2\,Al(C_3H_7O)_3 + 27\,O_2 \rightarrow Al_2O_3 + 18\,CO_2 + 21\,H_2O$ developed by Niska et al. [37]. Again this reaction is theoretical and will not happen exactly like that during

the decomposition but the creation of CO_2 by adding oxygen is conceivable. As presented in the section 5.1 adding oxygen decreases the activation energy of the decomposition process.
The decomposition of ATI is not studied in details in this thesis but the existence of $Al(OH)_3$ or C_3H_7-Al=O seems to be not very realistic because the standard aluminum coordination is not satisfied [96].

Besides these concerns about stability, thermal behavior and decomposition reported in the literature and observed in our experiments, we can conclude that the decomposition of ATI in CVD conditions gives reasonable quality films with reproducible growth rates using the precursor charge for a limited period of time, typically few hours of deposition [78, 96].

In the case of laser induced HV-CVD two different processes are distinguished: pyrolitic and photolytic. In the second case the decomposition of the precursor take place from the interaction of photon and precursor molecules. In consequence the absorption of the precursor at the illumination wavelength plays a key role. The ATI absorption cross section curve is represented from literature in Graph 17 in the range of 100 to 200 nm and shows low UV absorption near 200 nm.
Our illumination source at 248 nm wavelength has a larger wavelength than in Graph 17 but seems not to be really well absorbed by ATI according to the literature [17, 63, 64].

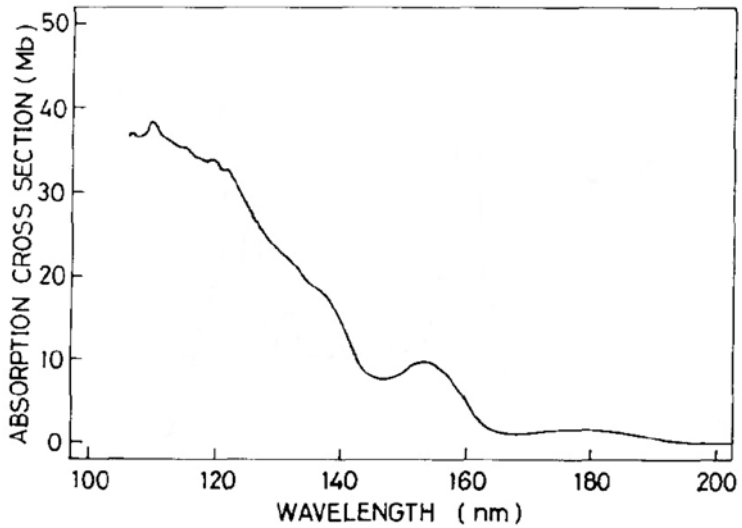

Graph 17 Aluminum isopropoxide absorption in the UV range (1Mb =10^{-21}cm^{-2}) [64].

Chapter 5 Alumina thin film deposition by HV-CVD

5.1. Study of the deposition process using ATI

5.1.1. Pre-deposition preparation

Sample preparation

Clean room quality Si wafers are used as substrates. The substrates are installed on the holder via the load lock in the reactor. Then they are heated during fifteen minutes at 500 °C under 1 sccm oxygen flux, in order to burn organic contamination. Finally the substrate is thermostated at the deposition temperature (200-700 °C) in high vacuum.

Precursor preparation

Clean glass reservoir is filled with fresh ATI precursor and tightly closed in a glove box (nitrogen atmosphere) to avoid exposition to air. After that, the reservoir is connected to the high vacuum chamber and finally we pump directly on the precursor kept at room temperature for fifteen minutes to remove nitrogen excess and other volatile species. At least one hour before deposition experiments the reservoir is heated to the desired temperature (130-150 °C). The usual reservoir temperature in this work is 140 °C. The gas line and the pre chamber are heated 10 °C higher than the reservoir to avoid precursor condensation on the walls of the tubes.

Reactor preparation

The chamber background pressure before deposition is in the order of $2 \cdot 10^{-7}$ mbar. The cryopanel is filled with liquid nitrogen at least thirty minutes before deposition.

5.1.2. Growth behavior

We studied the growth of alumina thin films from the thermal decomposition of aluminum isopropoxide in high vacuum environment in presence or not of reactive gases (O_2 or N_2O), in the temperature range of 200-700 °C and for different precursor fluxes. During each deposition the substrate temperature, the chamber pressure, the gas lines pressure and the in situ reflectometry signal are recorded.

In a first time, the growth kinetic of ATI decomposition is studied; indeed we reported the growth rate in function of the temperature, as illustrated on Graph 18.

The deposition conditions are: chamber pressure of 10^{-6} mbar during the process, precursor flux of $1.5 \cdot 10^{16} \pm 1.1 \cdot 10^{15}$ molecules/cm^2·s and deposition for thirty minutes. Assuming that all the precursor molecules impinging on the substrate surface are immediately decomposed, two aluminum isopropoxide molecules are needed to form one Al_2O_3 molecule and that the density of alumina is 3.99 g/cm^3 the maximum theoretical growth rate would be 0.19 µm/min.

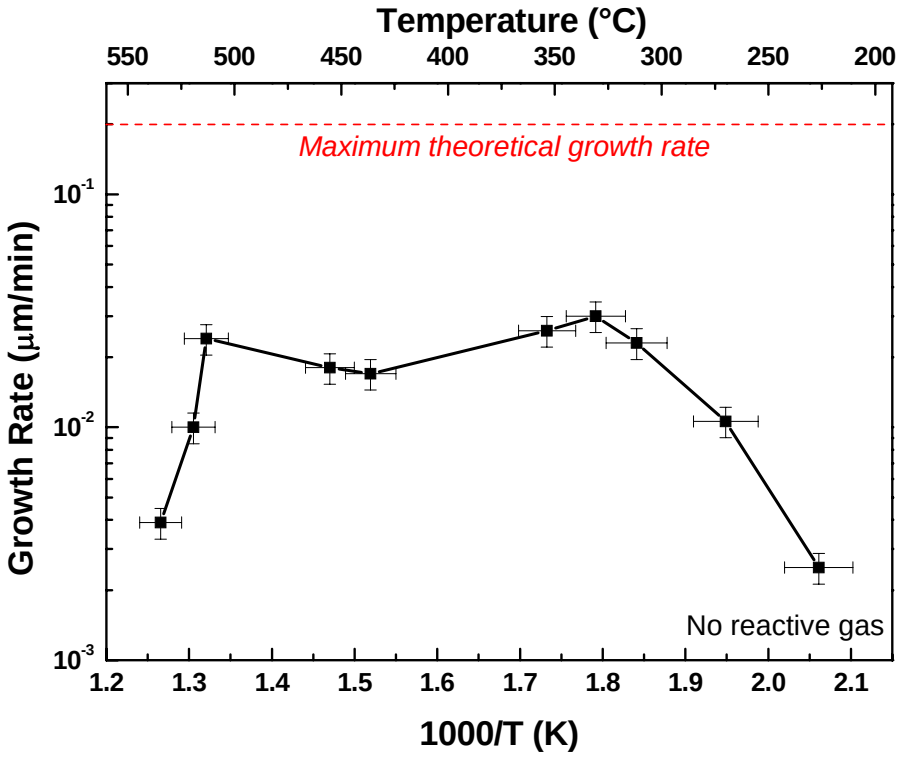

Graph 18 Arrhenius plot for alumina thin films deposited from ATI in HV-CVD.

The relative error on the temperature is 2% and corresponds to the variation observed experimentally of the PID regulation of the inductive heater and the intrinsic error of the K-type thermocouple used to measure the temperature. The 15% relative error on the growth rate is the combination of the error of the in situ reflectometry system and the dispersion of the measurements; each point was reproduced twice.

In a first approximation, we clearly distinguish three different regimes as predicted by the CVD growth behavior presented in 1.3.2. From 200 to 325 °C the chemical reaction limited regime, from 325 to 510 °C the mass transport limited regime and at higher temperature the desorption regime.

In the chemical reaction limited regime, where the growth rate depends mainly on the substrate temperature, and for a given precursor flow we can calculate the activation

energy from the slope of the straight line, within the measurements accuracy, using the Arrhenius equation and assuming that the surface is precursor saturated. As shown on Graph 19, the activation energy is 33.1 ± 8.2 kJ/mol, the linear fitting is represented in red, while the two extreme cases are represented in green and blue respectively; and allow to estimate the error on the activation energy. This value corresponds to what Morssinkhof et al. also observed in almost similar conditions [35].

We have to precise here that it is not a true Arrhenius plot since the ordinate is a combination of rate constant and a concentration term which can vary with temperature. The sharp changeover between chemical reaction limited regime and the mass transport limited regime is in reality a large transition region between the two. This means that although the low temperature region may appear linear the growth rates will be under mixed control with both kinetic and transport contributions. The apparent activation energy from the low temperature linear region could be less than the true energy of activation for the kinetic process.
In HV-CVD the growth rate is never strictly chemical reaction limited. Desorption plays already a role at low temperature. Indeed, competition between adsorption, desorption and decomposition takes place along all the temperature range [104].
Mechanisms at high temperatures would in principle include a temperature activated desorption of the precursor molecules so rapid that only a fraction of the adsorbed precursor would have time to dissociate.

By keeping the same deposition conditions as before but adding an oxygen flow of one sccm during the deposition process we obtain the same kind of Arrhenius plot but with an activation energy of 11.39 ± 5.31 kJ/mol, as presented on Graph 20; this value is in agreement with the work of Saraie et al. [34] and Sovar et al. [96] where 18.8 kJ/mol and 12.0 kJ/mol were measured, respectively. We also observed that adding 0.2 sccm oxygen during deposition has no effect on the activation energy; indeed we measured an energy of 35.2 ± 9.4 kJ/mol.
The 0.2 sccm oxygen flux represents only 6.3% of the total flux (precursor + reactive gas) while 1 sccm is 25.2% of the total flux. The 0.2 sccm flux is too small to have quantitative effect on the activation energy.

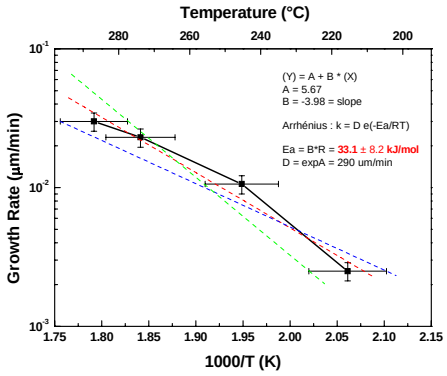

Graph 19 Activation energy for ATI decomposition.

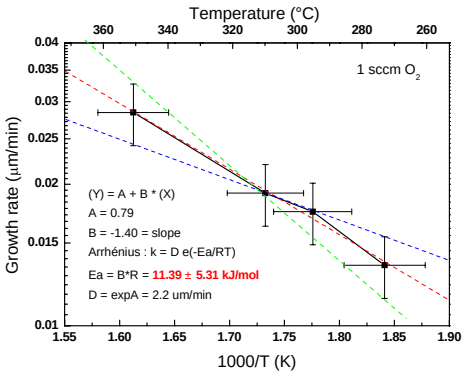

Graph 20 Activation energy for ATI decomposition in presence of 1 sccm oxygen.

The same experiment was done in the same conditions replacing the oxygen flux by one sccm N_2O flux. This reactive gas has no effect on the activation energy. The measured activation energy in presence of nitrous oxide is 30.5 ± 11.4 kJ/mol.

Nitrous oxide is usually used in plasma enhanced CVD [61] or laser induced CVD [62] where N_2O is decomposed by ions or photons. The temperature range used in this thermal deposition seems to be not large enough to decompose N_2O in active species able to decrease the activation energy of the reaction. N_2O seems to block the surface and avoids deposition until high temperatures, and then it desorbs and does not do any positive effect on the decomposition.

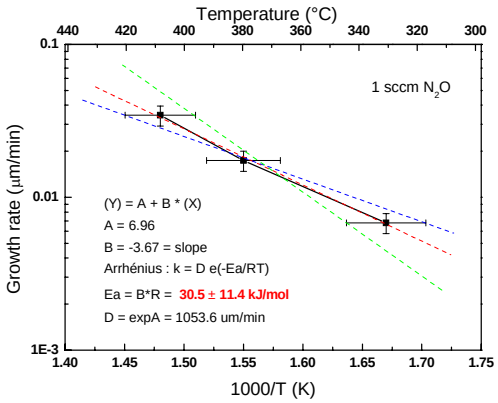

Graph 21 Activation energy for ATI decomposition in presence of 1 sccm N_2O.

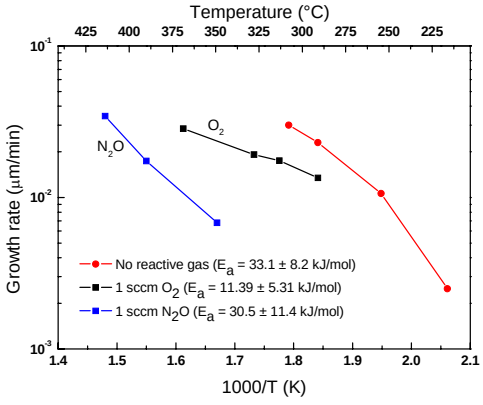

Graph 22 Comparison of activation energy for ATI decomposition: without reactive gas in red, 1 sccm O_2 in black, 1 sccm N_2O in blue.

We observe that the straight line of the chemical reaction limited regime in presence of N_2O is shifted to the left. Higher temperature is needed to reach the same growth rate. This might be explained by surface competition between reactive gas and precursor molecules. The nitrous oxide molecules cover locally the substrate surface

for a certain time and decrease the growth rate by decreasing the chance of precursor to be decomposed.

Now focusing in more detail on the mass transport limited regime we observe that we have two distinct trends. Even if a straight line can fit in the limit of the error bars, first the growth rate decreases between 325 to 430 ºC and then from 430 to 520 ºC increases again. In the first part the growth rate is limited by the quantity of precursor molecules impinging on the substrate surface and increasing the temperature decreases the residence time of a molecule. So the growth rate is limited by the precursor flux that is kept constant in this case. That means that the growth rate will stay constant by increasing the temperature but shorter residence time of a molecule induces a decrease of the growth rate. In the second part the augmentation of the growth rate can be explained by the fact that another chemical reaction path is promoted.
Finally the growth rate decreases drastically because of the main part of the molecules do not stay long enough on the substrate surface to be decomposed.

The growth behavior of the high vacuum chemical vapor deposition of aluminum isopropoxide follows the general trend of the empirical model established for standard CVD. But, due to the molecular beam of the precursor molecules and consequently the absence of collisions in the gas phase, the interaction between the substrate and the impinging molecules can be completely different than in CVD.

The HV-CVD approach stands out of all the other CVD methods as it allows excellent prediction of growth rates and film thickness homogeneities, if the decomposition probability of the precursor is known. We propose here to determine the decomposition probability. Assuming an impinging rate efficiency of 18% (see 3.3.3) the ATI precursor flow can be determined from the prechamber pressure. Consequently the total number of molecules impinging on the substrate surface is known. On the other hand, from the measured thickness of the deposit, we can determine the volume of the layer and then determine the number of Al_2O_3 molecules present in the deposit, assuming an average density of 2.7 g/cm^3 (see 5.1.5). With the approximation that 1 molecule of alumina comes from the decomposition of 2 molecules of aluminum isopropoxide, we can calculate the number of ATI molecules needed to create the thin film. The ratio of the number of ATI molecules in the deposit on the number of ATI molecules impinging on the substrate surface gives the probability of decomposition of ATI. We observe in Graph 23 that this ratio is function of the temperature.

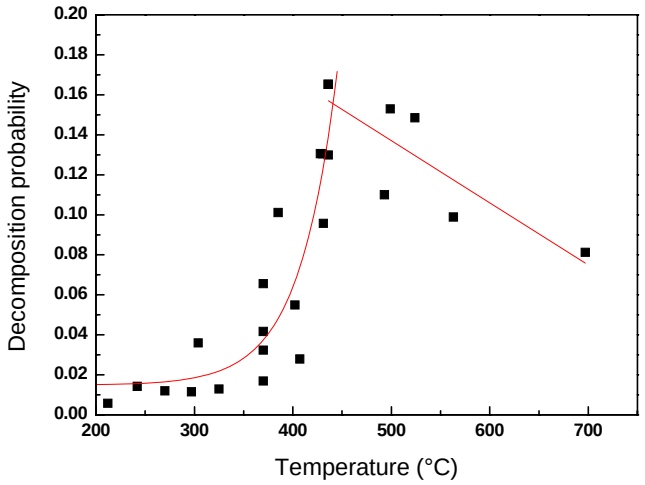

Graph 23 Probability of ATI molecules decomposition versus temperature. The red line is just guide for the eyes.

The maximum probability is about 0.17 at 425 °C. The errors are large on this estimated probability due to the different approximations. We observe that the probability increases with temperature until a maximum and then decrease certainly due to increased desorption rate. This decomposition probability is a good criterion for precursor selection of HV-CVD systems; the higher the probability the higher the growth rate. From 200 to 325 °C the probability is more or less constant because many molecules are on the substrate surface and surface competition takes place while between 325 to 450 °C the probability increases with the temperature. Indeed higher energy increases the probability of decomposition and no surface competition happens due to the lack of precursor on the substrate surface at this temperature range. The same behavior in observed in the case of the deposition of aluminum in UHV-CVD conditions from the decomposition of dimethylethylamine alane with a maximum probability of 0.13 [105]. This value is lower than expected based on the classical CVD processes, Karpov et al. assume that steric effects play a role.

To demonstrate the influence of the deposition parameters on the growth rate, in the different regimes, and to confirm that the delimitation of the regimes is correct, we used the in situ reflectometry setup to study in real time the behavior of the growth rate for temperature or precursor flow variations in the chemical reaction limited regime and the mass transport limited regime respectively.
In the temperature range of the chemical reaction limited regime, for a constant precursor flux and one sccm of O_2, by increasing the temperature after one period on the reflectometry signal, we observed (see Graph 24) that the period duration

decreased. That means, as expected in that regime, increasing the temperature enhances the growth rate.

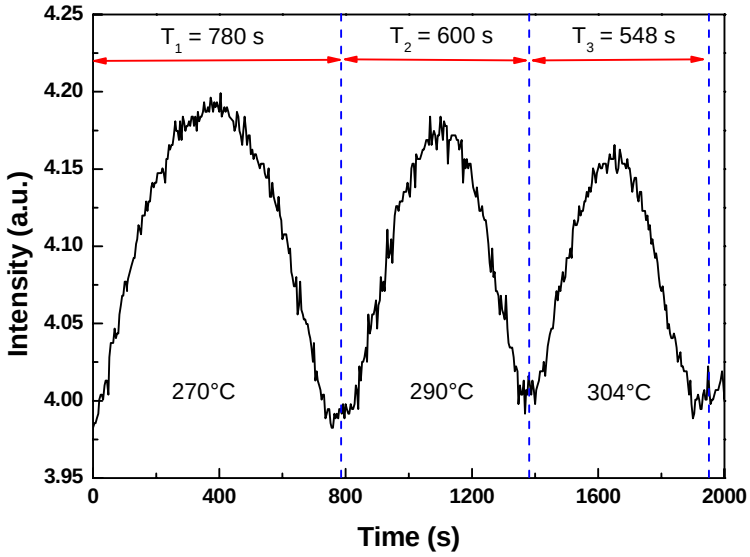

Graph 24 Evolution of the reflectometry signal for temperature increase in the chemical reaction limited regime.

Temperature (°C)	Period (s)	Growth rate (nm/min)
270	780	13.45
290	600	17.49
304	548	19.15

Table 10 Influence of the temperature on the growth rate in the chemical reaction limited regime.

On the other hand with a constant temperature of 510 °C (mass transported limited regime) and an oxygen flux of 0.2 sccm the growth rate is dependent of the precursor flow. Indeed, as demonstrated on Graph 25, if we decrease the precursor flow during the deposition, the growth rate follows nicely the same trend. Experimentally, we decreased the precursor flow with the help of the regulation system after a certain time and the growth rate has been calculated from the reflectometry signal.

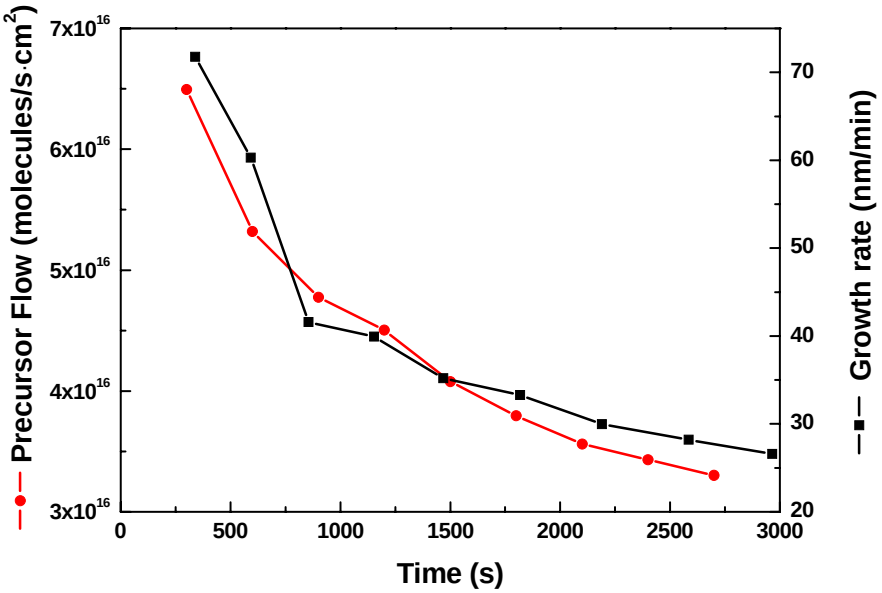

Graph 25 Temporal evolution of the growth rate for a given precursor flux in the mass transported limited regime.

Time interval	Precursor flow (molecules/s·cm^2)	Growth rate (nm/min)
1	$6.5 \cdot 10^{16}$	71.8
2	$5.3 \cdot 10^{16}$	60.3
3	$4.8 \cdot 10^{16}$	41.6
4	$4.5 \cdot 10^{16}$	40.0
5	$4.1 \cdot 10^{16}$	35.2
6	$3.8 \cdot 10^{16}$	33.3
7	$3.6 \cdot 10^{16}$	30.0
8	$3.4 \cdot 10^{16}$	28.2
9	$3.3 \cdot 10^{16}$	26.6

Table 11 Growth rate behavior for precursor flux modification in the mass transport limited regime.

So, we confirmed that the growth rate follows the precursor flux when the deposition takes place in the mass transport limited regime. And we observe that a diminution of the precursor flow by a factor two decreases the growth rate by a factor three in these deposition conditions.

The thickness of the films deposited in the mass transport limited regime has almost no temperature influence and gives homogenous films on wafer scale as demonstrated

in 3.3.3. Moreover, the films deposited in any regimes have homogenous structure surface, see Picture 12, no surface defects or impurities are present.

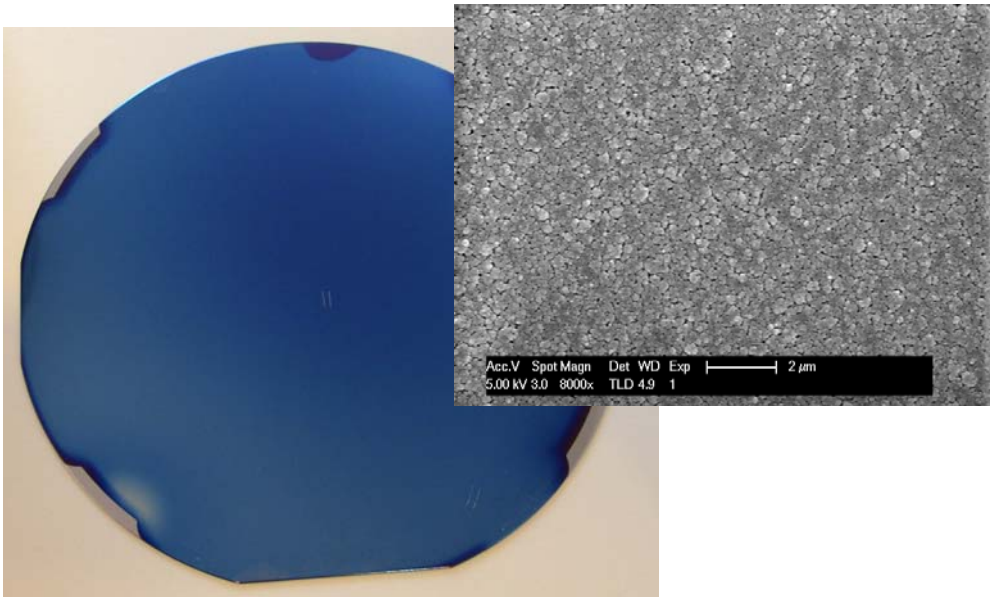

Picture 12 Homogenous (96%) alumina thin film deposited on Si wafer and detail of its microstructue for a substrate temperature of 424 °C.

The growth behavior of alumina from the decomposition of ATI in high vacuum has been studied according to the deposition temperature for a specific precursor flux. The measured activation energy of the reaction is in adequacy with the energies reported in the literature for low pressure CVD and smaller than for atmospheric CVD. Adding 25% of oxygen in the gas phase reduces the activation energy by a factor 3, less oxygen has no effect while adding more oxygen is not possible otherwise the molecular beam regime would not be guaranteed anymore. Nitrous oxide has no effect on the growth rate, the temperature is certainly too low to produce active species but higher substrate temperature is not obtainable in the reactor. The importance of the role of the precursor flux is demonstrated in the mass transport limited regime. And in particular, surface competition between molecules is important in HV-CVD as illustrated here with N_2O and confirmed in 5.2 during the co-deposition of alumina and erbium.

5.1.3. Chemical composition study

From EDX analysis, all the films deposited between 200 to 700 °C, in presence or not of reactive gases, under different precursor flux and at different chamber pressure are nearly stoichiometric: 65 ± 5 at% O and 35 ± 5 at% Al. No carbon contamination, nor

other elements, is measured by EDX in the alumina films. The little excess of oxygen can be explained by EDX sensitivity for light element or artifact from the quantification setup and by the fact that ATI molecule contains one Al for three O and induces oxygen incorporation. However, this excess can also come from the presence of hydroxylated form of alumina (diaspore or boehmite). Indeed, the theoretically stoichiometric ratio for Al_2O_3 is 60 at% O and 40 at% Al, but the ratio of AlO(OH) is 66.66 at% O and 33.33 at% Al. We observe that the films deposited between 250 to 400 °C have in average 66 %at O and 34 at% Al, whereas the films deposited between 450 to 700 °C have in average 61 at% O and 39 at% Al. Indeed, at higher temperature the film composition is expected to be closer to Al_2O_3.
The presence of OH is confirmed in Graph 26 by FTIR measurement and again low temperature deposits have a larger OH peak.

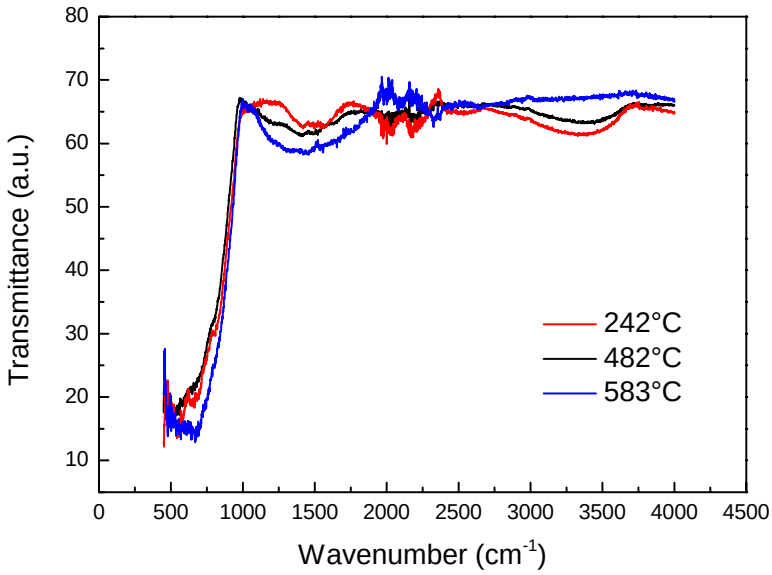

Graph 26 FTIR measurements of alumina thin films deposited at 3 different temperatures.

The two absorption regions between 500 to 1000 cm^{-1} and 1000 and 2000 cm^{-1} are assigned to the alumina [74, 96]. This broad feature, characteristic of alumina, between 500 to 1000 cm^{-1} is in fact the overlap of the O-Al-O bending mode (650-700 cm^{-1}) and the Al-O stretching mode (750-850 cm^{-1}) [106], while the wide absorbance region centered at 1345 cm^{-1} corresponds to Al=O [107].
The very broad absorption region from 2600 to 3800 cm^{-1} is characteristic of hydroxylated compounds, in particular O-H stretching mode [106]. The noise near 2000 cm^{-1} is due to the silicon substrate. High temperature deposits show well defined Al_2O_3 absorption band and no OH absorption peak, while lower temperature deposit

have a wide peak in the OH region. This confirms the presence of hydroxylated form of alumina, for instance AlO(OH).

In order to check in a more precise manner the chemical composition and to be sensitive to the depth of the film we investigated the atomic presence of the different elements by XPS before and after several sputtering cycles. As presented in the two graphs below we have pure alumina with the correct stoichiometry (60 at% O and 40 at% Al) from 10 nm below the surface. The important point here is that no carbon contamination is detected in the deposited material. This is crucial for the optical applications for which this material is destined. Indeed carbon will absorb the light and kill the waveguiding properties of the material. In our case the HV-CVD deposited alumina can guide light and propagation losses lower than 2 dB/cm are presented in paragraph 7.1.2.

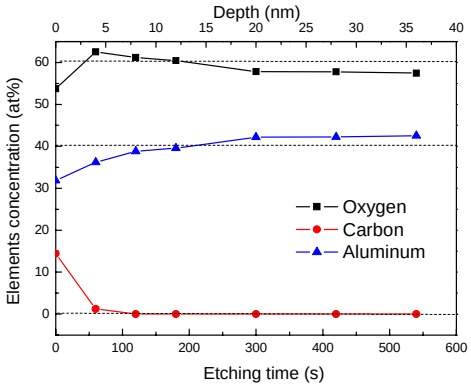

Graph 27 XPS of alumina thin films deposited at 482 °C.

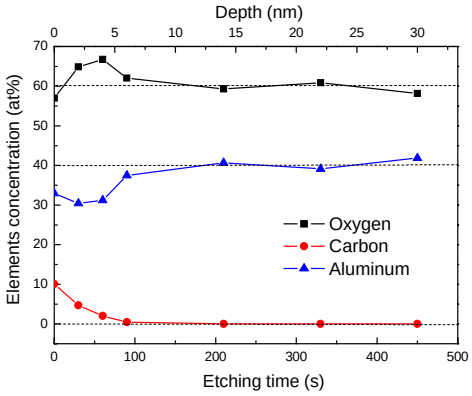

Graph 28 XPS of alumina thin films deposited at 242 °C.

Nevertheless about 10 at% carbon contamination was detected by XPS on the surface of the films. This carbon is probably mainly ex-situ contamination induced during the different characterization that the samples have sustained.

But we observed excess of oxygen in the film between 0 to 10 nm deep. Again that can be explain by the presence of AlO(OH) in the upper part of the films. In section 5.1.5 structural difference along the deposition will be presented and will be discussed taking into account the possible presence of hydroxylated species.

Pure stoichoimetric alumina thin films can be deposited by HV-CVD. Carbon contamination is not a problem; the precursor decomposes properly in Al_2O_3 but the presence of hydroxlated form of alumina is possible at low deposition temperature due to incomplete oxidation.

5.1.4. Optical characterization

The index of refraction and the extinction coefficient of the alumina layers were measured by spectral ellipsometry. We notice that the imaginary part of the refractive index, see Graph 30, increases above zero at wavelength shorter than 400 nm, when the extinction coefficient of alpha alumina is zero until 140 nm. This could come from either co-deposition of carbon due to incomplete decomposition of the precursor, certainly improbable according to the chemical composition analysis, or deposition of non-stoichiometric aluminum oxide, or from other effects, for example scattering in the films. Nevertheless, the extinction coefficient at 1.55 µm, wavelength of interest for the optical applications in telecommunication, is zero at any deposition temperature that is necessary for good light transmission in the material.

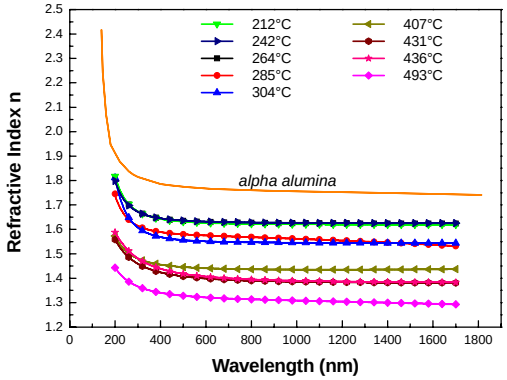

Graph 29 Refractive index of alumina thin films deposited at different temperature.

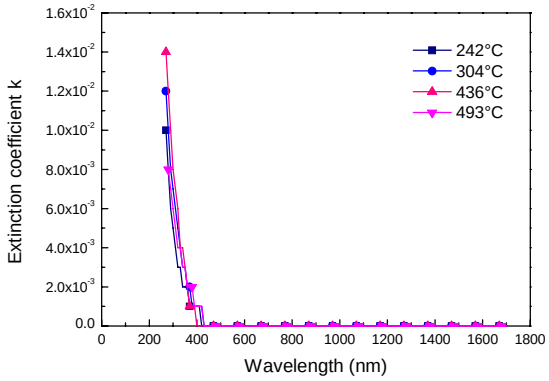

Graph 30 Extinction coefficient of alumina thin films deposited at different temperature.

The refractive index of this amorphous alumina (see section 5.1.5) varies in the range of 1.30 to 1.65 (at 632.8 nm wavelength) in function of the deposition temperature, as presented on Graph 29. Increasing the substrate temperature during deposition induces a decrease of the refractive index.

In order to check if the extinction coefficient values measured from 400 to 200 nm affect the optical quality of the films, we measured the transmission of alumina films deposited on quartz by HV-CVD with a spectrophotometer. The transmission of the as deposited alumina (Figure 48) is compared, in the range of 300 to 900 nm, to the transmission of pure crystalline alpha alumina (Figure 49).

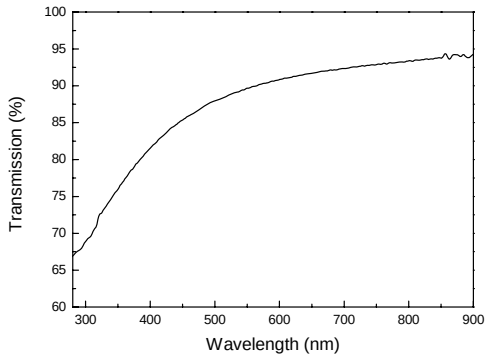

Figure 48 Transmission spectrum of alumina deposited by HV-CVD.

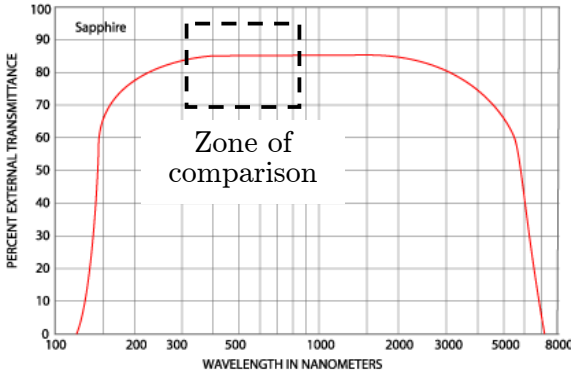

Figure 49 Transmission spectrum of pure sapphire [108].

We observe that the transmission decreases more in the deposited film than in pure sapphire, this can be due to absorption in the film, to scattering in the film or surface reflection. Indeed, the grains in the films can induce Rayleigh or Mie scattering, as presented in 5.1.5.

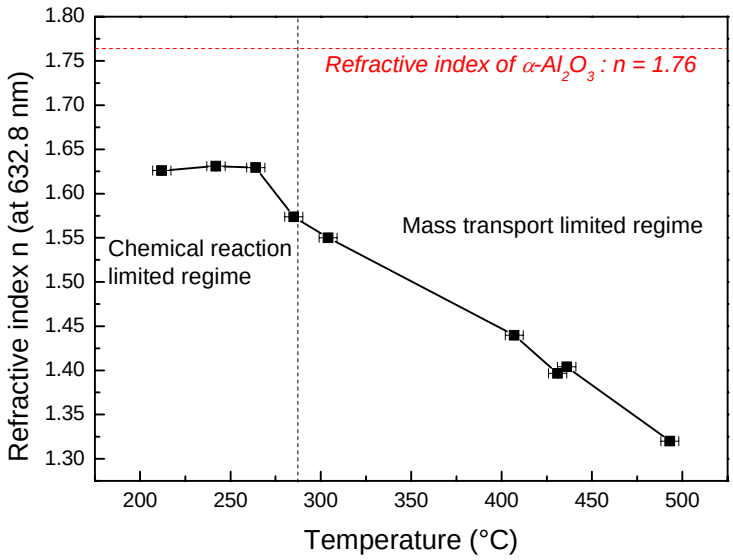

Graph 31 Thermal evolution of the refractive index of pure alumina thin films.

As shown in Graph 31, at low temperature (200-300 °C) or in other words in the chemical reaction limited regime we have a nearly constant refractive index of 1.63 at 632.8 nm. That means that the films are more dense but still much less compact as compared to crystalline sapphire with a refractive index of 1.76 at 632.8 nm. A simplified explanation could be that the deposition is controlled by surface reaction and the precursor molecules are not immediately decomposed after adsorption and

have time to diffuse into pores of the deposit resulting in denser films. On the other hand, at higher temperature or in the mass transport regime, the refractive index decreases by increasing the temperature. In this mass transport limited regime the growth rate is higher and leads to the formation of less dense and rough film. The decomposition is faster at higher temperature and a precursor molecule impinging on the substrate has a higher probability (see Graph 23) to be decomposed faster and directly where the molecule hits the substrate because this regime is limited by precursor transport. So the structure of the film shows lower organization as compared to low temperature deposition where the molecules have more time to find the most energetically favorable place in the film structure. Voids density and porosity increase therefore in the films deposited at higher temperature.

By varying the deposition temperature in the chemical reaction limited regime we can adjust the refractive index of the layer. This might be technologically very useful to create multilayers with different refractive indices as for instance wavelength selective dielectric filters or buried waveguides.

To complete the optical characterization of the thermal deposition of alumina we analyzed the films by Raman spectroscopy, see Graph 32. With a laser power of 1 mW, focusing to the diffraction limit and an acquisition time of 100 s, no Raman signals for carbon or alumina were detected. This confirms that no carbon agglomeration as contamination is present in the films and we conclude that the films are amorphous, as explained in more detail in the next section. Indeed amorphous alumina shows no Raman signal as reported in the literature [109, 110].

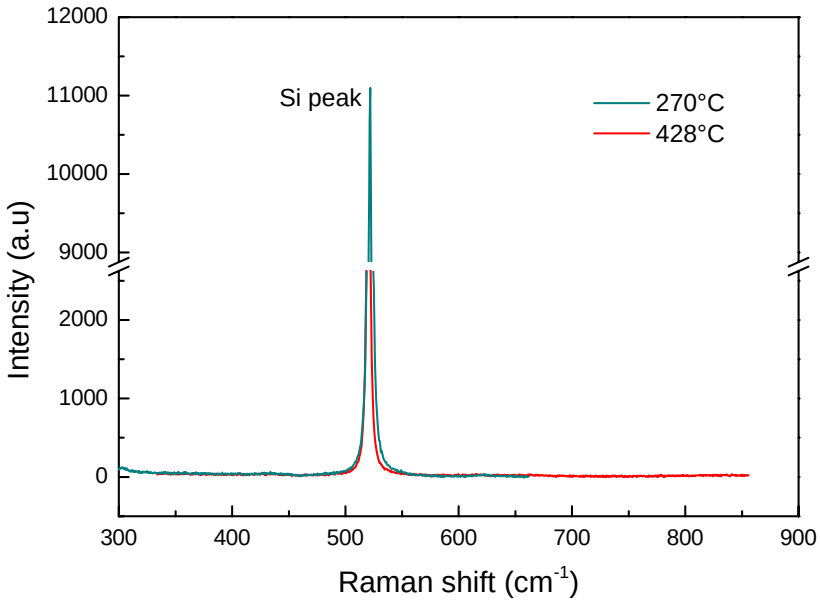

Graph 32 Raman spectrum of alumina deposited at 270 and 428 °C.

5.1.5. Structure characterization

The XRD measurements of the Al_2O_3 on Si, deposited between 300 to 700 °C, hint to an amorphous structure of the films; because only Si substrate peaks are identified in the diffraction spectrum, see Graph 32. The samples were characterized by grazing incident angle x-ray diffraction.

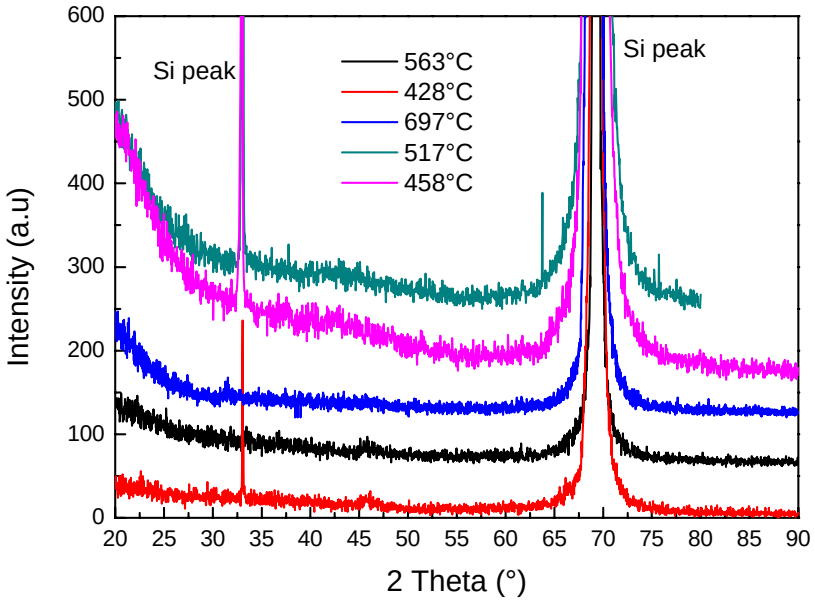

Graph 33 XRD spectra of alumina thin films.

For comparison, the XRD spectrum of alpha, gamma, theta and kappa alumina phases are reported in appendix 9.8.

More detailed structural investigations were achieved by Transmission Electron Microscopy (TEM) and confirmed the amorphous structure of the alumina films, but the formation of small crystallites induced by the electron beam (300 keV) was observed. Indeed, during TEM analysis, we observed that the film material crystallizes under the electron beam. This phenomenon is illustrated with the appearance of TEM diffraction patterns after a 5 min electron beam irradiation.

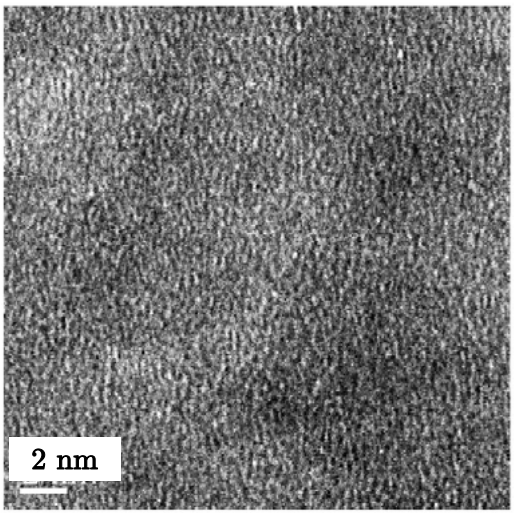

Picture 13 TEM image of amorphous alumina, as prepared.

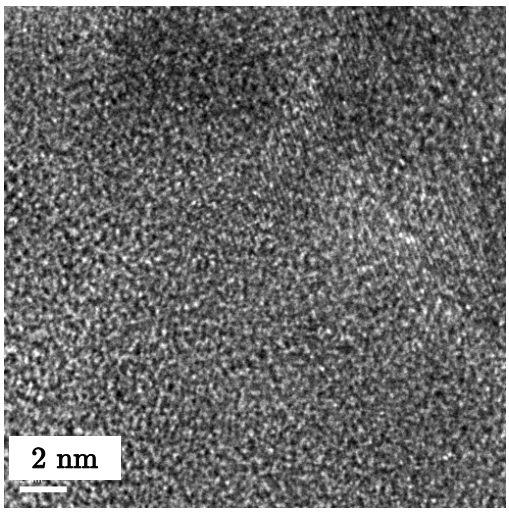

Picture 14 TEM image of alumina after 5 min irradiation (300 keV), presence of cristanillity.

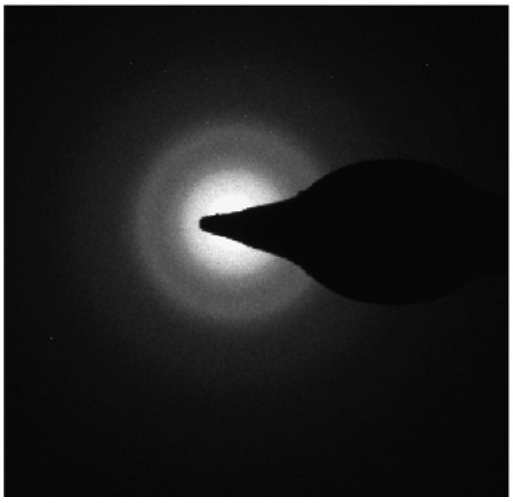

Picture 15 Diffraction pattern showing amorphous alumina, as prepared.

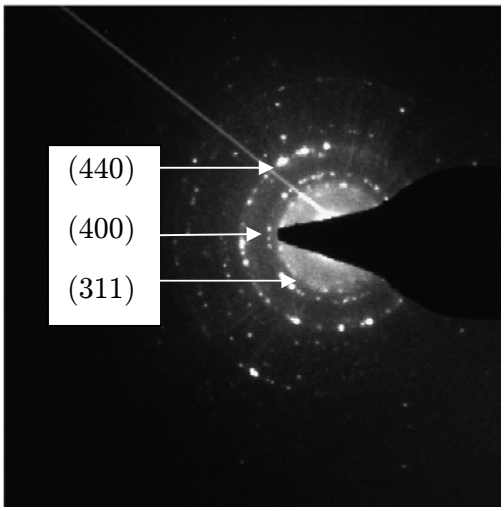

Picture 16 Diffraction pattern after 5 min irradiation showing the appearance of crystals.

This phenomena is commented in the literature as a crystallization of amorphous alumina in gamma alumina by electron beam heating [111, 112] or by the creation of defects induced by the impact of the electrons [113]. According to the indexation of the TEM diffraction pattern, we observe the apparition of gamma alumina confirming the first hypothesis.

XRD and TEM measurements prove that our thin films are amorphous after deposition. Another hint to the amorphous structure is the value of the refractive index (see section 5.1.4), much lower than 1.76 corresponding to the index of pure sapphire [30]. The density of the deposited film is lower than the density of the crystalline form, so our material is amorphous and not polycrystalline to the limit of 2 nm crystals. This is in good adequacy with the literature, where the reported

crystallization temperature (see paragraph 1.4) of the alumina occurs between 700 to 800 °C.

The density of the thin films can be expressed as function of the refractive index of the films and the bulk material based on the Lorentz-Lorentz effective medium equation [114]: $\frac{n_f^2 - n_h^2}{n_f^2 + 2n_h^2} = f_a \frac{n_a^2 - n_h^2}{n_a^2 + 2n_h^2} + f_b \frac{n_b^2 - n_h^2}{n_b^2 + 2n_h^2}$ for a heterogeneous composite of a host material h with a refractive index n_h and diluted phase a and b with refractive indices n_a, n_b and volume fraction f_a, f_b respectively.

In the case of porous film with n_f as refractive index, we have: n_h the refractive index of the bulk, $n_a = 1$ the refractive index of air and $f_a = (1\text{-}p)$ with p the packing density.

So, we have: $(1-p) = \frac{n_f^2 - n_s^2}{n_f^2 + 2n_s^2} \cdot \frac{1 + 2n_s^2}{1 - 2n_s^2}$ which is the Maxwell-Garnett form of the effective medium equation.

From the refractive indices measured, at 632 nm wavelength, by spectral ellipsometry (see 5.1.4) we can calculate the density ρ of the films deposited at different temperature. In Table 12 the films density is reported in function of the deposition temperature for a density of 3.99 g/cm^3 and a refractive index of 1.76 (at 632 nm) of bulk crystalline alumina.

Deposition temperature T_s (°C)	Refractive index n (@ 632 nm)	Void ratio (1-p)	Packing density p (%)	Density ρ (g/cm^3)
212	1.630	0.17	83	3.31
242	1.631	0.17	83	3.32
264	1.626	0.18	82	3.29
285	1.574	0.24	76	3.01
304	1.550	0.28	72	2.88
407	1.440	0.42	58	2.29
431	1.397	0.48	52	2.06
436	1.404	0.47	53	2.10
493	1.320	0.59	41	1.65

Table 12 Density of alumina thin films deposited by HV-CVD at different substrate temperatures.

In the literature the density of amorphous alumina varies between 2 and 3.6 g/cm^3 [115-117]. Here the values are in the same range with the difference that lower density can be achieved. The top view SEM images presented in Table 13 as well as Picture 17 and Picture 18 confirm that the surface structure varies with the deposition temperature and that the porosity decreases at lower temperature; indeed smaller grains with smaller space in between appear at low substrate temperature.

Temperature (°C)	Packing density (%)	Density (g/cm^3)	SEM image
431	63	2.51	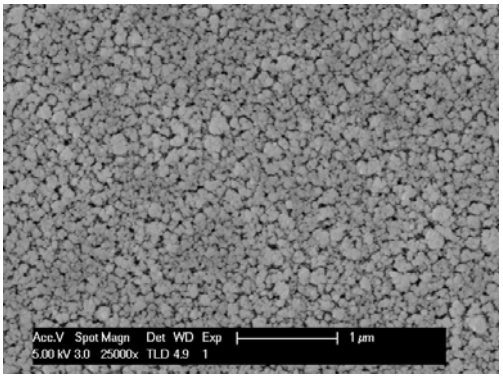
407	71	2.83	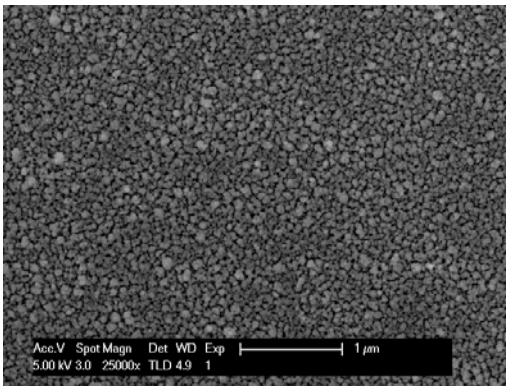
212	86	3.43	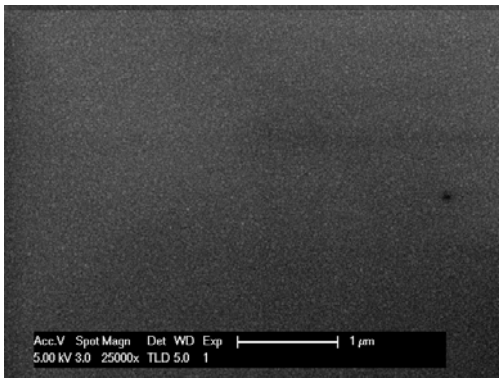

Table 13 SEM images for different density of alumina thin films deposited at different temperatures.

From the SEM images we have estimated the packing density by simple image processing. First, the images have been normalized to the same contrast and brightness and then a binary threshold is applied. From the binary image, the ratio of black pixels (void) on white pixels (material) is calculated and represents the packing density. Finally the density is estimated from the packing density according to the density of bulk crystalline alumina.
This second method gives slightly higher value of density but in the same order of magnitude.
The error on both methods is high and these density values can only be considered as approximation. But these values can highlight interesting behavior of growth as explained below.

In the chemical limited regime (T_s < 325 °C) the density is more or less constant around 3.3 g/cm^3 and then in the mass transport limited regime the density decreases with increasing temperature. In the mass transport limited regime a molecule impinging on the substrate surface is directly decomposed and integrated in the film, consequently the organization in the film is weaker compared to the chemical reaction limited regime where more molecule as needed are present on the surface of the substrate and can find the appropriate spot before decomposition.

The grain boundaries, voids, disorders effects regions, inhomogeneities of the microstructure, roughness and defects can significantly affect the optical properties of thin films [118]. In particular, the refractive index varies according to the porosity [119]. Thereby porosity is a key parameter for waveguide applications [120], influencing transmission properties and that can increase the photoluminescence quenching [121]. Porosity can also enhance light scattering in thin films, this phenomena is useful in solar cell applications where voids increase scattering and light capture [122, 123].
However scattering contributes to the attenuation of light in transmission waveguides, thus scattering must be as small as possible to guarantee a good propagation of the optical signal.

We distinguish three scattering processes one without and two with energetic exchange with matter [29]: (1) Rayleigh & Mie, (2) Raman and (3) Brillouin. Raman scattering deals with the alteration of photon frequency by an exchange of energy with rotational or vibrational mode of a molecule, while Brillouin scattering is similar to Raman scattering except that the exchange of energy takes place with acoustic modes of the material.

Here, we discuss in detail Rayleigh and Mie scattering which are processes that can appear in alumina waveguides due to the microstructure of the films.
Rayleigh scattering causes an incident photon to change direction. The scattered photon has the same energy as the incident photon; this is an elastic process conserving the energy. Rayleigh scattering occurs when the particles sizes are much smaller than λ the wavelength of light. The scattered intensity is proportional to $1/\lambda^4$. So, in the telecom wavelength at 1.55 µm, Rayleigh scattering is limited. For higher porosity, Mie scattering can take place. This scattering does not depend strongly on the wavelength of the illumination and is present for particles larger than λ /10.

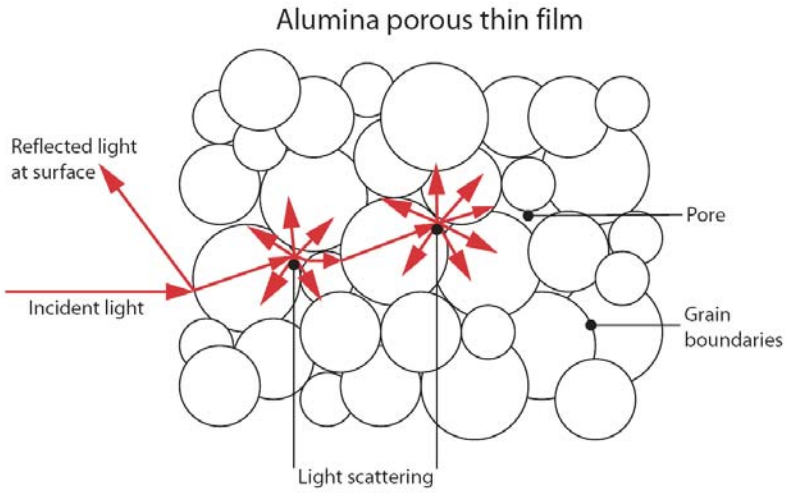

Figure 50 Schematic illustration of light transmission in porous alumina with scattering effect.

Grains boundaries and pores are the main sources of scattering which degrades the direct intensity transmitted light but grain boundary reflection and refraction can also influence the direct transmission. The pores scatter the light very effectively because of the high difference in the refractive index of the material and the void pores.
For the alumina thin films deposited by HV-CVD in this work the particle sizes vary from 20 to 120 nm. We are just below Mie scattering limit for an illumination wavelength of 1.55 µm and at this wavelength Rayleigh scattering is limited. But residual porosity can have pronounced effect on the transparency.
In brief, low porosity and small grain size help to avoid Rayleigh and Mie scattering and are favorable for light transmission in waveguide applications [124].

We also observed that the surface structure is temperature dependent. Indeed, increasing the temperature induces higher roughness and larger grain size, as shown

on Graph 34. The roughness is measured by AFM (see Figure 51 and Figure 52) whereas the grain size is estimated from the top view SEM pictures (see Picture 17 and Picture 18).

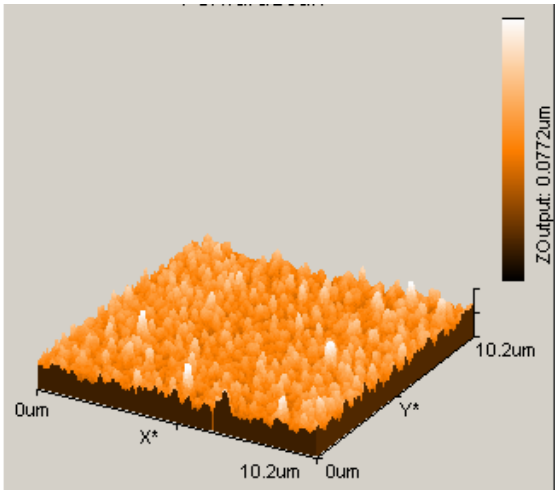

Figure 51 AFM image of alumina thin deposited at 264 °C, R_a = 5.57 nm.

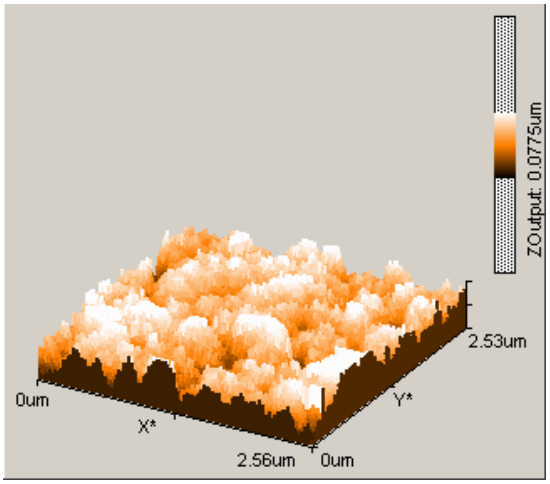

Figure 52 AFM image of alumina thin deposited at 493 °C, R_a = 15 nm.

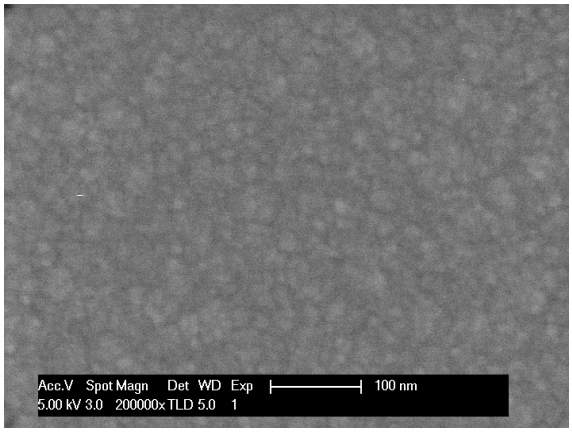

Picture 17 SEM image of alumina deposited at 264 °C, grain size = ~ 10 nm.

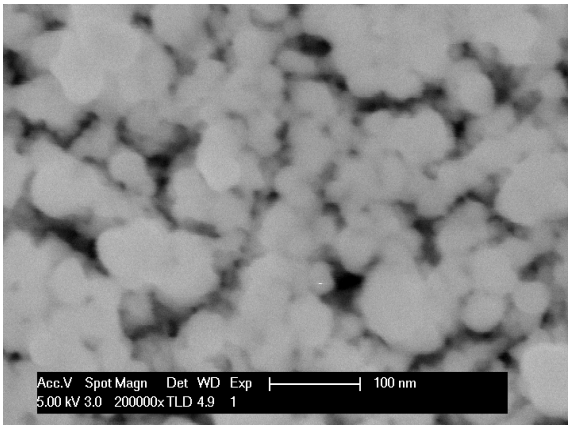

Picture 18 SEM image of alumina deposited at 493 °C, grain size = ~ 80 nm.

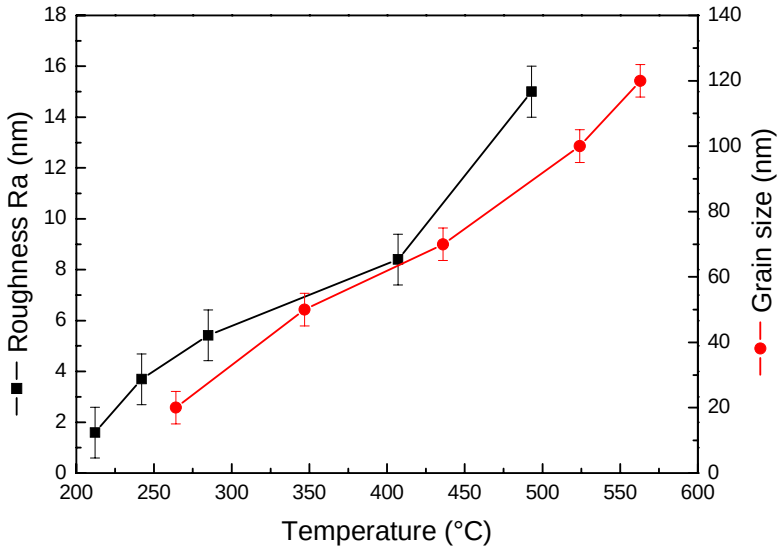

Graph 34 Temperature dependence of grain size and roughness of alumina thin films.

We have seen that the temperature influences the surface topography, now we will study the effect on the growth by checking the structure difference along the growth direction.

The first observation, in the as cleaved side view SEM images, is that at low temperature the film is oriented on the growth direction (Picture 19), while at high temperature (> 450 °C) no preferential orientation is present, as illustrated on Picture 20. The same behavior appears on TEM images; see Picture 21 and Picture 22 of samples prepared by carbon coating and Focused Ion Beam (FIB) cut. The film deposited at 325 °C shows an orientation along the growth direction while on the films deposited at 525 °C only assembly of more spherical structure can be observed.

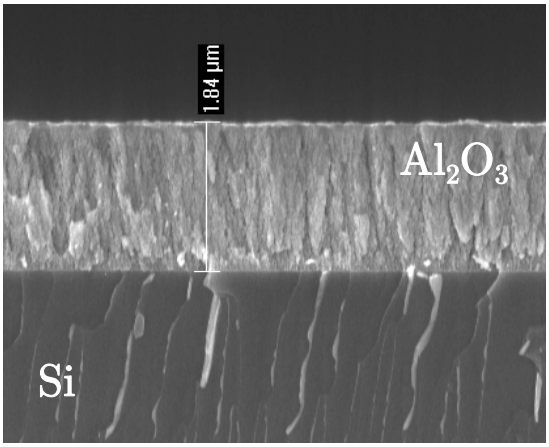

Picture 19 SEM side view of alumina thin film deposited at 347 °C, as cleaved.

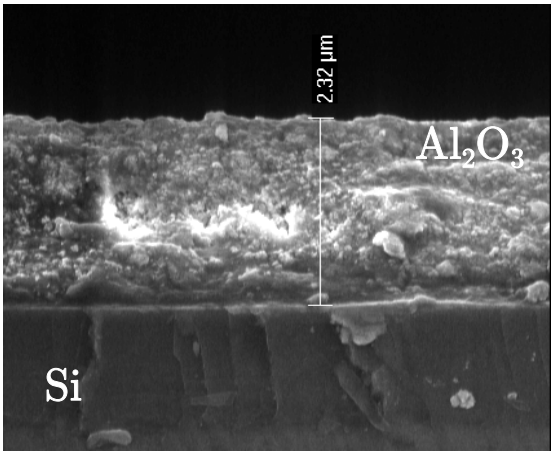

Picture 20 SEM side view of alumina thin film deposited at 563 °C, as cleaved.

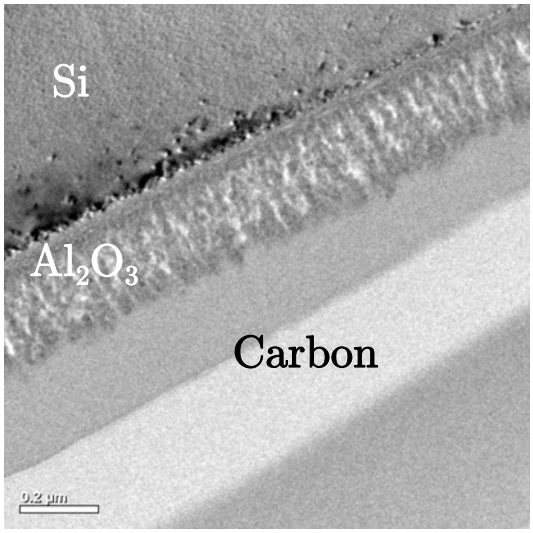

Picture 21 TEM image of alumina thin film deposited at 325 °C.

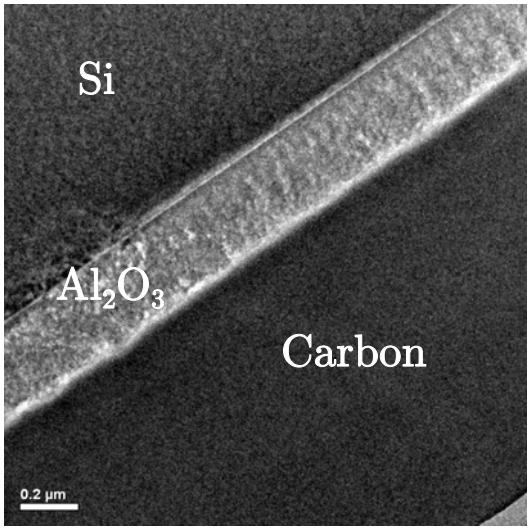

Picture 22 TEM image of alumina thin film deposited at 524 °C.

The growth behavior can be predicted by the zone model developed by Thornton for films deposited by PVD [125]. But based on the work of Movchan et al. [126] and Sanders et al. [127] this model can be extended to the case of oxide films deposited by CVD. The zone model can predict coating microstructure as a function of primary deposition variables such as substrate temperature. This model concludes that the coatings can be represented as a function of T/T_m (T = substrate temperature and T_m = melting temperature of the bulk material) in terms of three different zones, each with its own characteristic structure and properties, see Figure 53.

Zone 1 ($T/T_m < 0.3$) consists of tapered poorly defined crystals with domed tops which are separated by voided boundaries. A transition zone, Zone T, consisting of a dense array of poorly defined grains without boundaries can be distinguished between Zone 1 and Zone 2.

Zone 2 ($0.3 < T/T_m < 0.5$) consists of columnar grains separated by distinct, dense, and intercrystalline boundaries which have highly faceted surfaces.
Zone 3 ($0.5 < T/T_m < 1$) consists of equiaxied dense grains.

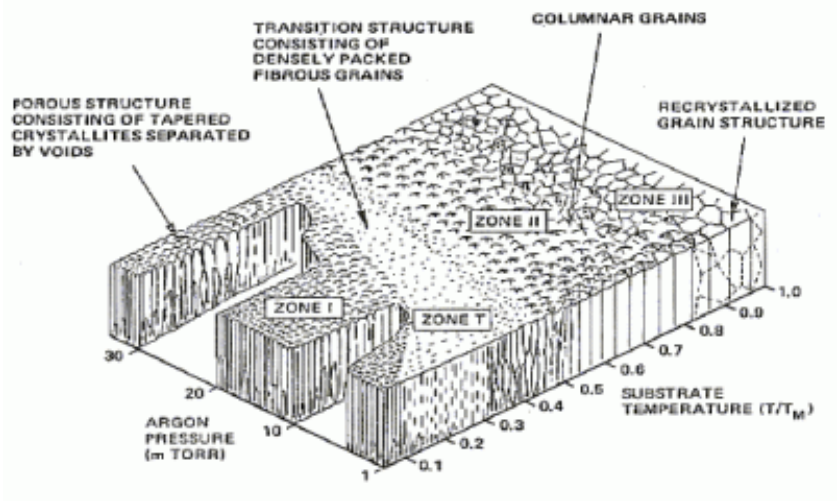

Figure 53 Structural zone models for coating growth [125].

The melting point of alpha alumina is T_m = 2054 °C and the deposition temperature range used in this work is T = 200 to 600 °C; that means that the T/T_m ratio is always lower than 0.3 and thus we are in the Zone 1.

The model of Thornton was primarily developed for Physical Vapor Deposition (PVD) of metal, but different studies show that this model can be adapted to oxide thin films [117, 128].

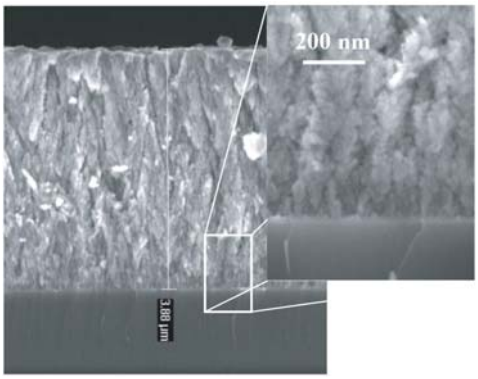

Picture 23 SEM side view of alumina thin film deposited at 430 °C.

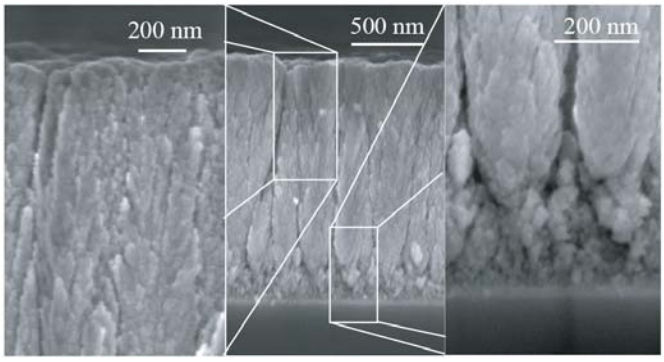

Picture 24 SEM side view of alumina thin film deposited at 400 °C.

The different SEM pictures (19, 23, 24, 25 and 26) of alumina thin films show clearly tapered structure with domed tops separated by voided boundaries; this confirms

that the alumina deposited at 200 to 600 °C under HV-CVD conditions belong to the Zone 1 of Thornton's model eventually the Zone T.

The presence of void also confirms that the density is lower than pure crystalline form of aluminum oxide. As proven in Table 13, the structure diameter increases with T/T_m and indicates that the surface diffusion is limited during the growth process.

We also observe that near the substrate or at the beginning of the growth, the structure is composed of smaller grains. The nucleation on the substrate starts on small grains and then the film grows on top of theses nucleation site in a tree structure following the growth direction.

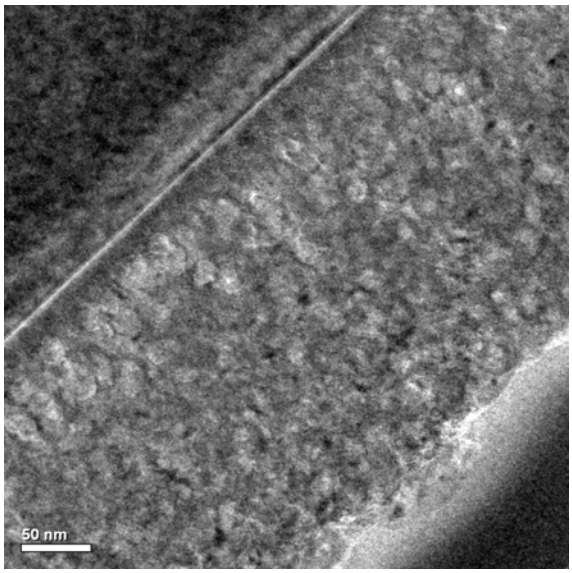

Picture 25 Alumina thin film for $T/T_m \approx 0.3$.

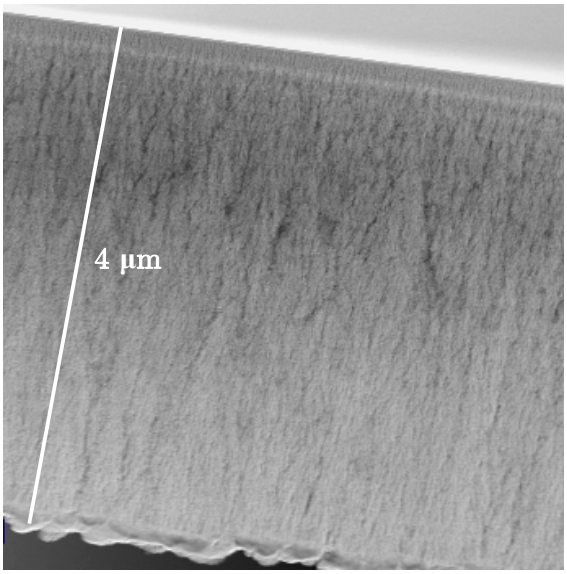

Picture 26 Alumina thin film for $T/T_m \approx 0.15$.

The dependence of the column diameter on the thin film thickness can be explained by the fact that the columns consist of, for example, fibrous subunits which bunch together more and more as the films thickness increases [129].

The alumina thin films deposited in high vacuum by chemical vapor deposition process from 200 to 600 °C have very good adhesion on silicon substrate. As already shown on the SEM images the interface between film and substrate is well defined. In the following TEM images (Picture 27, 28 and 29), we clearly see that the interface is perfect. In Picture 29 the substrate has been heated at 650 °C for one hour before the deposition in presence of 0.4 sccm of oxygen and the native silicon oxide is present in the TEM image and again the interface with the alumina thin films is perfect.

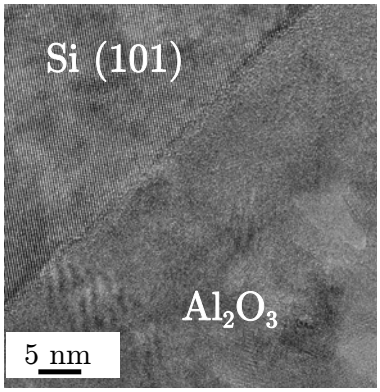

Picture 27 TEM image of Si – Al_2O_3 interface.

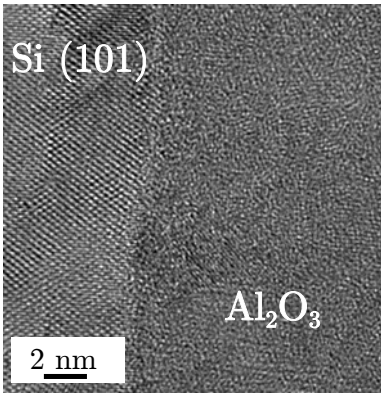

Picture 28 TEM image of Si – Al_2O_3 interface.

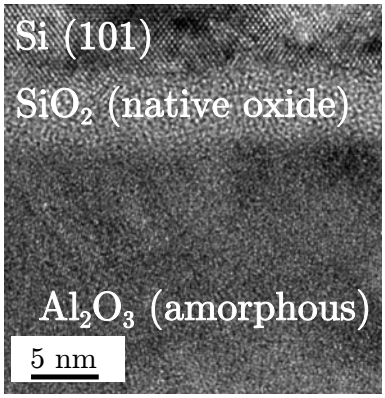

Picture 29 TEM image of SiO_2 – Al_2O_3 interface.

The structure of the deposited alumina films by HV-CVD is amorphous in the temperature range of 250 to 700 ºC. But the density shows variation according the deposition temperature. This is explained by the different growth regimes and the number of molecules present on the substrate surface. The presence of void confirmed by optical measurements and SEM images can induce scattering in the films but this is particularly important for short wavelengths.

Finally, substrate effects have not been observed in the limited range of tests on natural oxidized silicon, 3 µm SiO_2 on silicon, quartz, stainless steel, fused silica and 100 nm silicon nitride on top of silicon.

5.2. Erbium doping

In optical fiber technology, erbium doped fiber amplifiers are widely used in long distance communications systems working at 1.55 µm wavelength. From this concept erbium doped waveguide amplifiers are being developed. The need of optical devices for integrated optics, such as tunable optical amplifiers is in fast expansion. These components should be silicon compatible in order to be incorporated in more complex opto-electronic devices.

To induce amplification, Er is incorporated in the core of a waveguide and is excited with a pumping laser then the transition to the ground state occurs at 1.55 µm. Pumping is achieved by 980 nm laser diodes and, with enough power, leads to population inversion between the first excited state and the ground state. Finally the 1.55 um signal induces stimulated emission resulting in amplification.

To fabricate such devices one needs a host material, compatible with Si technology, transparent to the excitation and signal wavelengths, with high refractive index and able to receive Er atoms. Besides its good optical properties alumina is chosen as

attractive host material for erbium doping because similarity in valence, crystal structure and lattice constants between Er_2O_3 and Al_2O_3.

The erbium concentration needed is in the range of 10^{19} to 10^{20} cm^{-3} (optically active Er) to achieve reasonable gain [130, 131] or in other words a concentration of about 0.26 at% [132]. Erbium doped alumina waveguides have been fabricated in the last ten years mainly by sputtering and ion implantation [85, 133].

We propose here to deposit Er doped Al_2O_3 with our HV-CVD system using the decomposition of ATI and $Er(TMHD)_3$, some details about $Er(TMHD)_3$ are presented in appendix 9.9. We intend to use two independent rings of the effusing source to have a co-flux of precursor reaching the Si substrate homogenously and with the right set of parameters (substrate temperature, pressure) be able to control the erbium doping of alumina.

But first to have a better understanding of the erbium precursor behavior, we tried to deposit pure erbium oxide from the thermal decomposition of $Er(TMHD)_3$ in HV-CVD conditions. The precursor is heated at 145 °C and the deposition duration was one hour, in presence or not of oxygen.

This precursor seems to be difficult to decompose in our system indeed, after many unsuccessful tries in the range of 400 to 700 °C; we obtained only non-stoichiometric very thin films (about 20 nm), see Picture 30 and Picture 31. The decomposition probability of this precursor is low. The EDX analysis show chemical composition close to "ErO4". This is confirmed by XPS, see Graph 35, indeed surface carbon contamination is present but after etching few nanometers of the material, we reach the same ratio between erbium and oxygen: 80 at% O and 20 at% Er.

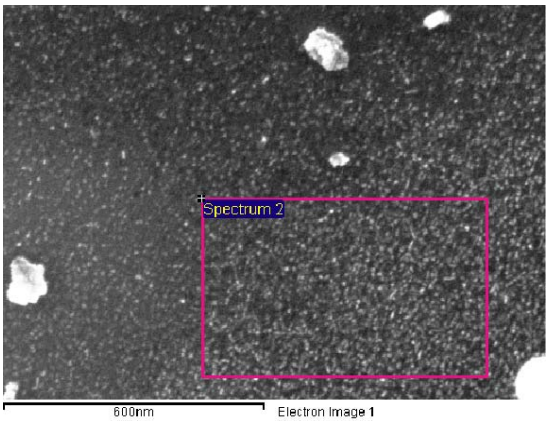

Picture 30 Very thin film made of 89 at% O and 11 at% Er (600 °C, 0.2 sccm O_2).

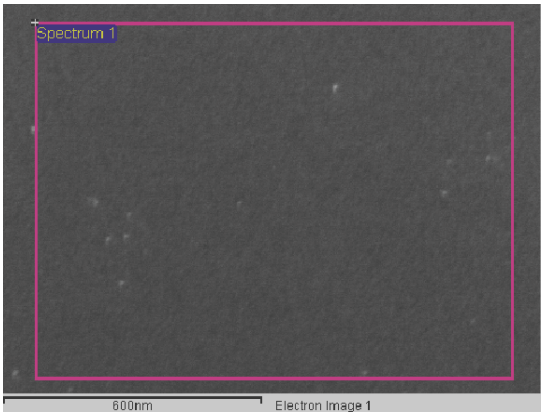

Picture 31 Very thin film made of 79 at% O and 21 at% Er (700 °C, 0.2 sccm O_2).

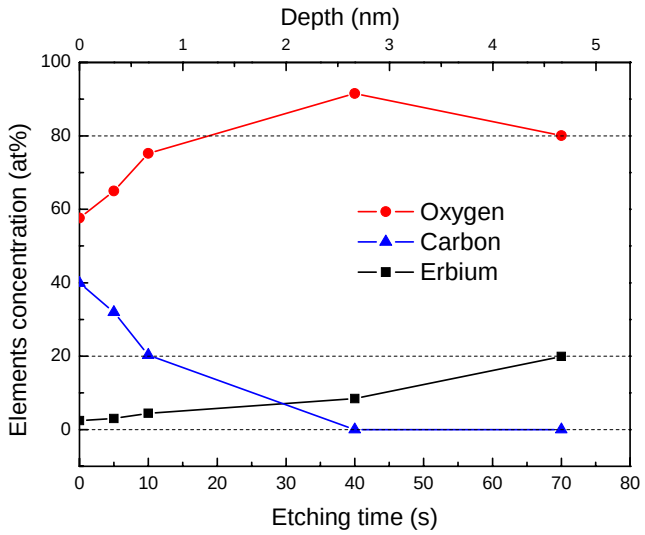

Graph 35 XPS characterization of erbium oxide thin film deposited by HV-CVD.

From these results we co-deposited ATI and $Er(TMHD)_3$ precursors with a substrate temperature of 700 °C and an oxygen flux of 0.2 sccm. Again the film is thin and made of 29 at% O, 57 at% Al and 21 at% Er. The quantity of erbium is clearly too high for optical applications but the most relevant thing is that this co-flux process seems to limit the aluminum oxide growth. Indeed, the presence of the erbium precursor flux limits the growth of alumina. Surface competition between the two precursors can explain this decrease of the growth rate. But at high temperature we enter into the desorption limited regime of alumina deposition (see 5.1.2).

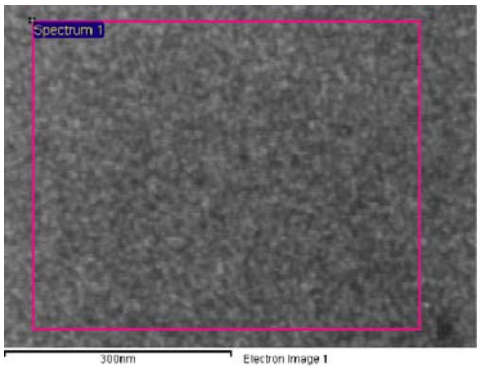

Picture 32 Er doped alumina obtained at 700 °C.

Co-deposit at lower temperature (500 °C) in presence of 0.6 sccm of oxygen for sixty minutes; resulted in 400 nm thick film. EDX measurements show pure alumina but this technique is not sensitive enough to detect small amounts of erbium as needed for doping. So, this film was analyzed by XPS. The results of the XPS depth profile are summarized in Table 14 and plotted in Graph 36.

Etching		Atomic Concentrations (at%)			
Time (s)	Depth (nm)	O	C	Er	Al
0	0	44.90	21.18	0.17	0.17
30	1.33	58.39	0	0.09	41.52
60	2.67	58.95	0	0.06	40.99
90	4	57.93	0	0.06	42.01
120	5.33	58.19	0	0.10	41.71
150	6.67	57.55	0	0.13	42.32
210	9.33	56.15	0	0.10	43.75
270	12	55.97	0	0.12	43.91
450	20	52.57	0	0.16	47.27

Table 14 XPS analysis of Er:Al_2O_3.

Carbon contamination is only observed on the surface but then the material is constituted of pure alumina with 0.06 to 0.17 at% of erbium.
The individual spectra are plotted in Graph 37 to Graph 40.

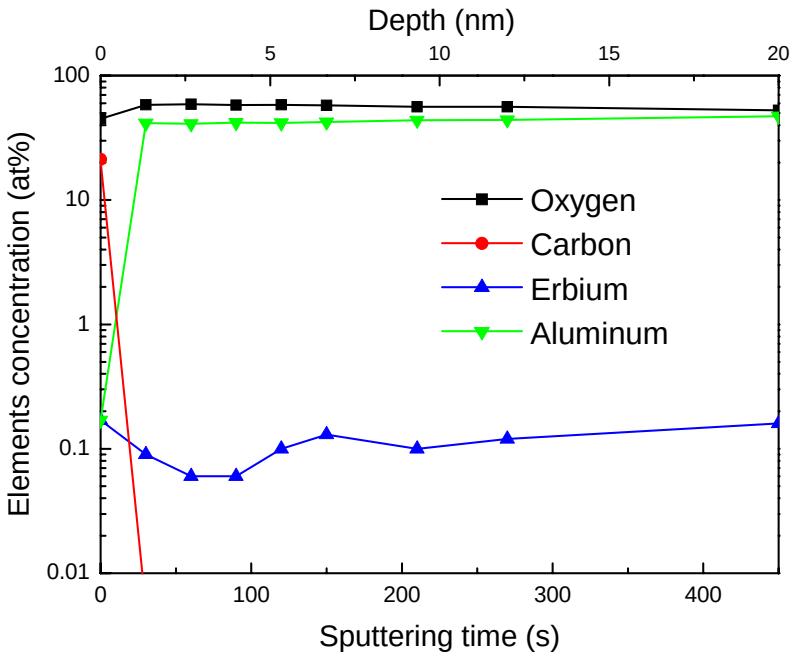

Graph 36 XPS depth profile of erbium doped alumina.

Erbium doped alumina can be deposited by HV-CVD. The parameters window (temperature, pressure, precursor fluxes), inducing good quality Er doped Al_2O_3 thin films, has still to be optimized.

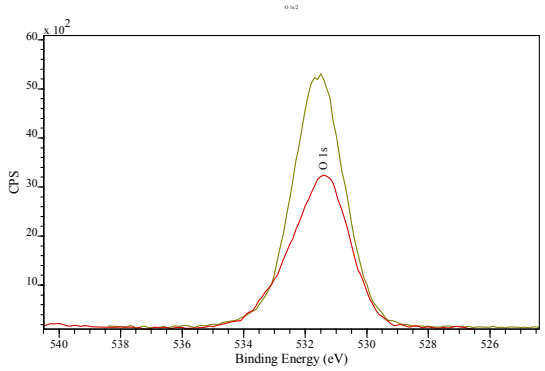

Graph 37 Red curve: before sputtering, green one: sputtering 30 s.

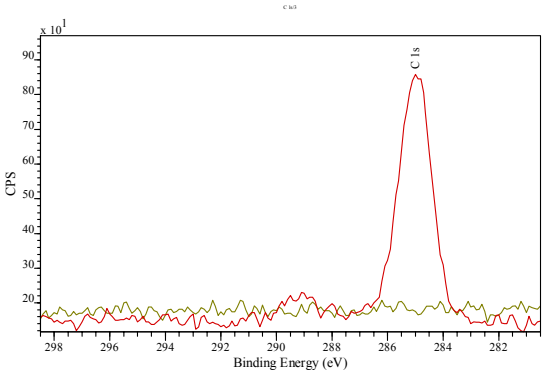

Graph 38 Red curve: before sputtering, green one: sputtering 30 s.

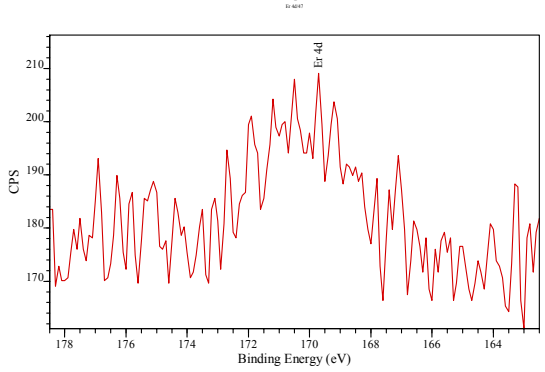

Graph 39 Red curve: sputtering 270 s.

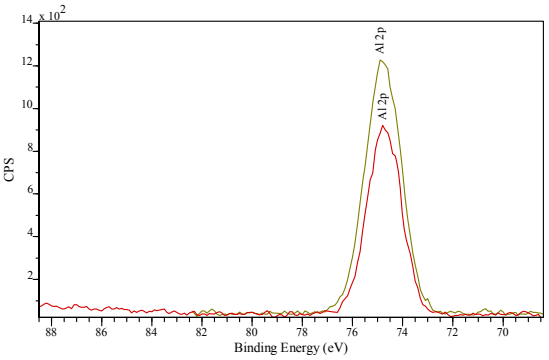

Graph 40 Red curve: before sputtering, green one: sputtering 30 s.

5.3. Summary and conclusion

The growth behavior of HV-CVD follows the two regime model with a chemical reaction limited regime and a precursor desorption limited regime. A minimum activation energy of 33.1 ± 8.2 kJ/mol is measured for thermal deposition. Adding sufficient flow of oxygen reduces this activation energy to 11.4 ± 5.3 kJ/mol. The alumina films are free from carbon contamination but show, for lower temperature deposition, the presence of OH-groups.

Concerning the optical properties of the films, absorption is low above 400 nm wavelength and the refractive index varies from 1.35 to 1.65 (at 632 nm) with decreasing deposition temperature. The layers are amorphous and grainy with a density of 3.3 to 2.0 g/cm^3. Columnar growth is observed from 250 to 450 °C and the adhesion on the substrates is good, as measured by the steam cooking test.

HV-CVD can deposit alumina thin films with different properties especially density and refractive index, this latter can be useful for instance to deposit multilayers of different refractive indices. HV-CVD follows the growth rate behavior as reported in

the litertaure but presents some differences as illustrated with the temperature effect on the density. Usually increasing the temperature densifies the layers in CVD but here in the range of 250 to 700 °C, where amorphous alumina is produced, the temperature influences the density in the opposite way.

Erbium doped alumina is demonstrated with an average erbium concentration of about 0.12 at% and could be a promising laser material in the telecom windows for integrated optics.

Chapter 6 Beam assisted HV-CVD of alumina

6.1. Laser induced HV-CVD

In this chapter, the interaction between 248 nm wavelength UV light, silicon substrate and aluminum isopropoxide is discussed. The aim is to deposit local structure in the HV-CVD system to create an in-situ manner integrated optical devices. The influence of the excimer laser on the deposits will be studied as well as the properties of the deposited material.

When the silicon substrate at room temperature is exposed to a molecular flux of ATI and is locally illuminated with the excimer laser light, a local deposit of alumina is obtained. Thickness of the deposits varies as a function of the fluence, the frequency of the laser and the exposition time.

A systematic study of deposition at different smaller laser fluences and variations of frequency was carried out in order to obtain good quality alumina deposit. The saturation of the thickness with increasing frequency at constant fluence is observed as illustrated in Graph 41. Currently, it is explained by the decreasing temperature during deposition as the film grows thicker. This hypothesis would be based on the transparency of the alumina at 248 nm wavelength. The termal deposits were absorbing at this wavelength, but due to the limited size of the excimer laser induced deposits the optical properties could not be determined. Taking transparent alumina as film, the laser light would be absorbed in the substrate. The alumina films could act as thermal insulation causing the temperature on the surface to be lower than in the case of pure silicon substrate. In section 3.3.6, the decrease of the temperature at the surface of different thicknesses of alumina layer is simulated.

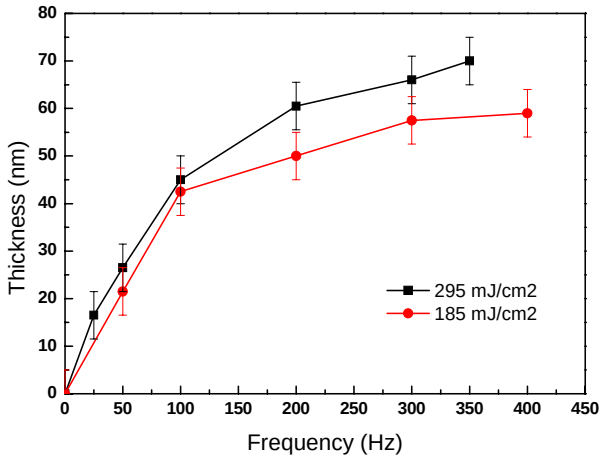

Graph 41 Influence of the frequency on the thickness of laser induced alumina deposited at 295 and 185 mJ/cm^2.

The temporal behavior of the laser induced deposition has not been studied, therefore the interpretation of these results are purely hypothetical.

Saturation effects are reported in the literature for laser assisted deposition of GaAs by 514.5 nm argon laser [134] or 308 nm excimer laser [135] irradiation and for deposition of aluminum by 193 nm excimer laser [136]. Sugiura et al. observed that for 514.5 nm irradiation the growth rate tends to saturate with increasing the power of light. The growth rate saturation is explained by the fact that impinging precursor is fully decomposed and mass transport limited regime appears. Farrell et al. studied the influence of the laser (308 nm) repetition rate and the growth rate saturates with increasing the frequency. The explanation is that the variation in growth rate with the repetition rate is primarily related to the kinetics of adsorbate formation and dissociation. Another hypothesis is very briefly mentioned that involves the laser pulses to mobilize molecules to free sites and can induce site blocking. Tokumitsu et al. observed saturation effect as well for the deposition of aluminum and suggests that the kinetic mechanisms play an important role in photodecomposition.

The saturation effect has been reported by Fukushima et al. in the case of decomposition of aluminum isopropoxide by 185 nm irradiation [17].

In our case, the thickness of the films stops, which is difficult to explain.
Our explanation would be a re-ablation effect. Indeed, the maximum thickness reached is about 70 nm close to $\lambda/2 \cdot n$ (assuming $n=1.6$, $\lambda=248$ nm). The ablation would be most efficient at that thickness due to the maximum intensity of light reached in that point coming from the incident beam interfering constructively with the reflected light on the silicon substrate. As demonstrated in the next paragraph, some of the laser induced deposits are made of aluminum, oxygen and carbon. This carbon contamination increases locally the temperature due to its strong absorption and can promote the ablation effect.

Carbon contamination at higher fluence or at higher frequency is measured by EDX, see Graph 42. It probably comes from stronger ligand fragmentation and fragment incorporation under these conditions.

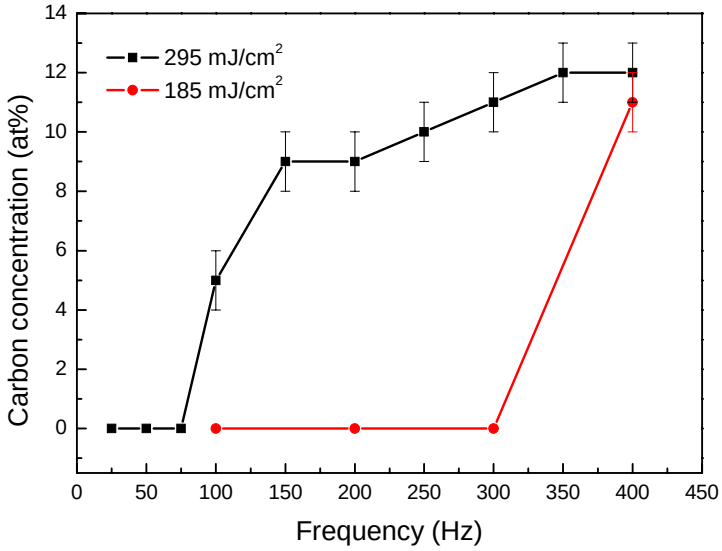

Graph 42 Carbon contamination in alumina laser assisted deposits at 2 fluences: 185 and 295 mJ/cm^2.

By increasing the fluence for a given repetition rate and a constant illumination time, we can increase the temperature where the decomposition of the precursor takes place. We observe a laser induced deposition threshold near 160 mJ/cm^2; after that the films growth follows the fluence as presented in Graph 43.

Considering that the calculated temperatures are a good representation of the substrate temperature heated by laser, we can state that the laser induced deposition threshold lies close to the thermal decomposition temperature at around 220 ºC; this means that the substrate must be at least heated to that temperature to initiate the deposition of alumina. Then it is difficult for the laser induced HV-CVD process to delimit clearly different regimes. But increasing the fluence for constant precursor flux, keeps the growth rate increasing, so we are still in a kind of chemical reaction limited regime. In this regime, we can calculate an activation energy of 5.2 ± 0.4 kJ/mol, see Graph 44. This energy is clearly lower than the 33.1 ± 8.2 kJ/mol measured for the thermal process and is in adequacy with the value (6.3 kJ/mol) reported in the literature by Saraie et al. [63] for ATI decomposition by UV lamp in LPCVD conditions.
The lower activation energy measured indicates that the laser induced process is not completely a thermal process but is at least partially photolytic.

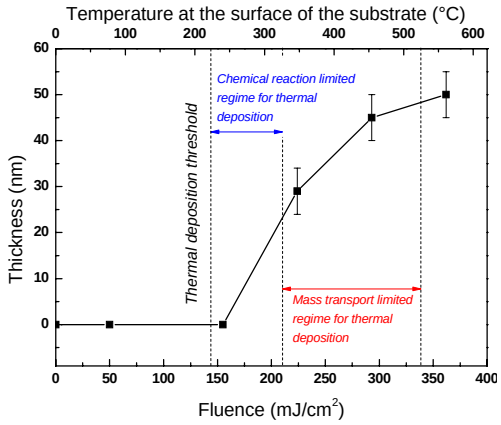

Graph 43 Influence of the fluence on the tickness of alumina laser induced deposition for a repetition rate of 100 Hz.

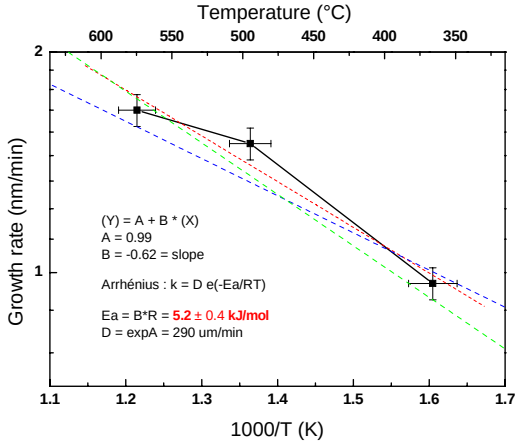

Graph 44 Arrhenius plot of the laser induced process of ATI decomposition in high vacuum.

Both pyrolitic (thermal) and photolytic ways of precursor decomposition are considered. Combination of both effects is surely also possible. According to simulation temperature, rise due to laser pulse illumination is considerable and temperatures up to 300 °C for a fluence of 200 mJ/cm^2 are achieved at the wafer surface. The effect of increasing carbon contamination at higher laser average power suggests as well that photolytic influence is present. Thermal effect of increased irradiation power is expected to cause the opposite effect.

The variation of the different parameters (fluence, repetition rate and time) to increase the total dose gives the same result on the deposited thickness, as represented in Graph 45. No particular effect is observed on the growth rate in function of the total dose by changing one of the parameters; in consequence the process seems to be dominated by photolytic effects.

Nevertheless, local in situ alumina laser assisted high vacuum chemical vapor deposition is demonstrated. Low repetition rate seems to be favorable to avoid carbon contamination and produce transparent alumina structures.

Thicker laser assisted alumina deposits are presented in the next paragraph. The microstructure is different than for thermal deposition but the deposits show cracks and large size grains.

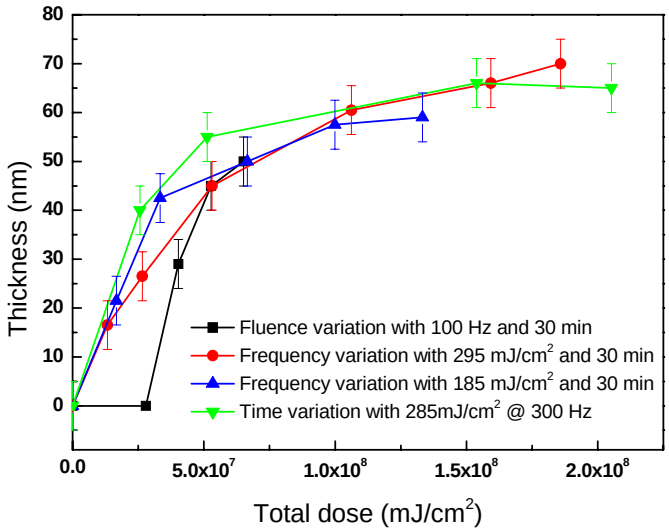

Graph 45 Influence of the laser total dose on the thickness of alumina microstructures deposited by laser assisted HV-CVD.

In Figure 54, a 425 ± 5 nm thick alumina deposit (see Graph 46) on silicon is grown at room temperature by laser induced chemical vapor deposition with 248 nm UV light. The fluence is 362 ± 10 mJ/cm^2, the repetition rate is 100 Hz and the deposition was carried out for 30 min. In these conditions, the total dose is $6.5 \cdot 10^7$ mJ/cm^2 and the real exposure time is $4.5 \cdot 10^{-2}$ s. Thus, the average growth rate is about 14 nm/min but the real growth rate (from the real exposure time) is about 9.5 µm/s or $2.4 \cdot 10^{-3}$ nm/pulse. The precursor flux is $3.1 \cdot 10^{16}$ molecules/s·cm^2 and the chamber pressure during deposition is $5.8 \cdot 10^{-6}$ mbar.

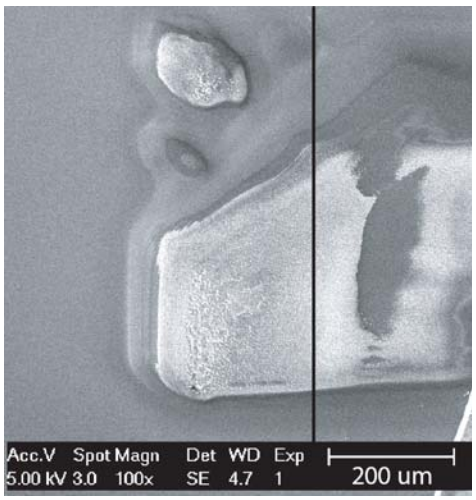

Figure 54 SEM image of laser induced alumina deposited on silicon

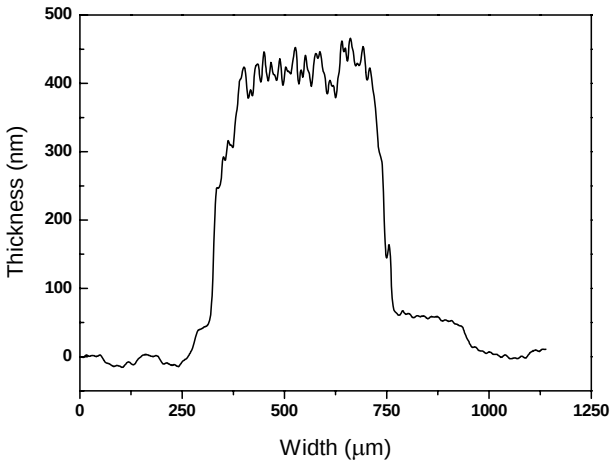

Graph 46 Thickness profile of the laser induced alumina deposit

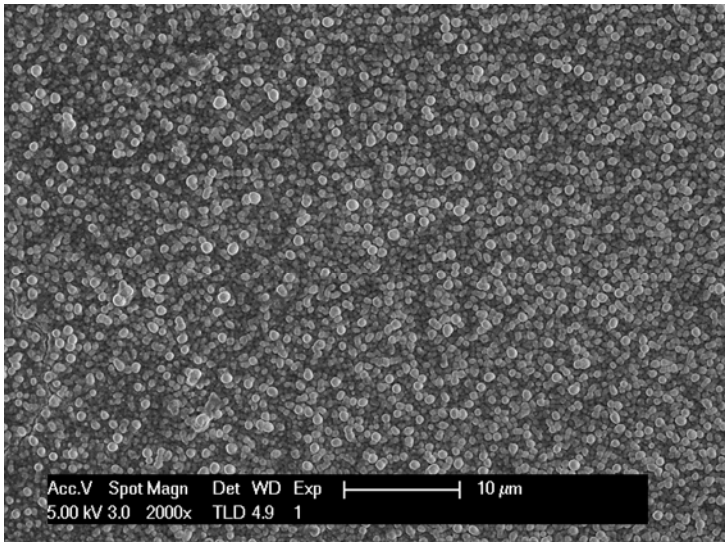

Figure 55 Microstructure of alumina deposited by laser with a fluence of 362 mJ/cm² and a repetition rate of 100 Hz.

The microstrucure of laser induced HV-CVD of alumina is represented in Figure 55 and is grainy and homogenous on the surface of the deposit. The average grain size (500 nm) is larger than purely thermal deposits, where the grains are in the range of 20 to 100 nm with increasing temperature, see 5.1.5. We also observe that the shape of the grains is not the same. They are more round and regular for the deposition under UV light irradiation, as shown in the comparison of laser induced and thermal HV-CVD in Figure 56 and Figure 57, respectively.

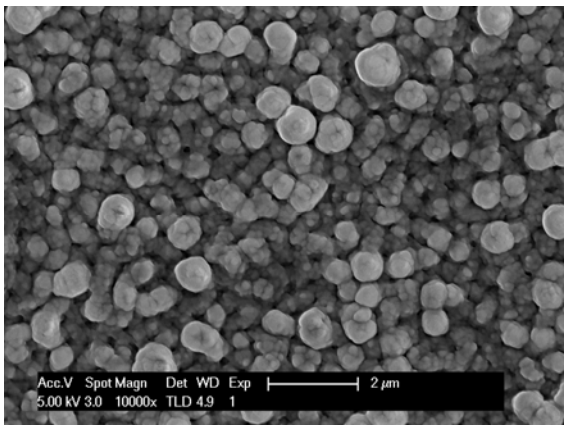

Figure 56 Laser induced HV-CVD of alumina with a fluence of 362 mJ/cm² corresponding to a temperature of 550 °C.

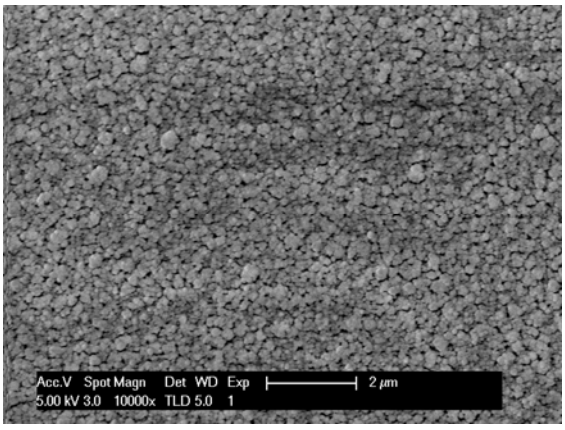

Figure 57 Thermal HV-CVD of alumina at 520°C.

From Figure 54, it is clear that the adhesion of laser induced films is not perfect and some cracks are present. This is probably due to internal stress and side effects of the laser pulses.

6.2. Electron beam assisted HV-CVD

The combination of HV-CVD on wafer scale and electron beam has not been reported before to our knowledge. On the other hand, Focused Electron Beam Induced Deposition (FEBID) is well studied for different materials especially to the fabrication of micro and nano structures for prototyping and microelectronics mask repair [137]. Direct writing with focused electron beam on larger surfaces by the electron beam lithography is described and illustrated in the literature [138].
Here, we propose to study the possibility to use an electron beam to locally deposit nanostructures in HV-CVD conditions, i.e. different from most FEBID systems with controlled flow of precursors and a heatable substrate. The aim is to produce in situ nanostructures on wafers by interaction of electrons and precursor molecules adsorbed on the substrate surface. In this preliminary study, the electron beam has a diameter spot of three millimeters and can not be scanned on the sample surface; but allows to study the effect of electron irradiation on adsorbed molecules and the possibility to deposit aluminum oxide from the decomposition of aluminum isopropoxide. In the literature, alumina deposition by electron beam assisted CVD or FEBID has not been reported.

The example of the electron beam assisted deposition is shown in Figure 58, the substrate was kept at room temperature and irradiated with an electron beam of 3.7 kV and 0.45 mA for 45 min, when exposed to a precursor flow of $2.3 \cdot 10^{16}$ molecules/$cm^2 \cdot s$; thus a deposit of 3 mm diameter and 135 nm thick is achieved.
The electron beam irradiation can also be combined with thermal deposition see Figure 59; in this way the deposit is locally thicker.

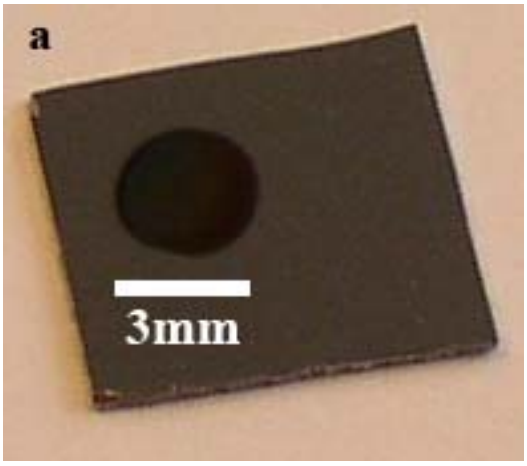

Figure 58 Local alumina deposited by electron beam (3.7 kV and 0.45 mA) on Si at room temperature.

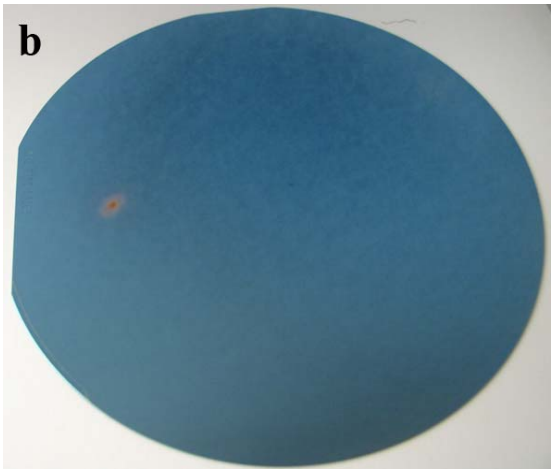

Figure 59 Local increase of the alumina growth rate by electron beam assisted HV-CVD with a subsrate temperature of 350 °C

The grain size of the structure of the electron deposited film is quite small (10 nm to 20 nm), see Figure 60. This observation could be explained by the higher film nucleation density due to electron bombardment. However, such small grain size has also been observed during the thermal growth under certain conditions, see 5.1.5. Currently, it is believed that thermal effect (temperature increase of the substrate surface) of the electron beam irradiation plays an important role.

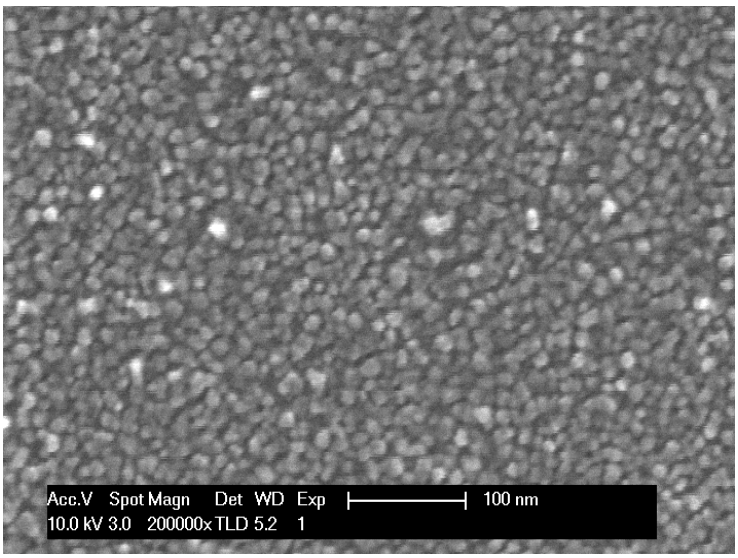

Figure 60 SEM image of the microstructure of assisted electron beam HV-CVD of alumina on Si.

The thickness of the deposits as a function of beam current and acceleration voltage is presented in Graph 47. At constant voltage the deposition rate increases with higher current. However, as soon as acceleration voltage is modified focusing of the beam changes and beam current density on the substrate is strongly influenced. This

effect has to be compensated in order to compare quantitatively the irradiation effect, which is necessary to determine the main precursor decomposition path: either directly electron induced or thermal.

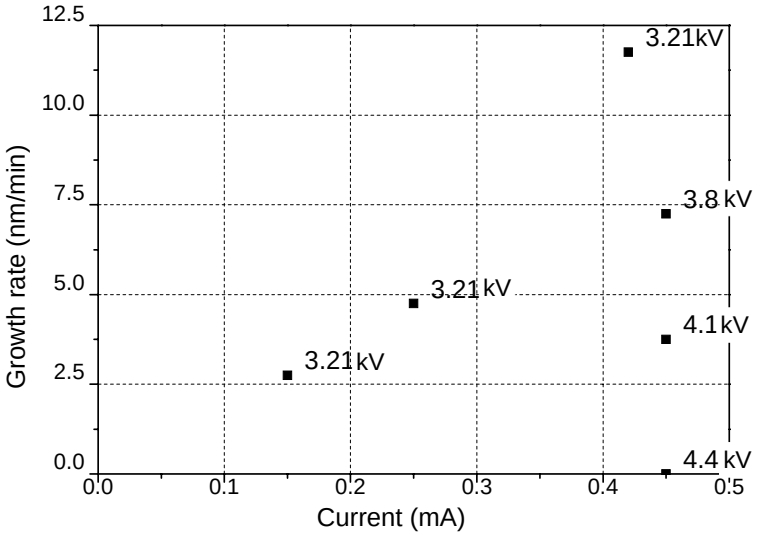

Graph 47 Growth rate versus current for different acceleration voltage of the electron beam in HV-CVD environment.

For a constant current of 0.45 ± 0.02 mA, we can observe in Graph 47, that the growth rate decreases with increasing tension. Electrons with higher energy induce a decrease of the growth rate. Applying the hypothesis of a pure thermal process, we could interpret the result as entering into the desorption rate limited growth regime of HV-CVD, see 1.3.2. Non thermal effect on the deposition could be interpreted by the secondary electron yield that decreases with increasing acceleration voltage, but the growth rate influence seems to be much strong than the secondary electron yield effect would suggest.
The highest growth rate achieved is about 10 nm/min, which is of the same order of magnitude as for thermal deposition of alumina with Al-isopropoxide.

Carbon contamination was measured by EDX and Raman spectroscopy in all the electron beam assisted high vacuum chemical vapor deposition samples investigated.
EDX detects 35 to 45 at% of carbon in the deposits for an average Al/O ratio of 0.45, smaller than the theoretical ratio (0.66) of Al_2O_3.
Raman measurements show typical peaks (see Graph 48) originating from graphite at 1357 cm^{-1} and 1570 cm^{-1} [139, 140].
In order to remove the carbon during the electron beam assisted process, we add 0.4 sccm of N_2O to burn the carbon excess. We see in Graph 48 that, for electron beam

conditions of 3.6 kV and 0.43 mA, the presence of reactive gas helps to reduce the carbon incorporation in the film but unfortunately the contamination has not completely disappeared. Increasing the N_2O flux would help to remove the carbon. Electron beam seems to be efficient to decompose nitrous oxide in active species able to remove the carbon excess. In the thermal decomposition study we observed that N_2O has no effect on the deposition from ATI. Here the presence of N_2O has a quantitative effect on the chemical composition and indicates that electron interaction plays a role.

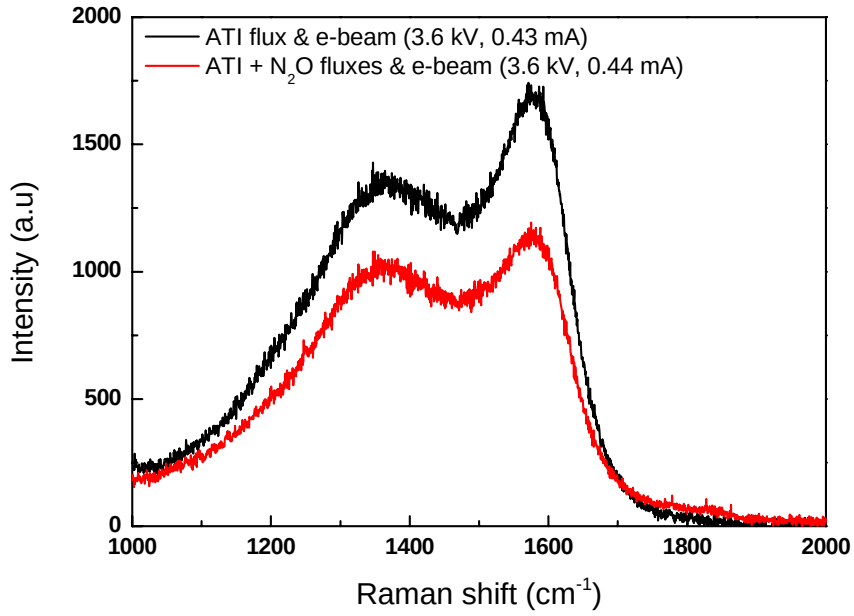

Graph 48 Raman analysis of alumina deposited by electron beam HV-CVD.

6.3. Summary and conclusion

Alumina microstructures can be deposited by laser induced HV-CVD. The measured activation energy of 5.2 ± 0.4 kJ/mol is much smaller than for the pure thermal process. Increasing the repetition rate saturates the growth rate and induces carbon contamination. Thicker deposits with very high growth rate per pulse can be obtained with poor adhesion but composed of plain material and not resulting to the formation of a bubble, as observed in a cross section of the deposit.

The distinction between pyrolytic and photolytic effects of the deposition is difficult. But the structure of the films, the carbon contamination and the same behavior for different doses seem to indicate that photolytic effects are involved.

Concerning the electron beam assisted HV-CVD, the deposition of alumina is demonstrated and a preliminary study of the influence of the acceleration voltage and the current is investigated. Thermal effect of electron irradiation plays a role but other effects are certainly involved. Indeed, the carbon contamination and the surface structure, compared with the thermal deposits, indicate that electrons irradiation influences the deposition by interaction with the molecules and/or the substrate.

Chapter 7 Applications

7.1. Waveguides

7.1.1. Planar waveguide

We demonstrated that the alumina films can perform as planar waveguides, by butt coupling a 670 nm wavelength laser in a 1 cm long and 1.3 µm thick alumina layer deposited on a 3 µm silicon oxide optical buffer layer, see a sketch of the optical setup in Figure 61.

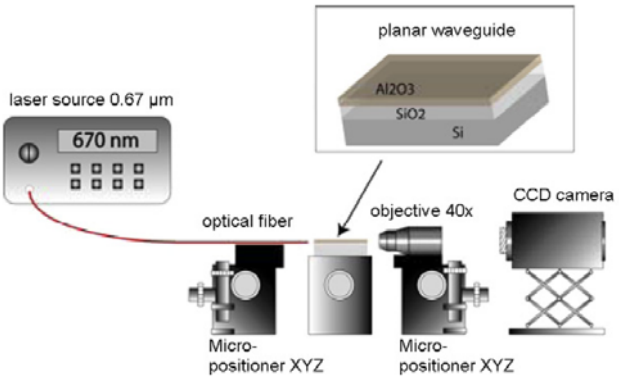

Figure 61 Optical setup for coupling and detection in planar waveguides. (670 nm coupled light).

A SEM image of an asymmetric planar waveguide is represented on Figure 62 with a 1.3 µm thick alumina layer as film.

The guided and transmitted light detected by a CCD camera and the intensity profiles are represented in Figure 63.

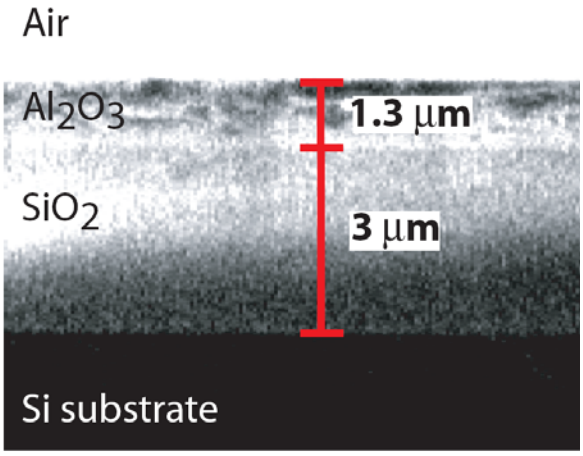

Figure 62 SEM image of a planar waveguide composed of 3 µm SiO_2, 1.3 µm Al_2O_3 and air.

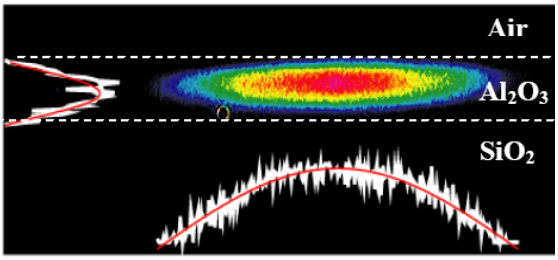

Figure 63 CCD image with intensity distribution of the guided and transmitted light at 670 nm in the planar alumina waveguide. The dotted lines delimiting the substrate and Al_2O_3 layers are guides for the eyes only.

The guiding effect in the vertical direction is clearly demonstrated in the Figure 63, while the beam can spread in the horizontal direction.

7.1.2. Channel waveguide

We produced in this work two types of channel waveguides from four presented in Figure 7: the rib (Figure 64) and the strip (Figure 65).

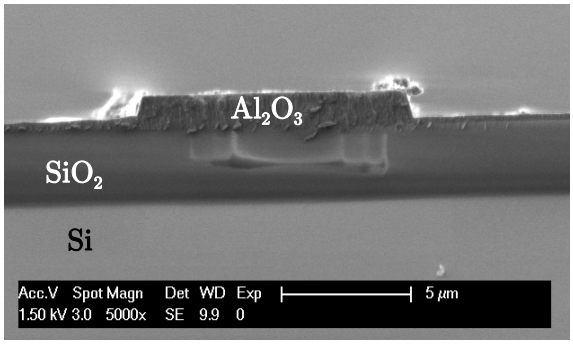

Figure 64 SEM image of a cleaved alumina rib waveguide.

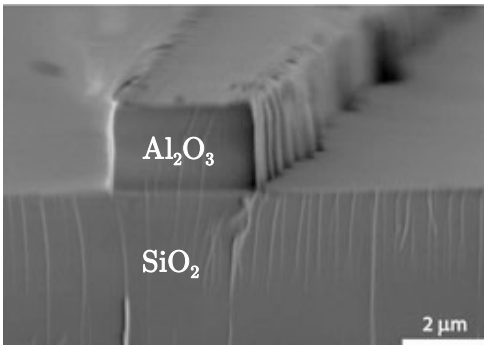

Figure 65 SEM image of a cleaved alumina strip waveguide on silicon dioxide.

Channel waveguides were produced on HV-CVD deposited alumina on SiO_2/Si substrate by standard photolithographic process and Reactive Ion Etching (RIE) on full wafer scale (see Figure 66) in clean room facilities. The different steps of the process are described in appendix 9.10.

In Figure 67 and Figure 68, SEM top view images of channel waveguides are presented as well as a Y junction (left corner in Figure 67). Y junctions, directional couplers and resonators were also produced by this technique in collaboration with the University of Twente (see Figures 69 to 71).

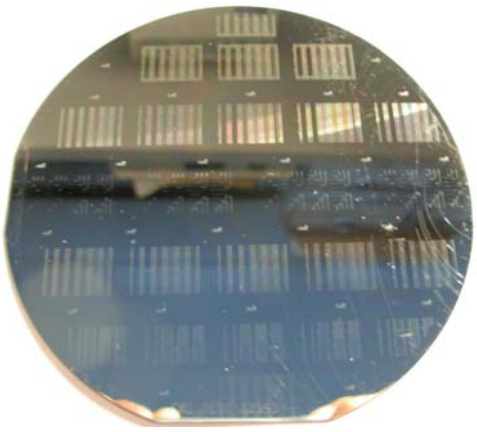

Figure 66 Structured alumina thin films on top of 4 inch silicon wafer.

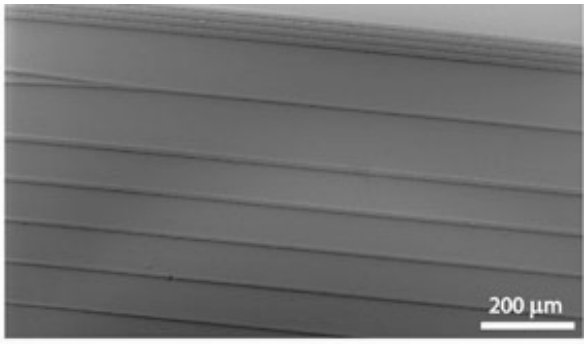

Figure 67 Alumina channel waveguides and a Y junction.

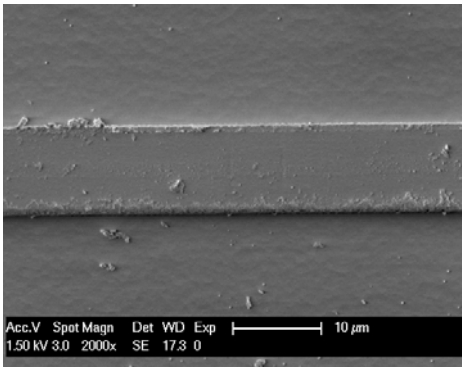

Figure 68 Top view of alumina channel waveguides.

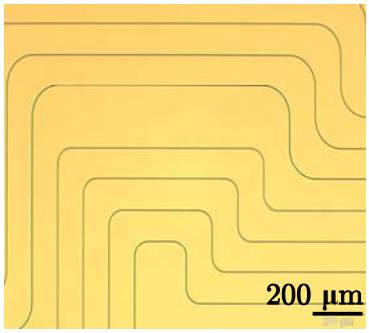

Figure 69 Resonator.

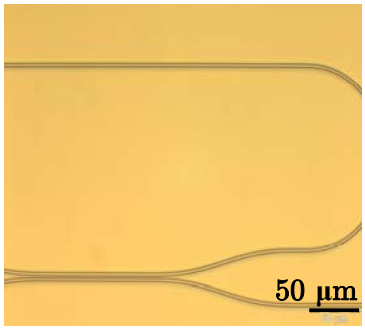

Figure 70 Directional coupler.

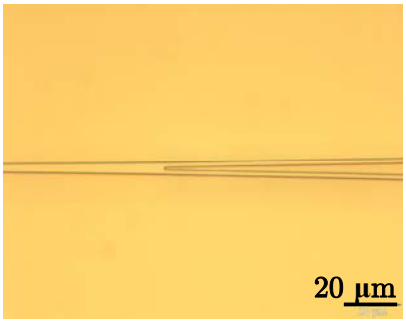

Figure 71 Y junction.

For the Al_2O_3 channel waveguides, the optical characterization is carried out with respect to their mode guiding properties and propagation losses. Before all the measurements, a polishing step is imperative which could effectively reduce the roughness of the coupling facet.

The set-up depicted in Figure 72 records the profiles of guided modes in channel waveguides. The light source, with a wavelength of 670 nm is coupled into a channel waveguide (see Figure 73) via an optical fiber. The intensity profile of the transmitted light is projected onto a CCD camera by an objective of 40× magnification. By adjusting the relative positions of the incoupling optical fiber, the channel waveguide, and the outcoupling objective, the profiles on the intensity distribution of the guided modes can be recorded. Figure 74 shows such profiles for the 670 nm laser diode wavelength and proves that the light is confined inside the strip channel waveguide and that this device performs well as two dimensions waveguide.

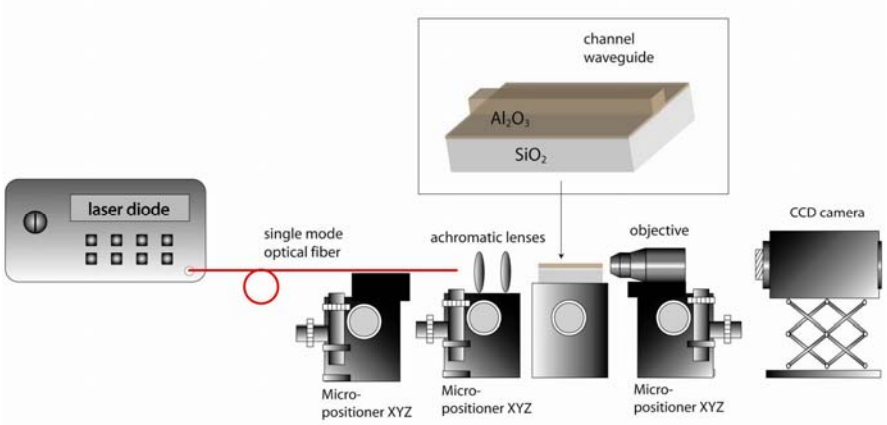

Figure 72 Optical setup for coupling and detection in channel waveguides.

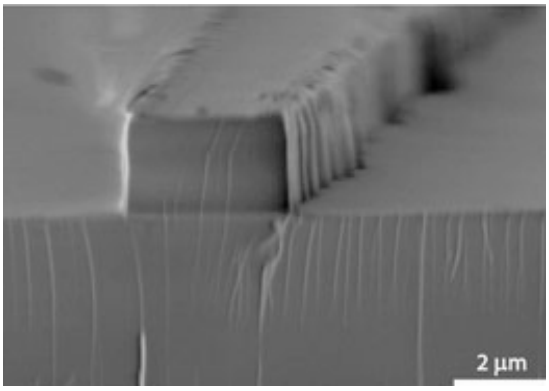

Figure 73 SEM image of an alumina strip channel waveguide.

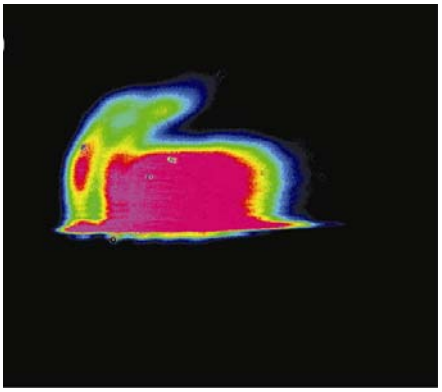

Figure 74 CCD image of the guided and transmitted light in a channel waveguide.

As depicted in the Figure 75a, the set-up for the propagation loss measurement in the Al_2O_3 channel waveguides is based on an HP8504A precision reflectometer operating at a central wavelength of 1.55 µm. The method is so-called optical low coherence reflectometry (OLCR), see 3.4.8. The light source of the HP8504A from the device under test (DUT) port is coupled into a single mode optical fiber (1.55 µm). The length of the optical fiber between the two reference ports A and B of the HP8504A is adjusted that the signal scanning range displayed covers all the distances of reflections in the channel waveguide under investigation. The relative position of the end of the incoupling optical fiber can be adjusted precisely by a micropositioner in X, Y, and Z directions. When a guided mode was observed as the signal of the CCD camera, the reflection spectra were registered from the HP8504A, as shown in Figure 75b. By comparing the optical distance L_{opt}, recorded as the distance between two neighbouring peaks in the reflection spectra, and the physical length of the channel waveguide L_{phy}, measured in an optical microscope, the group index of Al_2O_3 composing the channel waveguides is determined to be $L_{opt}/L_{phy} = 1.7$ at 1.55 µm wavelength.

The propagation loss from guided modes can be measured by comparing the reflectivity values of P_2 and P_3, as indicated in Figure 75b. The round trip loss γ is defined in dB as, $\gamma = P_3 - P_2 = R^2 \exp(-2\alpha L)$, in which R, α and L are respectively the Fresnel loss at the waveguide facets, propagation loss and the physical length of the waveguide. For the channel waveguide with a width of 2.5 µm that we measured, the propagation loss is determined to be 2 dB/cm at 1.55 µm.

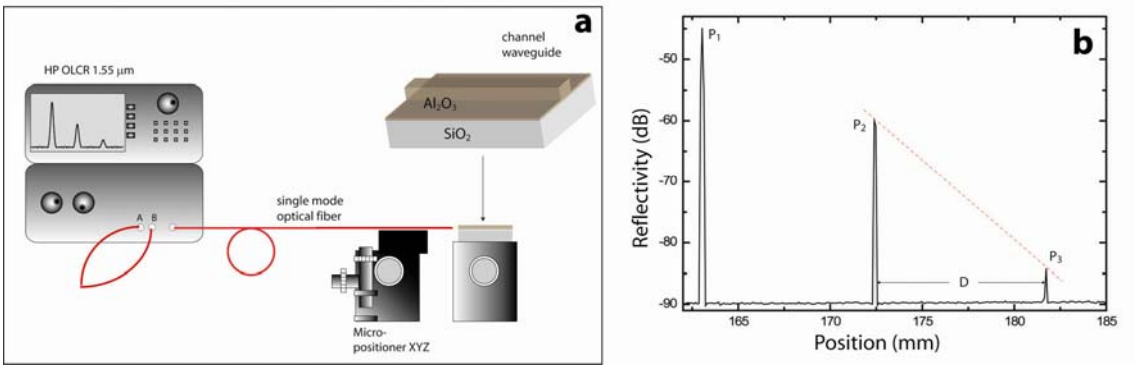

Figure 75 (a) Set-up to measure the propagation loss in the Al_2O_3 channel waveguides. An optical fiber which has a single mode operation at 1.55 µm is used to couple the light source of 1.55 µm from OLCR into the channel waveguides. (b) The returning loss from different facets of the waveguide is registered by H8504A.

7.2. Nano-structuration for integrated optics

We demonstrated the feasibility to deposit laser material such as erbium doped thin films by HV-CVD (see 5.2) and the fabrication of channel waveguides (see 7.1.2) able to guide and transmit light with small losses. In order to achieve integrated optical devices on chip, we need for instance: waveguides, splitters and couplers as presented in 7.1.2; but integrated laser for signal amplification is needed as well.
Er-doped alumina is a good laser material for light amplification [85] but two reflectors are needed to define the resonator cavity.

We propose here two solutions to fabricate integrated reflectors directly in the channel waveguide: (1) Bragg gratings and (2) Photonic crystals.
Theses two devices were produced by Focused Ion Beam (FIB) drilling in collaboration with the University of Twente and consist of the nanostructuration of the waveguide material.

The Bragg grating in Figure 76 has a total length of 24 µm and a pitch distance of 550 nm, it was produced by a FEI nova 600 FIB with an ion current of 93 pA and a total dose of 2138 pC/µm^2.

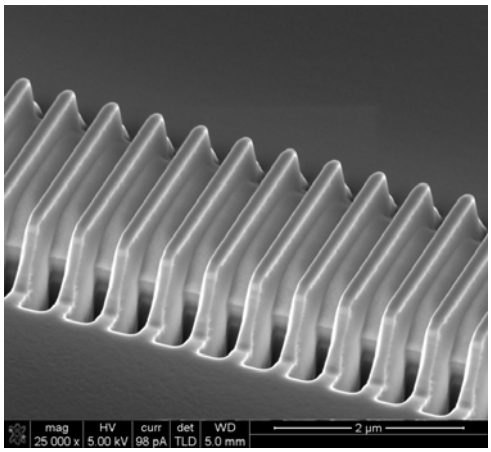

Figure 76 Bragg gratings in an alumina channel waveguide.

Two-dimensional (2D) hexagonal arrangement of nanoholes with depth of h = 1 μm and r(radius)/a(interpore distance) = 0.53 has been chosen to be realized by FIB into channel waveguides. The effect of these 2D nanostructures is to introduce a local reflection within the channel waveguide. Figure 77(a) demonstrates that when the confined light, with a wavelength of 1.5 μm, travels through the microstructured channel waveguide, it will be reflected by rows of nanoholes with the chosen parameters. Given that we would like to have an effective reflection at a wavelength of 1.55 μm, which will be the functional wavelength of the channel waveguide, the set of parameters is chosen to be r = 300 nm, a = 800 nm. The corresponding calculated reflectivity in the Γ-M direction gives a value of about 95%, for the chosen parameters at a wavelength of 1.5 μm, as shown in the Figure 77(b).

Based on the above summarized design considerations, nanohole arrays of 400 - 500 nm in diameter and 800 nm as inter-hole distance have been realized on microstructured Al_2O_3 channel waveguides. The aim to implement those 2D periodic nanostructures into the microstructures lies in introducing an additional high reflection “mirror” within the microchannel waveguides.

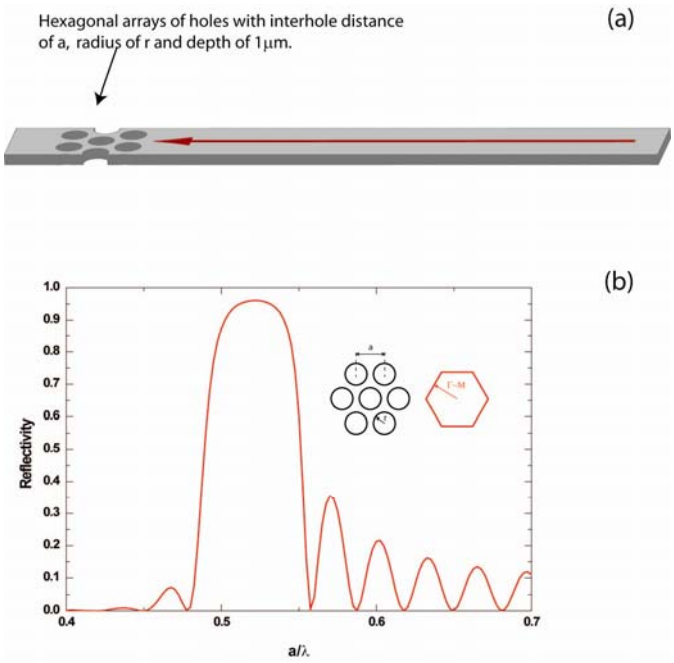

Figure 77 Theoretical calculation and sketch of nanoholes integrated in a microscale channel waveguide. (a) Sketch of 3 rows of nanoholes with a depth of 1 μm integrated close to one end of the microscale channel waveguide. (b) Reflectivity of light in the Γ-M direction in function of the a(interpore distance)/λ(wavelength).

As shown in Figure 78(a), by exploiting FIB-processing, three rows of hexagonally arranged nanoholes with a diameter of 400 nm and inter-hole distance of 800 nm have been successfully realized in a microchannel waveguide in Al_2O_3 with a channel width of 3 μm.

Figure 78(b) gives a zoomed top-view on the nanoholes. It can be seen that they are smooth and have a homogeneous size distribution. The depth of the nanoholes is 1 μm, as confirmed by FIB cross section preparation not show here. This depth is identical to the thickness of the HV-CVD deposited Al_2O_3 film on SiO_2 buffer layer.

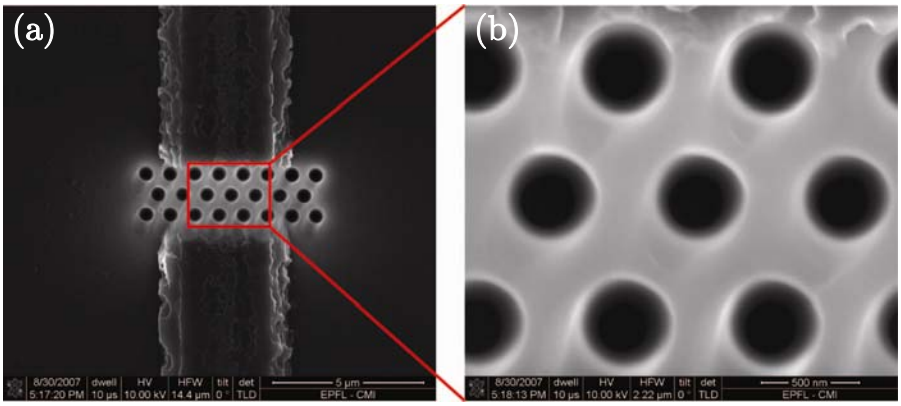

Figure 78 (a) FIB processed nanohole arrays of 400 nm in diameter and 800 nm as inter-pore distance realized on a microstructured Al_2O_3 channel waveguide. (b) Zoomed top-view on the nanoholes.

7.3. Summary and conclusion

HV-CVD alumina deposited on SiO_2 buffer layer can perform as planar waveguide at 670 nm wavelength. Channel waveguides can be prepared by standard photolithographic method; the etching of alumina with RIE proposed by the clean room facilities has been improved during this work. Guiding properties at 670 nm of the channels have been proven and propagation loss < 2 dB/cm at 1.55 μm are measured. Other devices such as Y junction splitter have been fabricated but not further optically investigated.

Nanostructuration of alumina by FIB to produce optical devices such as Bragg gratings or photonic crystals are realized.

In conclusion, optical applications can be realized from the HV-VD deposited alumina. After optical characterization, the optical propertied can be improved by optimizing for instance the film structure and the channel borders. Integrated optical devices on chip could be fabricated based on HV-CVD method which does not represent an advantage as compared to classical CVD methods or even PVD methods such as magnetron sputtering or evaporation. On the other hand, possibilities presented in Chapter 6 would allow the in-situ growth of channel waveguides and with the Er-doping presented in Chapter 5, buried functional system are feasible. The next step is to characterize a waveguide deposited in situ by laser or electron beam assisted CVD, but carbon contamination could induce too strong absorption.

Chapter 8 Conclusions and Outlook

8.1. Conclusion

High Vacuum Chemical Vapor Deposition (HV-CVD) of amorphous aluminum oxide thin films from aluminum isopropoxide decomposition is demonstrated in this work with high thickness uniformity of 95% on 4 inch wafer and competitive growth rate up to 100 nm/min. Erbium doping with $Er(TMHD)_3$ as precursor was achieved. Light induced CVD from 248 nm wavelength short pulse irradiation and electron beam assisted CVD are presented as well. Optical devices such as planar and channel waveguides were produced from the deposited alumina layers showing propagation loss smaller than 2 dB/cm.

All basic components for the in-situ creation of optically active devices compatible with CMOS technology have been presented. Individual steps of this big challenge have been studied in more detail.

A high vacuum reactor has been designed, built and optimized for the deposition of oxide thin films. The main challenge of high vacuum CVD is to obtain comparable control on the growth and the film quality as classical CVD but without moving the substrate and avoiding complex optimization processes, such as reactor design adaptation for CVD processes. In high vacuum CVD processes, the reactants are in molecular beam conditions which allow having a controlled distribution of the precursor molecules. Without substrate movement, an original effusing source has been designed to guarantee high uniform distribution of precursor molecules on the 4 inch substrate surface and in the same time to offer the possibility to perpendicularly irradiate the substrate with an external beam for in situ structuration.

Pure amorphous alumina films have been deposited with competitive growth rate compared to other deposition technique. The measured activation energy is 33.1 ± 8.2 kJ/mol. The aluminum oxide thin films have a refractive index of 1.35 to 1.65 according to the deposition conditions.

Erbium doping was shown up to 20 at% Er content, reasonable growth rates were obtained and deposits of optically active Er concentrations were achieved.

Laser assisted CVD of alumina structures has been achieved with 248 nm light. The measured activation energy is 5.2 ± 0.4 kJ/mol. The resolution is about 80 µm and in specific conditions the growth rate can be as high as 14 nm/min.

Carbon contaminated alumina has been deposited for the first time by electron beam assisted CVD. The growth rate is about 10 nm/min and carbon contamination can be reduced by adding N_2O during the deposition.

The films microstructure of thermal, laser and electron induced deposition has been investigated and compared; grain size, roughness and density are strongly dependent of the deposition conditions.

Planar and channel undoped alumina waveguides were produced by photolithography. Guiding effect at 670 nm and 1.55 μm wavelength has been demonstrated and 2 dB/cm propagation loss has been measured.

8.2. Outlook

Some improvements can be done on the HV-CVD reactor to improve the versatility of the system. First, the heater can be optimized to reach higher substrate temperature. So, crystalline thin films could be deposited. A shutter could be added to have a better control of the thickness and avoid post deposition due to precursor remaining in the prechamber. The effusing source could be also slightly modified to induce composition gradient by mixing different precursors. This technique called combinatorial deposition is really useful to deposit on one substrate different composition of film. This is a powerful tool for the research and development of new material and to optimize properties of material.

CVD and even more HV-CVD processes are strongly influenced by the precursor chemistry and several precursors able to deposit alumina by HV-CVD are available. Aluminum isopropoxide is a good candidate to deposit aluminum oxide thin films but oligomerization and aging effects are critical. Dimethylaluminum isopropoxide, could be a promising precursor for aluminum oxide film growth because its physical and chemical properties lend themselves to industrial applications, e.g., high vapor pressure, non-pyrophoric liquid, relatively simple synthesis and proven success in classical CVD.

High-Vacuum Chemical Vapor Deposition allows depositing thin films with better control but offers also, in a research way, the possibility to investigate in situ the different step of growth. High vacuum gives the possibility to interact with ion, x-ray or electron beams. We can imagine connecting Reflection High Energy Electron Diffraction (RHEED) system to characterize the surface of the growing film or Electron Energy Loss Spectroscopy (EELS) system to measure the presence of carbon for instance or the thickness. A mass spectrometer would help to analyze the formation of by products and help to understand the precursor decomposition or distinguish if a laser induced CVD process is pyrolytic or photolytic.

Some further experiments on laser induced CVD would be interesting to better understand the different involved processes, because mastering the deposition

conditions is needed to realize in situ functional integrated optical devices. Further effort is needed on the design of new devices with smaller features, indeed electron beam assisted CVD which can theoretically reach nanometric resolution by focusing the electron beam.
Technically, a more sophisticated electron gun is needed for a better focusing of the beam and for adding the possibility to scan the beam on the substrate surface.

New material could be deposited in the reactor. Yttrium oxide, as high refractive index transparent material, is an interesting material for optical applications. Lithium niobate, calcium copper titanium oxide (CCTO), hafnium oxide and zinc oxide are all potential interesting materials that could be deposited on wafer scale by HV-CVD.
High Vacuum Chemical Vapor Deposition offers the possibility to deposit mixed oxides or to dope the deposited material with competitive growth rate and good film quality on large surface. The process is compatible with silicon industry and can be adapted to larger wafer size for mass production.
The main advantages of HV-CVD stay the in-situ irradiation possibilities and the rapid optimization process to deposit new materials. The main drawback is the competition of desorption of precursors with decomposition that might limit the process to few final products.

Chapter 9 Appendix

9.1. Technical drawings

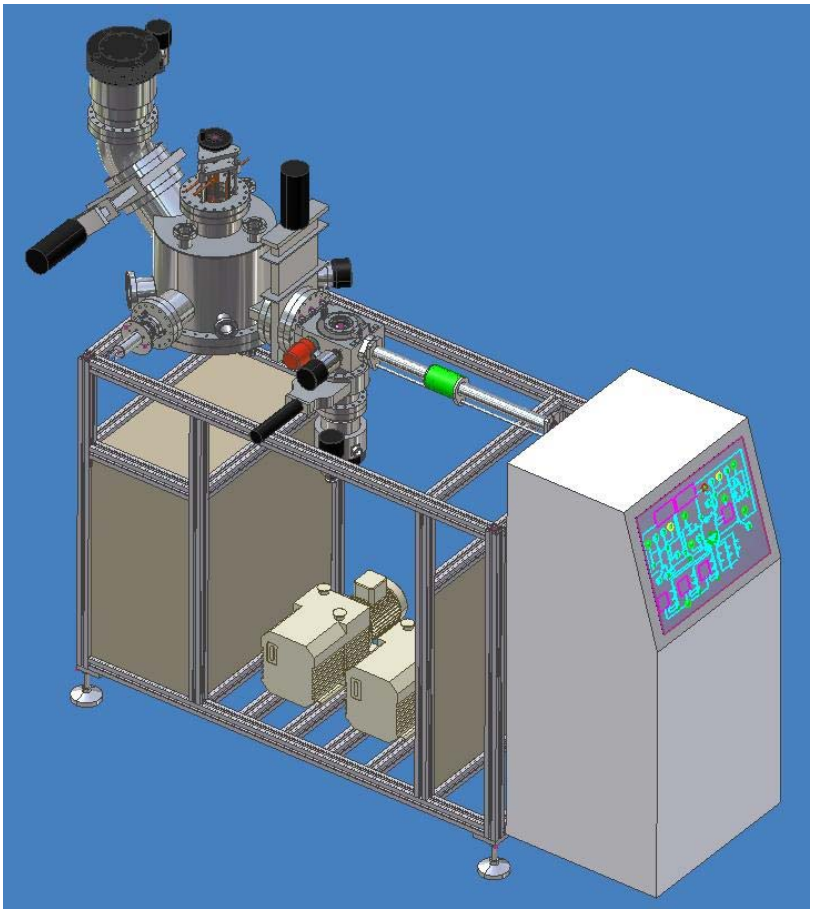

Figure 79 3D overview of the HV-CVD system.

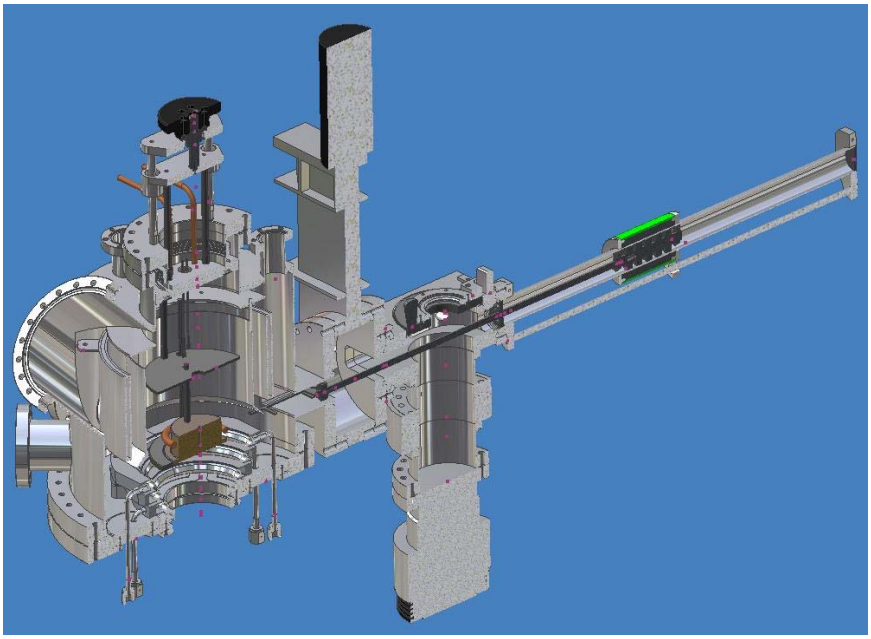

Figure 80 3D view of the inert part of the HV-CVD system.

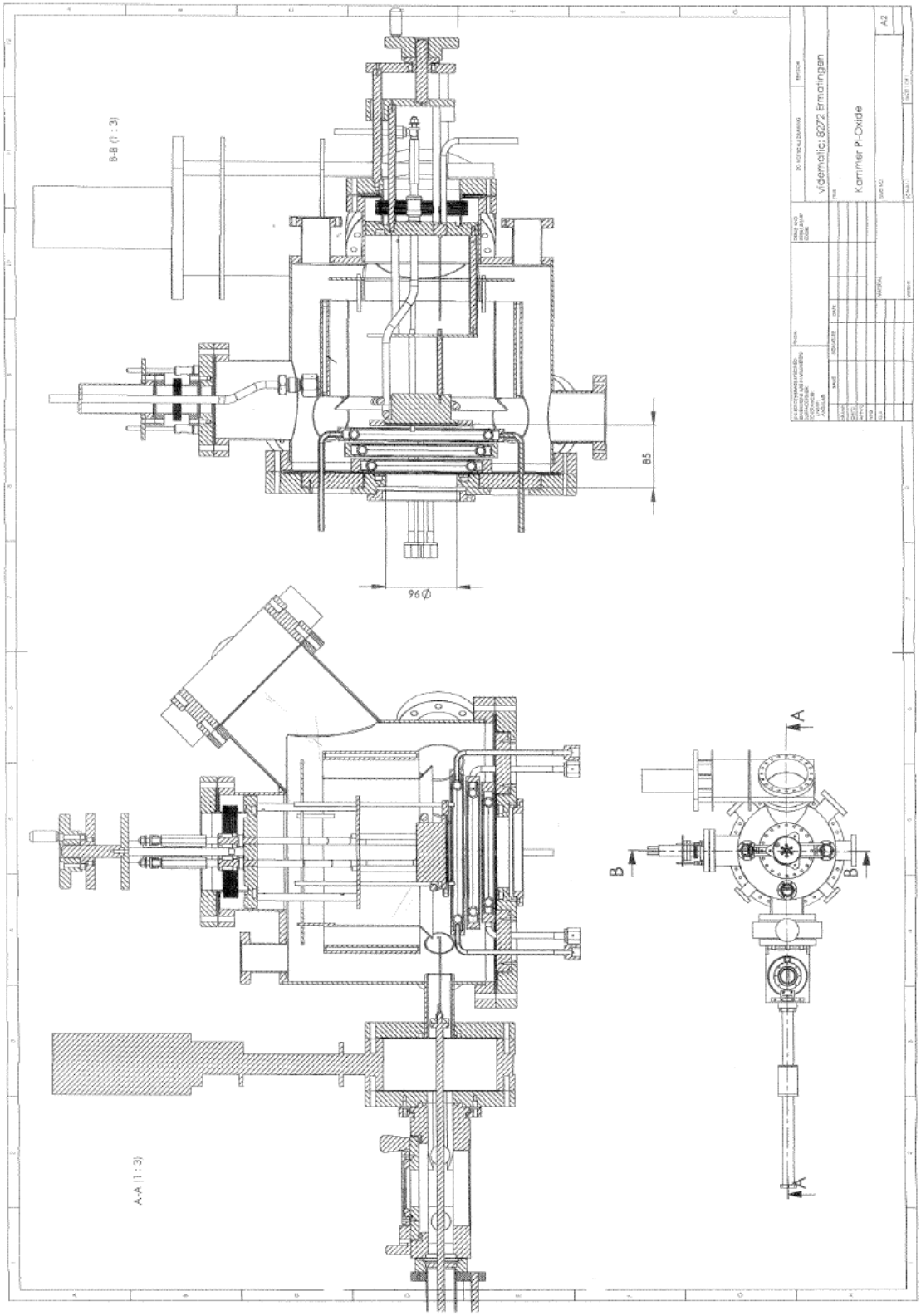

Figure 81 Technical drawing of the HV-CVD chamber.

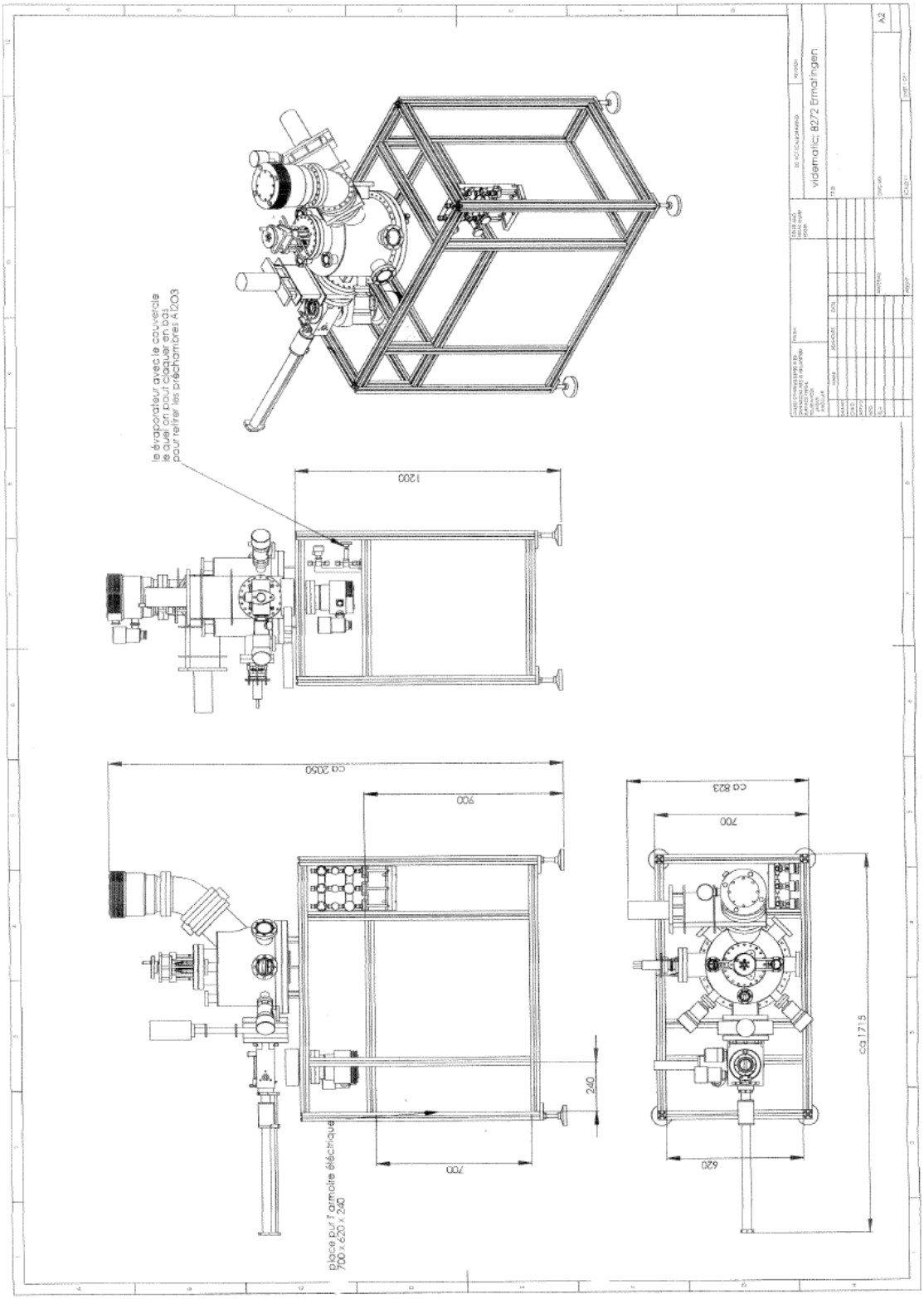

Figure 82 Technical drawing of the HV-CVD setup.

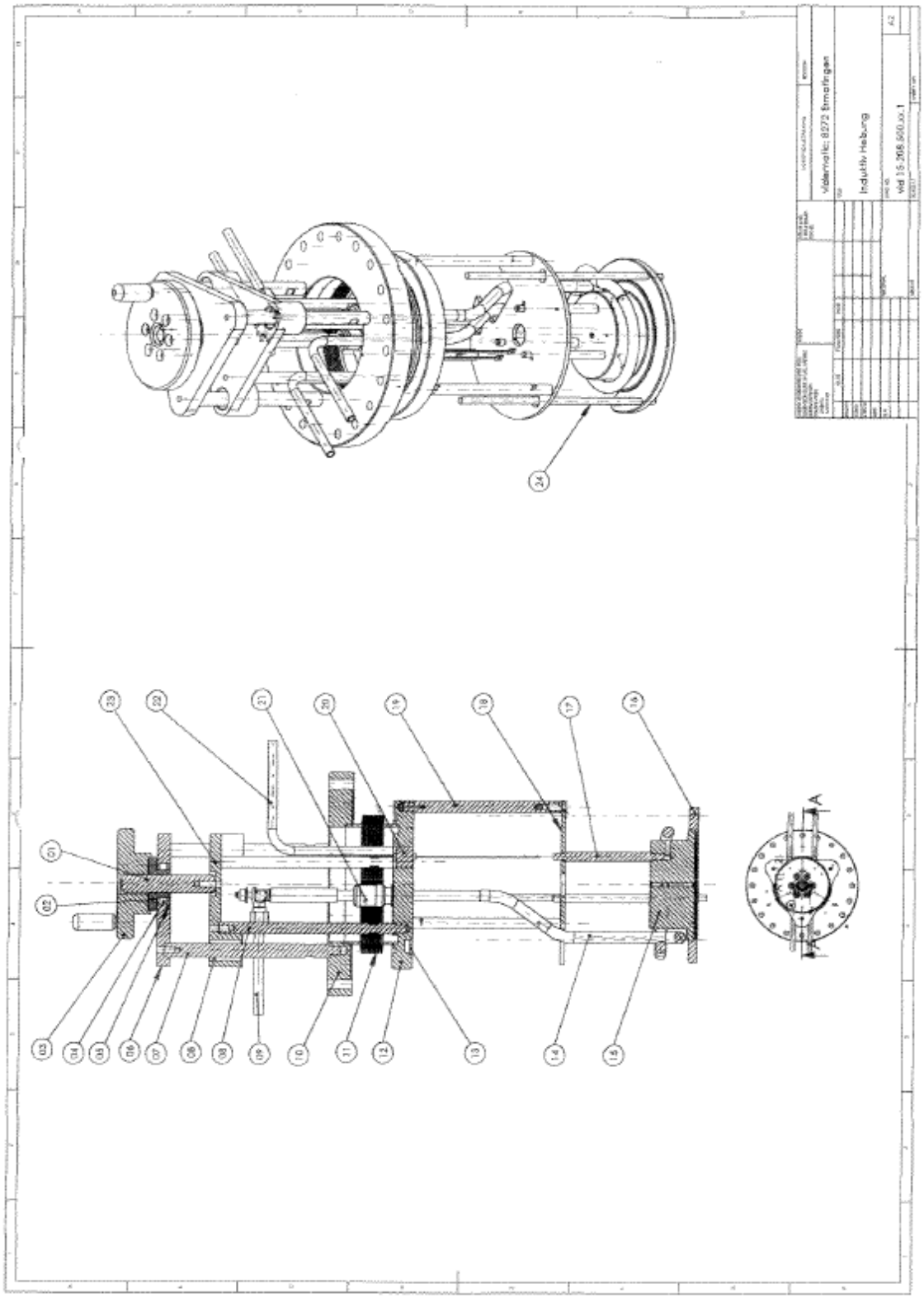

Figure 83 Detail of the substrate holder and heating system.

9.2. Quartz window properties

Transmission properties of the quartz window for the excimer laser illumination setup, about 90% of transmission at 248 nm. (Kurt J. Lesker Company)

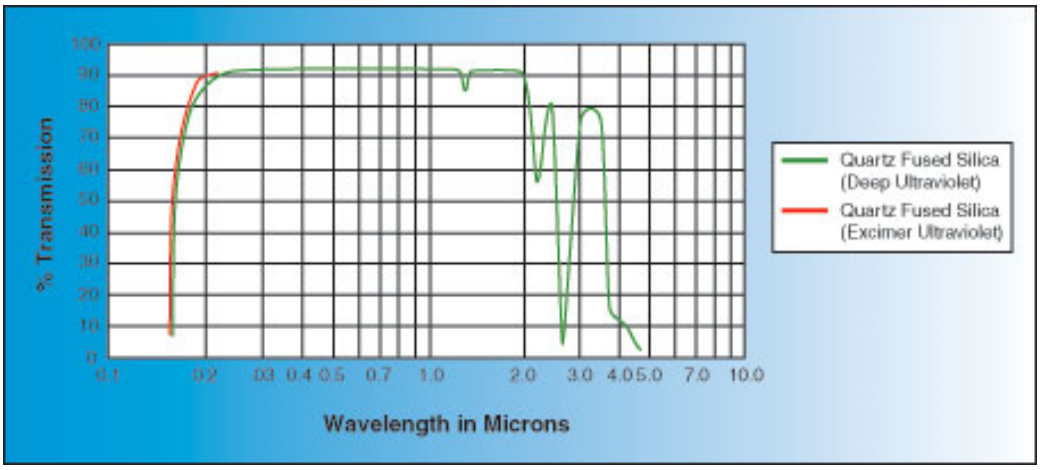

Figure 84 Quartz transmission.

9.3. Heat transfer calculation

The net radiative exchange is expressed as: $q_{ij} = A_i F_{ij} \sigma (T_i^4 - T_j^4)$, where A is the surface, F_{ij} is the fraction of the radiation leaving surface i that is intercepted by surface j and σ the Boltzmann constant.

Considering the three surfaces as illustrated in Figure 85, the net rate of radiation transfer between 1 and 2 is [90]: $q_{12} = \dfrac{A_1 \sigma \left(T_1^4 - T_2^4\right)}{\dfrac{1}{\varepsilon_1} + \dfrac{1}{\varepsilon_2} + \dfrac{1-\varepsilon_{31}}{\varepsilon_{31}} + \dfrac{1-\varepsilon_{32}}{\varepsilon_{32}}}$, where ε_1, ε_2, ε_{31}, ε_{32} are the emissivity of the heater, the wall chamber, the backside substrate and the front side substrate respectively. This relation is true for large infinite parallel surfaces. The same relations can be written for q_{13} and q_{32}.

We have: $q_{12} = q_{13} = q_{32}$

So: $$\frac{\left(T_1^4 - T_3^4\right)}{\dfrac{1}{\varepsilon_1} + \dfrac{1}{\varepsilon_{31}} - 1} = \frac{\left(T_3^4 - T_2^4\right)}{\dfrac{1}{\varepsilon_{32}} + \dfrac{1}{\varepsilon_2} - 1}$$

and finally: $$T_3 = \left[\left(T_2^4 - T_1^4 \right) \frac{\frac{1}{\varepsilon_1} + \frac{1}{\varepsilon_{31}} - 1}{\frac{1}{\varepsilon_1} + \frac{1}{\varepsilon_2} + \frac{1-\varepsilon_{31}}{\varepsilon_{31}} + \frac{1-\varepsilon_{32}}{\varepsilon_{32}}} + T_1^4 \right]^{1/4}$$

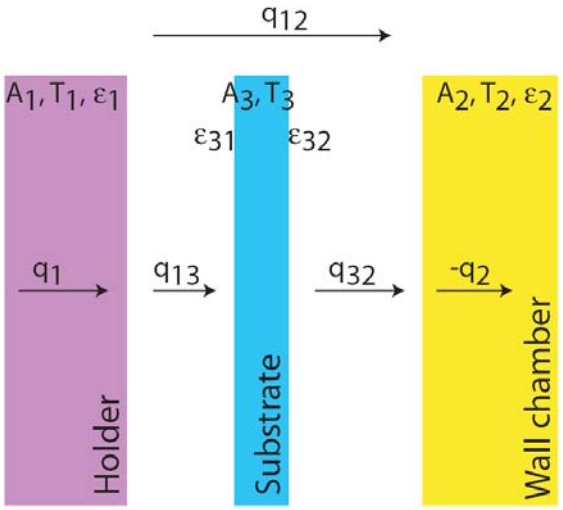

Figure 85 Sketch of the heating system with the different net radiative exchange.

9.4. Emissivity

The emissivity of the different materials used in this work is listed here:

Material	Temperature (° C)	Emissivity	References
Mo	38	0.06	
Mo	1093	0.13	
Al_2O_3	500	0.3	[30]
Stainless steel	600	0.55	
Graphite	500	0.71	
Si	1023	0.6	[141]

Table 15 Emissivity of different materials.

9.5. Correction factors for straight tubular orifices

Clausing's transmission factors for various orifice dimensions

L_0/d_0	W_a	L_0/d_0	W_a
0	1	0.75	0.5810
0.1	0.9092	1	0.5136
0.2	0.8341	1.5	0.4205
0.4	0.7177	2	0.3589
0.5	0.6720	4	0.2316

Table 16 W_a transmission factors.

9.6. Matlab program for distribution simulations

```
%Distance calculation – Geometric relation%
function D = dist_25_source (phi,R,h,precision,power);

[X,Y] = meshgrid(-50:precision:50);

size = 100/precision + 1;

r=sqrt(X.^2+Y.^2);

for i = 1:(size+3)/2
    for j = (size+3)/2:size
        beta(i,j) = atan(-Y(i,j)/X(i,j));
    end
end

for i = 1:(size-1)/2
    for j = 1:(size-1)/2
        beta(i,j) = atan(-Y(i,j)/X(i,j))+pi;
    end
end

for i = (size+3)/2:size
    for j = 1:(size-1)/2
        beta(i,j) = atan(-Y(i,j)/X(i,j))+pi;
    end
end

for i = (size+3)/2:size
    for j = (size+3)/2:size
        beta(i,j) = atan(-Y(i,j)/X(i,j))+ 2*pi;
    end
end
```

```
for j = 1:(size-1)/2
    beta((size+1)/2,j) = pi;
end

for j = (size+1)/2:size
    beta((size+1)/2,j) = 0;
end

for i = 1:(size-1)/2
    beta(i,(size+1)/2) = pi/2;
end

for i = (size+3)/2:size
    beta(i,(size+1)/2) = pi/2*3;
end

for i = 1:size
    for j = 1:size
        if r==0
            D(0,0) = intensity_25_source(phi,R,h,0,0,power);
        else
            D(i,j) = intensity_25_source(phi,R,h,r(i,j),beta(i,j),power);
        end
    end
end
```

```
%Intensity calculation for a single source%
function I = intensity_single_source (phi,R,h,r,beta,power);

I_source=1;

phi = phi/180*pi;

Ax=R-h*tan(phi);
A = [Ax 0 h];
D = [R 0 0];
C = [r*cos(beta) r*sin(beta) h];

cos_theta=costhetaC(A,C,D);

BD = dist(C,D)*cos_theta;

I_BD = (power/2-1)*I_source/(pi*BD^2);

if cos_theta < 0
     I = 0;
else
     I = I_BD*cos_theta^power*cos(phi);
end
```

```
%Intensity calculation for 25 sources%
function I = intensity_25_source (phi,R,h,r,beta,power)

alpha = 2*pi/25;

if r==0
    I=25*intensity_single_source (phi,R,h,0,0,power);
else
```

```
    I=0;
    for i = 1:25
        I = I + intensity_single_source(phi,R,h,r,beta-alpha*(i-1),power);
    end
end

function H = homo (D,precision,range);

size = 2*range/precision + 1;

[X,Y] = meshgrid(-range:precision:range);

r=sqrt(X.^2+Y.^2);

points = 0;

sum = 0;

for i=1:size
    for j=1:size
        if r(i,j) < range
            points = points + 1;
            D_temp(points) = D(i,j);
            sum = sum + D_temp(points);
        end
    end
end

average = sum/points;

H = 0;

for i = 1:points
    H = H + (abs(D_temp(i)-average))^2;
end

H = (H/points)^0.5/average;
```

9.7. Influence of the power in cosine law

Power of the cosine	Distribution simulation	Diametric profile
2.5	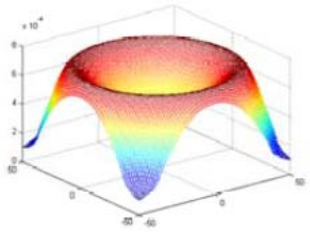	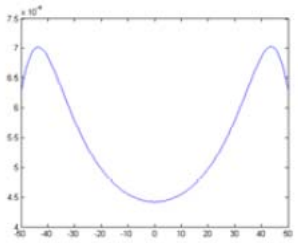
3	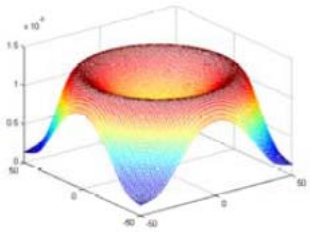	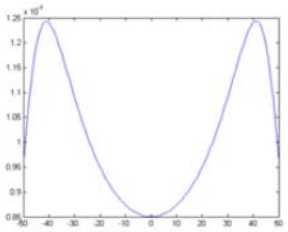
3.5	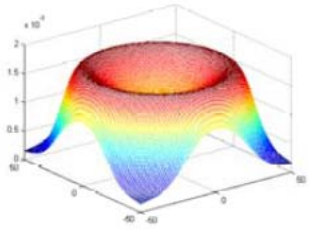	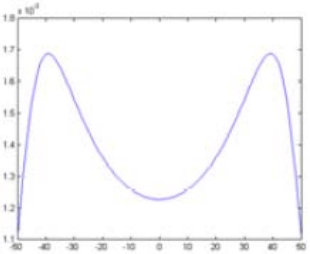
4	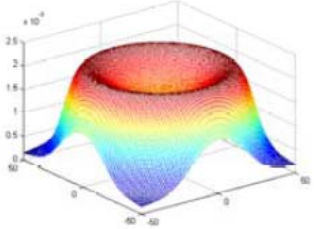	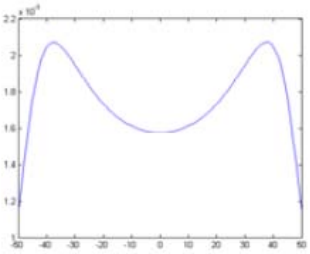
4.5	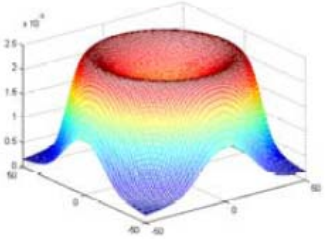	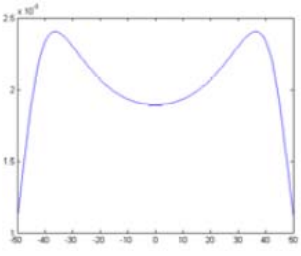

5	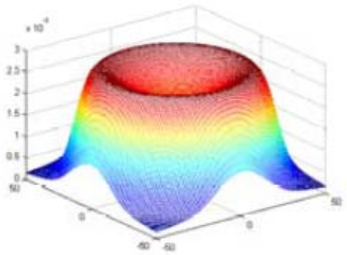	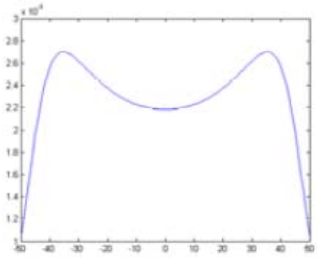
5.5	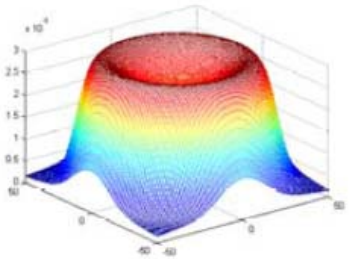	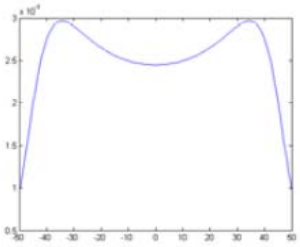

Table 17 Influence of the cosine power on the intensity distribution.

9.8. XRD spectra of different alumina phases

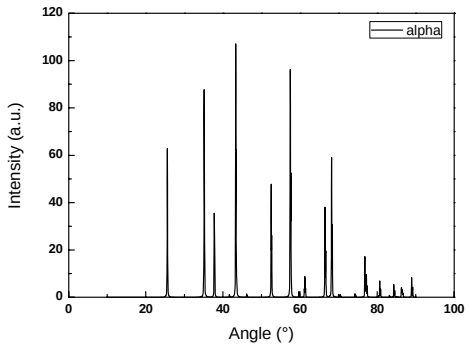

Figure 86 XRD spectrum of alpha alumina.

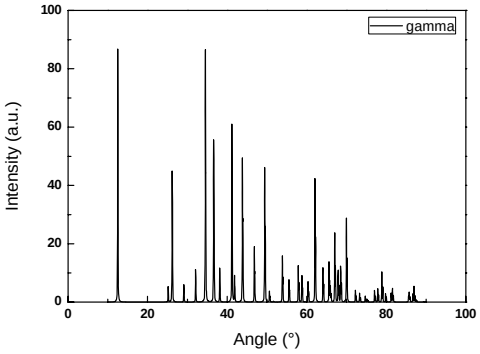

Figure 87 XRD spectrum of gamma alumina.

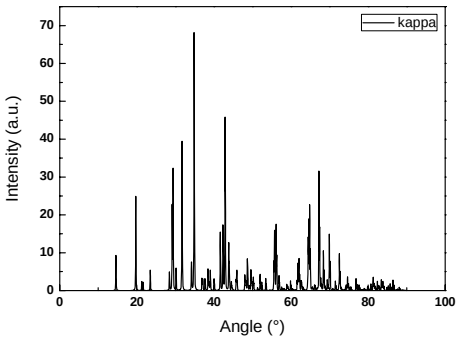

Figure 88 XRD spectrum of kappa alumina.

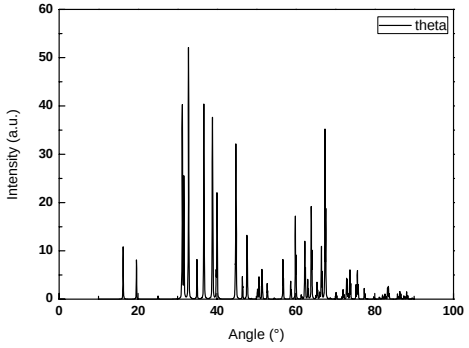

Figure 89 XRD spectrum of theta alumina.

9.9. Erbium tetra-methyl-heptanedionate

The main properties of $Er(TMHD)_3$ are presented here:

Name	CAS	Formula	Structure	State	Price (5 g)
Er $(TMHD)_3$	35733-23-4	$Er(OCC(CH_3)_3 CHCOC(CH_3)_3)_3$	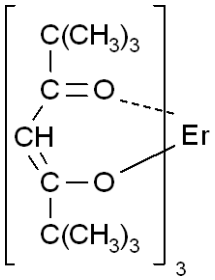	Pink powder	279.5 CHF

Table 18 Erbium tetra-methyl-heptanedionate properties.

Molecular weight (AMU)	Boiling point (°C) @ 38 mm Hg	Melting point (°C)
717.08	345 °C	168-171 °C

Table 19 Physical and chemical properties of $Er(TMHD)_3$.

$Er(TMHD)_3$ sublimes at 160 °C under 0.1 mm Hg and its vapor pressure is reported as $1.33 \cdot 10^{-1}$ mbar at 150 °C [142].

9.10. Alumina structuration process

Reactive Ion Etching (RIE) is a well-established method for producing high quality micron-sized structures with low roughness in optical materials, for the purpose of light propagation with low loss. We investigated the structuring of Al_2O_3 layers using RIE by applying different etching masks consisting of either standard positive

photoresist, or polycrystalline Si, which itself was first structured by photolithography.

The mask design contains several sets of channels with different widths, from 0.8 μm to 2.5 μm with steps of 0.5 μm. The numbers placed on top of the drawing indicate the width of the lines in the corresponding set. Neighbouring sets of 5 lines are separated by two sets of 3 lines having 10 μm in width, which are visible by naked eye and serve as markers for coupling by optical fiber. The 3 line sets can also be used for quick resolution checks during the fabrication process.

While used as the only RIE etching mask for Al_2O_3, the maximum thickness of the photoresist was 2.5 μm. After spin-coating, the photoresist S1818 was structured by UV exposure and subsequent wet development. Channels with sizes between 1 to 10 μm in width and separated by distances of 10 to 150 μm were therefore obtained in the photoresist mask. RIE was then performed in an F-rich atmosphere, while the substrate was cooled down to 0°C. The maximum etching depth of the ribs was around 250 nm, sufficient for obtaining waveguide ribs in the initially 300 nm thick Al_2O_3 films. However, for deeper etching into the Al_2O_3 films, photoresist has limited selectivity which leads to an insufficient depth for channel waveguide fabrication. Therefore, amorphous Si (a:Si), also called poly-silicon was applied as etching mask in order to increase the selectivity in the RIE.

a:Si thin films with thicknesses of 0.5-1 μm were deposited directly onto the Al_2O_3 films, and then coated with photoresist layers of 1.8 μm. After the photolithography structuring of the photoresist, the polycrystalline Si layer was structured by using the photoresist as the mask material by RIE. The remaining photoresist on the surface of the polycrystalline Si was removed in CD26 developer. In order to transfer the so-structured polycrystalline Si profiles onto the Al_2O_3 films, RIE was then performed. Al_2O_3 etching is a highly ions bombardment assisted process. Here an Inductively Coupled Plasma (ICP) etcher has been used. ICP etchers offer high ions density with low pressure plasma. The average ions energy is controlled with the substrate holder voltage biasing by applying the radio frequency (RF) power (13.56MHz). A balance between Al_2O_3 etching and the mask erosion rate has to be found. To expect reasonable selectivity between Al_2O_3 and a:Si during plasma etching a rich carbon fluorine ratio mixture is needed. In this process, key parameters are C_4F_8/CH_4 gas mixture (C/F ratio) to get a good selectivity, Ar flow to enhance Al_2O_3 etching with heavy ions bombardment. ICP power, pressure and substrate holder power are major parameters to control ions flux and ions energy. We have used a dedicated commercial AMS200 ICP plasma etcher from Adixen (Alcatel Vacuum Technology). A complete heated chamber allows to support the highly contaminant C_4F_8/CH_4

chemistry. Without temperature control, some thick polymers depositions following its lift off have to be expected after the first few minutes of processing. The high temperature of the wall chamber insures low polymer deposition rate and an easy cleaning of the polymer with oxygen plasma afterward. The plasma density, i.e. ions flux, depends on the pressure and the ICP power. 0.8Pa and RF power between 2000 and 3000 W were found to be an optimum in our system for the targeted application. Ions bombardment and UV radiation coming from the plasma source heat the substrate. The substrate holder is cooled at 0°C, and the heat transfer between the wafer and the chuck is insured with a 15 mbar static He film. A balance has to be found between the substrate heating due to the process and its cooling with the He flux.

The depth of the etched structures can easily reach 1 µm.

Some previous work on deep silica etching (MEMS-04 Maastricht, "Profile Angle Control in SiO_2 Deep Anisotropic Dry Etching for MEMS Fabrication") has shown the impact of He as a diluted gas in the C_4F_8/CH_4 mixture. 150 sccm He drops drastically the gas residence time and offers a better verticality of the SiO_2 sidewall. For the Al_2O_3 RIE process, Ar is used instead of He. Ar ions are heavier than He ions and provide a better Al_2O_3 etch rate.

Substrate holder voltage biasing is the last key parameter. A too high voltage offers a high Al_2O_3 etch rate but consumes the a:Si mask too quickly, too low voltage enhances polymer deposition on Al_2O_3 and suppresses etching. 200 W was found as a good equilibrium to keep a reasonable Al_2O_3 etch rate with good selectivity to the mask.

Process steps		Description	Equipment	Parameters
Sample preparation	1	Mask wash	Wet bench	Stripper PR for 5 min
Cleaning	2	O_2 plasma	Tepla 300	500 W / 1 min
Photolithography	3	Photo-resist coating (2.5 µm)	RC8	Resist S1818 2500 rpm 30 s
	4	Photo-resist baking	Oven	115 °C / 60 s
	5	Photo-resist	MA6	10 mW/cm^2

		exposure		8.5 s Soft contact
	6	Photo-resist development	CD26	30 s
	7	Post backing	Oven	115 °C / 60 s
	8	Inspection	Microscope Alpha-step	
Etching	9	RIE (90 nm/min)	AMS200	0 °C / 2000 W
Cleaning	10	O_2 plasma	Tepla 300	20 min
PR Mask removal	11	Development	CD 26	1 min
Inspection	12	Resolution	Microscope	

Table 20 Alumina microstructuration steps.

Chapter 10 References

1. Bunshah, R.F., *Handbook of Deposition Technologies for Films and Coatings - Science, Technology and Applications (2nd Edition)*. 1994.

2. Smith, D.L., *Thin-Film Deposition: Principles and Practice*. 1995.

3. Seshan, K., *Handbook of Thin-Film Deposition Processes and Techniques - Principles, Methods, Equipment and Applications (2nd Edition)*. 2002.

4. Elshabini-Riad, A., *Thin Film Technology Handbook*. 1998.

5. Vongutfeld, R.J., M.H. Gelchinski, and L.T. Romankiw, *Maskless Laser Patterning for Gold Plating of Microelectronic Materials.* Journal of the Electrochemical Society, 1983. **130**(9): p. 1840-1844.

6. Ohring, M., *Materials Science of Thin Films*. 2002.

7. Leskela, M. and M. Ritala, *Atomic layer deposition chemistry: Recent developments and future challenges.* Angewandte Chemie-International Edition, 2003. **42**(45): p. 5548-5554.

8. Hitchman, M.L., *Chemical Vapor Deposition: Principles and Applications*. 1993.

9. Madou, M.J., *Fundamentals of microfabrication: the science of miniaturization*. 2002.

10. Atkins, P.W., *Atkins'Physical Chemistry*. 2002.

11. Pierson, H.O., *Handbook of Chemical Vapor Deposition (CVD): Principles, Technology, and Applications*. 1992.

12. Lu, J.P. and R. Raj, *Ultra-High Vacuum Chemical Vapor-Deposition and Insitu Characterization of Titanium-Oxide Thin-Films.* Journal of Materials Research, 1991. **6**(9): p. 1913-1918.

13. West, G.A., A. Gupta, and K.W. Beeson, *CO2 Laser-Induced Chemical Vapor-Deposition of Titanium Silicide Films.* Applied Physics Letters, 1985. **47**(5): p. 476-478.

14. Solanki, R., W.H. Ritchie, and G.J. Collins, *Photodeposition of Aluminum-Oxide and Aluminum Thin-Films.* Applied Physics Letters, 1983. **43**(5): p. 454-456.

15. Kern, W., *Thin film processes*. 1978.

16. Higashi, G.S. and L.J. Rothberg, *Surface Photochemical Phenomena in Laser Chemical Vapor-Deposition.* Journal of Vacuum Science & Technology B, 1985. **3**(5): p. 1460-1463.

17. Fukushima, Y., et al., *Photochemical Vapor-Deposition of Al2O3 Thin-Films with High Quantum Yield.* Japanese Journal of Applied Physics Part 2-Letters, 1992. **31**(3A): p. L261-L264.

18. Hatch, S.R., et al., *Surface Photochemistry 15 - On the Role of Substrate Excitation.* Journal of Chemical Physics, 1990. **92**(4): p. 2681-2682.

19. Tsao, J.Y. and D.J. Ehrlich, *Laser-Chemical Modification of Nucleation Barriers for Area-Selective Thin-Film Growth.* Journal of Crystal Growth, 1984. **68**(1): p. 176-187.

20. Tsao, J.Y. and D.J. Ehrlich, *Patterned Photonucleation of Chemical Vapor-Deposition of Al by Uv-Laser Photodeposition.* Applied Physics Letters, 1984. **45**(6): p. 617-619.

21. Higashi, G.S. and C.G. Fleming, *Patterned Aluminum Growth Via Excimer Laser Activated Metalorganic Chemical Vapor-Deposition.* Applied Physics Letters, 1986. **48**(16): p. 1051-1053.

22. Lux, B., et al., *Preparation of Alumina Coatings by Chemical Vapor-Deposition.* Thin Solid Films, 1986. **138**(1): p. 49-64.

23. Nishio, K., et al., *Effects of apatite and wollastonite containing glass-ceramic powder and two types of alumina powder in composites on osteoblastic differentiation of bone marrow cells.* Journal of Biomedical Materials Research, 2001. **55**(2): p. 164-176.

24. Wei, W.C.J., S.J. Lu, and C.L. Hsieh, *Colloidal processing and fracture strength of alumina prepared from partially agglomerated theta-phase powder.* Journal of the Ceramic Society of Japan, 1996. **104**(4): p. 277-283.

25. Levin, I. and D. Brandon, *Metastable alumina polymorphs: Crystal structures and transition sequences.* Journal of the American Ceramic Society, 1998. **81**(8): p. 1995-2012.

26. Fredriksson, E. and J.O. Carlsson, *Factors Influencing the K-Al2O3 & Alpha-Al2O3 Phase Transformation during CVD Growth.* Surface & Coatings Technology, 1993. **56**(2): p. 165-177.

27. Landolt-Boernstein, *Group IV Physical Chemistry*. Vol. 5a. 1991: Springer-Verlag.

28. Sundgren, J.E. and H.T.G. Hentzell, *A Review of the Present State of Art in Hard Coatings Grown from the Vapor-Phase.* Journal of Vacuum Science & Technology a-Vacuum Surfaces and Films, 1986. **4**(5): p. 2259-2279.

29. Saleh, B.E.A., *Fundamentals of Photonics*, ed. Willey. 1991, New-York.

30. Lide, D.R., *Handbook of chemistry and physics*. 1993.

31. Aboaf, J.A., *Deposition and Properties of Aluminum Oxide Obtained by Pyrolytic Decomposition of an Aluminum Alkoxide.* Journal of the Electrochemical Society, 1967. **114**(9): p. 948-&.

32. Barybin, A.A., et al., *Device for Obtaining Al2O3 Thin-Films.* Pribory I Tekhnika Eksperimenta, 1975(3): p. 238-239.

33. Saraie, J., J. Kown, and Y. Yodogawa, *Chemical Vapor-Deposition of Al2O3 Thin-Films under Reduced Pressures.* Journal of the Electrochemical Society, 1985. **132**(4): p. 890-892.

34. Saraie, J., K. Ono, and S. Takeuchi, *Effects of Various Atmospheres on the Reduced-Pressure CVD of Al2O3 Thin-Films at Low-Temperatures.* Journal of the Electrochemical Society, 1989. **136**(10): p. 3139-3141.

35. Morssinkhof, R.W.J., et al., *The Protective Properties of Thin Alumina Films Deposited by Metal Organic-Chemical Vapor-Deposition against High-Temperature Corrosion of Stainless-Steels.* Materials Science and Engineering A-Structural Materials Properties Microstructure and Processing, 1989. **120**: p. 449-455.

36. Yom, S.S., et al., *Growth of Gamma-Al2O3 Thin-Films on Silicon by Low-Pressure Metal Organic-Chemical Vapor-Deposition.* Thin Solid Films, 1992. **213**(1): p. 72-75.

37. Niska, R.H., et al., *Chemical vapor deposition of alpha aluminum oxide for high-temperature aerospace sensors.* Journal of Vacuum Science & Technology A-Vacuum Surfaces and Films, 2000. **18**(4): p. 1653-1658.

38. Blittersdorf, S., et al., *CVD of Al2O3 thin films using aluminum tri-isopropoxide.* Chemical Vapor Deposition, 2003. **9**(4): p. 194-198.

39. Kodas, T.T., A. Sood, and S.E. Pratsinis, *Submicron Alumina Powder Production by a Turbulent-Flow Aerosol Process.* Powder Technology, 1987. **50**(1): p. 47-53.

40. Haanappel, V.A.C., et al., *Corrosion-Resistant Coatings (Al2O3) Produced by Metal-Organic Chemical-Vapor-Deposition Using Aluminum-Tri-Sec-Butoxide.* Thin Solid Films, 1993. **230**(2): p. 138-144.

41. Haanappel, V.A.C., et al., *Properties of Alumina Films Prepared by Metal-Organic Chemical-Vapor-Deposition at Atmospheric-Pressure in the Presence of Small Amounts of Water.* Surface & Coatings Technology, 1995. **72**(1-2): p. 1-12.

42. Kuo, D.H., B.Y. Cheung, and R.J. Wu, *Growth and properties of alumina films obtained by low-pressure metalorganic chemical vapor deposition.* Thin Solid Films, 2001. **398**: p. 35-40.

43. Ajayi, O.B., et al., *Preparation and Optical Characterization of Pyrolytically Deposited Thin-Films of Some Metal-Oxides.* Thin Solid Films, 1986. **138**(1): p. 91-95.

44. Maruyama, T. and S. Arai, *Aluminum-Oxide Thin-Films Prepared by Chemical Vapor-Deposition from Aluminum Acetylacetonate.* Applied Physics Letters, 1992. **60**(3): p. 322-323.

45. Kim, J.S., et al., *Fabrication of Aluminum-Oxide Thin-Films by a Low-Pressure Metalorganic Chemical Vapor-Deposition Technique.* Applied Physics Letters, 1993. **62**(7): p. 681-683.

46. Kim, J.S., et al., *Effect of Water-Vapor on the Growth of Aluminum-Oxide Films by Low-Pressure Chemical-Vapor-Deposition.* Thin Solid Films, 1993. **230**(2): p. 156-159.

47. Pradhan, S.K., P.J. Reucroft, and Y.K. Ko, *Crystallinity of Al2O3 films deposited by metalorganic chemical vapor deposition.* Surface & Coatings Technology, 2004. **176**(3): p. 382-384.

48. Ishida, M., et al., *Epitaxial Al2O3 Films on Si by Low-Pressure Chemical Vapor-Deposition.* Applied Physics Letters, 1988. **52**(16): p. 1326-1328.

49. Kimura, T., et al., *Epitaxial Si on Al2O3 films grown with O2 gas by the ultrahigh-vacuum chemical vapor deposition method.* Japanese Journal of Applied Physics Part 1-Regular Papers Short Notes & Review Papers, 1998. **37**(3B): p. 1285-1288.

50. Kimura, T., et al., *The effect of oxidation source gas on epitaxial Al2O3 films on Si.* Japanese Journal of Applied Physics Part 1-Regular Papers Short Notes & Review Papers, 1997. **36**(12A): p. 7126-7132.

51. Kamoshid.M, I.V. Mitchell, and J.W. Mayer, *Influence of Deposition Temperature on Properties of Hydrolytically Grown Aluminum Oxide Films.* Applied Physics Letters, 1971. **18**(7): p. 292-&.

52. Iida, K. and T. Tsujide, *Physical and Chemical Properties of Aluminum-Oxide Film Deposited by AlCl3-CO2-H2 System.* Japanese Journal of Applied Physics, 1972. **11**(6): p. 840-&.

53. Kim, J.G., C.S. Park, and J.S. Chun, *Effect of Partial-Pressure of the Reactant Gas on the Chemical Vapor-Deposition of Al2O3.* Thin Solid Films, 1982. **97**(1): p. 97-106.

54. Maruyama, T. and T. Nakai, *Aluminum-Oxide Thin-Films Prepared by Chemical Vapor-Deposition from Aluminum 2-Ethylhexanoate.* Applied Physics Letters, 1991. **58**(19): p. 2079-2080.

55. Ciliberto, E., et al., *Synthesis of Aluminum-Oxide Thin-Films - Use of Aluminum Tris-Dipivaloylmethanate as a New Low-Pressure Metal-Organic Chemical-Vapor-Deposition Precursor.* Applied Physics Letters, 1995. **67**(11): p. 1624-1626.

56. Glass, J.A., S.S. Kher, and J.T. Spencer, *Chemical Vapor-Deposition Precursor Chemistry .2. Formation of Pure Aluminum, Alumina, and*

Aluminum Boride Thin-Films from Boron-Containing Precursor Compounds by Chemical Vapor-Deposition. Chemistry of Materials, 1992. **4**(3): p. 530-538.

57. Lin, C.H., H.L. Wang, and M.H. Hon, *Preparation and characterization of aluminum oxide films by plasma enhanced chemical vapor deposition.* Surface & Coatings Technology, 1997. **90**(1-2): p. 102-106.

58. Lin, C.H., H.L. Wang, and M.H. Hon, *The effect of residual stress on the adhesion of PECVD-coated aluminum oxide film on glass.* Thin Solid Films, 1996. **283**(1-2): p. 171-174.

59. Meiners, L.G., *Electrical-Properties of Al2O3 and AlPxOy Dielectric Layers on InP.* Thin Solid Films, 1984. **113**(2): p. 85-92.

60. Pande, K.P., V.K.R. Nair, and D. Gutierrez, *Plasma Enhanced Metal-Organic Chemical Vapor-Deposition of Aluminum-Oxide Dielectric Film for Device Applications.* Journal of Applied Physics, 1983. **54**(9): p. 5436-5440.

61. Kang, C.J., J.S. Chun, and W.J. Lee, *Properties of Aluminum-Oxide Films Prepared by Plasma-Enhanced Metal Organic-Chemical Vapor-Deposition.* Thin Solid Films, 1990. **189**(1): p. 161-173.

62. Ishida, M., et al., *Decomposition of Trimethylaluminum and N2O on Si Surfaces Using Ultraviolet-Laser Photolysis to Produce Al2O3 Films.* Journal of Vacuum Science & Technology a-Vacuum Surfaces and Films, 1989. **7**(5): p. 2931-2934.

63. Saraie, J. and S. Ngan, *Photo-CVD of Al2O3 Thin-Films.* Japanese Journal of Applied Physics Part 2-Letters, 1990. **29**(10): p. L1877-L1880.

64. Fukushima, Y., et al., *Photo-CVD of Al2O3 Thin-Films Using a D(2) Lamp.* Applied Surface Science, 1994. **80**: p. 361-365.

65. Hudson, M.D., C. Trundle, and C.J. Brierley, *Photochemical Deposition and Characterization of Al2O3 and TiO2.* Journal of Materials Research, 1988. **3**(6): p. 1151-1157.

66. Higashi, G.S. and C.G. Fleming, *Sequential Surface Chemical-Reaction Limited Growth of High-Quality Al2O3 Dielectrics.* Applied Physics Letters, 1989. **55**(19): p. 1963-1965.

67. Fan, J.F., K. Sugioka, and K. Toyoda, *Low-Temperature Growth of Thin-Films of Al2O3 by Sequential Surface Chemical-Reaction of Trimethylaluminum and H2O2.* Japanese Journal of Applied Physics Part 2-Letters, 1991. **30**(6B): p. L1139-L1141.

68. Soto, C. and W.T. Tysoe, *The Reaction Pathway for the Growth of Alumina on High Surface-Area Alumina and in Ultrahigh-Vacuum by a Reaction between Trimethyl Aluminum and Water.* Journal of Vacuum Science & Technology A-Vacuum Surfaces and Films, 1991. **9**(5): p. 2686-2695.

69. Kumagai, H., et al., *Comparative-Study of Al2O3 Optical Crystalline Thin-Films Grown by Vapor Combinations of Al(CH3)3/N2O and Al(CH3)3/H2O2.* Japanese Journal of Applied Physics Part 1-Regular Papers Short Notes & Review Papers, 1993. **32**(12B): p. 6137-6140.

70. Groner, M.D., et al., *Low-temperature Al2O3 atomic layer deposition.* Chemistry of Materials, 2004. **16**(4): p. 639-645.

71. Kattelus, H., et al., *Layered Tantalum-Aluminum Oxide-Films Deposited by Atomic Layer Epitaxy.* Thin Solid Films, 1993. **225**(1-2): p. 296-298.

72. Riihela, D., et al., *Introducing atomic layer epitaxy for the deposition of optical thin films.* Thin Solid Films, 1996. **289**(1-2): p. 250-255.

73. Kukli, K., et al., *Atomic layer epitaxy growth of aluminum oxide thin films from a novel Al(CH3)(2)Cl precursor and H2O.* Journal of Vacuum Science & Technology A-Vacuum Surfaces and Films, 1997. **15**(4): p. 2214-2218.

74. Katamreddy, R., et al., *ALD and characterization of aluminum oxide deposited on Si (100) using tris(diethylamino) aluminum and water vapor.* Journal of the Electrochemical Society, 2006. **153**(10): p. C701-C706.

75. Khanna, V.K. and R.K. Nahar, *Surface Conduction Mechanisms and the Electrical-Properties of Al2O3 Humidity Sensor.* Applied Surface Science, 1987. **28**(3): p. 247-264.

76. Ishida, M., et al., *Epitaxially Stacked Structures of Si/Al2O3/Si for Sensor Materials.* Sensors and Actuators a-Physical, 1990. **21**(1-3): p. 267-270.

77. Smit, M.K., G.A. Acket, and C.J. Vanderlaan, *Al2O3 Films for Integrated-Optics.* Thin Solid Films, 1986. **138**(2): p. 171-181.

78. Cameron, D.C., et al., *Inp Metal-Oxide Semiconductor-Devices Incorporating Al2o3 Dielectrics Chemically Vapor-Deposited at Low-Pressure.* Thin Solid Films, 1982. **91**(4): p. 339-347.

79. Waxman, A. and Zaininge.Kh, *Al2O3-Silicon Insulated Gate Field Effect Transistors.* Applied Physics Letters, 1968. **12**(3): p. 109.

80. Ha, H.Y., et al., *Alumina composite membranes prepared by MOCVD.* Journal of Materials Science Letters, 1997. **16**(12): p. 1023-1026.

81. Vancorbach, H.D., et al., *Al2O3 Coatings against High-Temperature Corrosion Deposited by Metal-Organic Low-Pressure Chemical-Vapor-Deposition.* Thin Solid Films, 1994. **239**(1): p. 31-36.

82. Ritchie, I.T. and B. Window, *Applications of Thin Graded-Index Films to Solar Absorbers.* Applied Optics, 1977. **16**(5): p. 1438-1443.

83. Ryabova, L.A. and Savitska.Ys, *Preparation of Thin Films of Some Oxides by Pyrolysis Method.* Thin Solid Films, 1968. **2**(1-2): p. 141-&.

84. Mahnke, M., et al., *Aluminum oxide doped with erbium, titanium and chromium for active integrated optical applications.* AEU-International Journal of Electronics and Communications, 2001. **55**(5): p. 342-348.

85. vanden Hoven, G.N., et al., *Net optical gain at 1.53 mu m in Er-doped Al2O3 waveguides on silicon.* Applied Physics Letters, 1996. **68**(14): p. 1886-1888.

86. Musa, S., et al., *Characteristics of Er-doped Al2O3 thin films deposited by reactive co-sputtering.* IEEE Journal of Quantum Electronics, 2000. **36**(9): p. 1089-1097.

87. Solehmainen, K., et al., *Erbium-doped waveguides fabricated with atomic layer deposition method.* IEEE Photonics Technology Letters, 2004. **16**(1): p. 194-196.

88. Benvenuti, G., *Chemical beam deposition of titanium dioxide thin films.* EPFL Thesis, 2003. **2744**.

89. Farrell, T., J.V. Armstrong, and P. Kightley, *Dynamic Optical Reflectivity to Monitor the Real-Time Metalorganic Molecular-Beam Epitaxial-Growth of Algaas Layers.* Applied Physics Letters, 1991. **59**(10): p. 1203-1205.

90. Incropera, F.P., *Fundamentals of Heat Transfer*. 1981.

91. Herman, M.A. and H. Sitter, *Molecular Beam Epitaxy.* Springer Series in Materials Science, 1989.

92. Clausing, P., *Flow of Highly Rarefied Gases through Tubes of Arbitrary Length.* Journal of Vacuum Science & Technology, 1971. **8**(5): p. 636-&.

93. Dayton, B.B., *Gas-Flow in Vacuum-Systems.* Journal of Vacuum Science & Technology, 1972. **9**(1): p. 243-&.

94. Halary-Wagner, E., F. Wagner, and P. Hoffmann, *Titanium dioxide thin-film deposition on polymer substrate by light induced chemical vapor deposition.* Journal of the Electrochemical Society, 2004. **151**(9): p. C571-C576.

95. Bauerle, D., *Laser processing and chemistry: recent developments.* Applied Surface Science, 2002. **186**(1-4): p. 1-6.

96. Sovar, M.M., et al., *Aluminium tri-iso-propoxide: Shelf life, transport properties, and decomposition kinetics for the low temperature processing of aluminium oxide-based coatings.* Surface & Coatings Technology, 2007. **201**(22-23): p. 9159-9162.

97. Shiner, V.J., D. Whittaker, and V.P. Fernande, *Structures of Some Aluminum Alkoxides.* Journal of the American Chemical Society, 1963. **85**(15): p. 2318-&.

98. Bradley, D.C., *Structural Theory for Metal Alkoxide Polymers.* Nature, 1958. **182**(4644): p. 1211-1214.

99. Robinson, R.A. and D.A. Peak, *The aluminum alkyl oxides and their parachors.* Journal of Physical Chemistry, 1935. **39**(8): p. 1125-1133.

100. Mehrotra, R.C., *Aluminium Alkoxides.* Journal of the Indian Chemical Society, 1953. **30**(9): p. 585-591.

101. Wilhoit, R.C., *Vapor Pressures of Some Aluminum Alkoxides.* Journal of Physical Chemistry, 1957. **61**(1): p. 114-116.

102. Bleyerve, R., W. Fieggen, and H. Gerding, *Structure and Physical Properties of Aluminum Alkoxides .4. Vapor-Pressures of Aluminum Isopropoxide.* Recueil Des Travaux Chimiques Des Pays-Bas, 1972. **91**(4): p. 477.

103. Shulman, G.P., J.H. Vickers, and M. Trusty, *Thermal Decomposition of Aluminum Alkoxides.* Journal of Organic Chemistry, 1963. **28**(4): p. 907.

104. Taylor, C.J., et al., *Does chemistry really matter in the chemical vapor deposition of titanium dioxide? Precursor and kinetic effects on the microstructure of polycrystalline films.* Journal of the American Chemical Society, 1999. **121**(22): p. 5220-5229.

105. Karpov, I., W. Gladfelter, and A. Franciosi, *Sticking coefficient and growth rate during Al chemical vapor deposition.* Applied Physics Letters, 1996. **69**(27): p. 4191-4193.

106. Kim, Y.C., et al., *Compositional and Structural-Analysis of Aluminum-Oxide Films Prepared by Plasma-Enhanced Chemical-Vapor-Deposition.* Thin Solid Films, 1994. **237**(1-2): p. 57-65.

107. Chowdhuri, A.R., et al., *Metalorganic chemical vapor deposition of aluminum oxide on Si: Evidence of interface SiO2 formation.* Applied Physics Letters, 2002. **80**(22): p. 4241-4243.

108. Griot, M., *Optics guide.* 2002.

109. Assih, T., et al., *Raman-Study of Alumina Gels.* Journal of Materials Science, 1988. **23**(9): p. 3326-3331.

110. Xiong, G., et al., *Effect of atomic layer deposition coatings on the surface structure of anodic aluminum oxide membranes.* Journal of Physical Chemistry B, 2005. **109**(29): p. 14059-14063.

111. Aladjem, A., et al., *Electron-Beam Crystallization of Anodic Oxide Films.* Electrochimica Acta, 1970. **15**(5): p. 663.

112. Shimizu, K., G.E. Thompson, and G.C. Wood, *Electron-Beam-Induced Crystallization of Anodic Barrier Films on Aluminum.* Thin Solid Films, 1981. **77**(4): p. 313-318.

113. Liu, J., et al., *Electron-Irradiation-Induced Crystallization of Amorphous Al2O3 Films on Silicon Substrates.* Phase Transformations in Thin Films - Thermodynamics and Kinetics, 1993. **311**: p. 239-244.

114. Guenther, K.H., *Physical and Chemical Aspects in the Application of Thin-Films on Optical-Elements.* Applied Optics, 1984. **23**(20): p. 3612-3632.

115. Fietzke, F., K. Goedicke, and W. Hempel, *The deposition of hard crystalline Al2O3 layers by means of bipolar pulsed magnetron sputtering.* Surface & Coatings Technology, 1996. **86-7**(1-3): p. 657-663.

116. Parfitt, L., et al., *Residual-Stresses in Amorphous Alumina Films Synthesized by Ion-Beam-Assisted Deposition.* Journal of Applied Physics, 1995. **77**(7): p. 3029-3036.

117. Koski, K., J. Holsa, and P. Juliet, *Properties of aluminium oxide thin films deposited by reactive magnetron sputtering.* Thin Solid Films, 1999. **339**(1-2): p. 240-248.

118. Aspnes, D.E., *Optical-Properties of Thin-Films.* Thin Solid Films, 1982. **89**(3): p. 249-262.

119. Charrier, J., et al., *Optical study of porous silicon buried waveguides fabricated from p-type silicon.* Materials Science in Semiconductor Processing, 2000. **3**(5-6): p. 357-361.

120. Ramsden, J.J., *Porosity of Pyrolyzed Sol-Gel Wave-Guides.* Journal of Materials Chemistry, 1994. **4**(8): p. 1263-1265.

121. Almeida, R.M., et al., *Photoluminescence of erbium-doped silicate sol-gel planar waveguides.* Journal of Sol-Gel Science and Technology, 2004. **31**(1-3): p. 317-322.

122. Hore, S., et al., *Scattering spherical voids in nanocrystalline TiO2 - enhancement of efficiency in dye-sensitized solar cells.* Chemical Communications, 2005(15): p. 2011-2013.

123. Tian, Z.P., et al., *Multilayer structure with gradual increasing porosity for dye-sensitized solar cells.* Applied Physics Letters, 2009. **94**(3): p. -.

124. Apetz, R. and M.P.B. van Bruggen, *Transparent alumina: A light-scattering model.* Journal of the American Ceramic Society, 2003. **86**(3): p. 480-486.

125. Thornton, J.A., *High-Rate Thick-Film Growth.* Annual Review of Materials Science, 1977. **7**: p. 239-260.

126. Movchan, B.A. and Molodkin.Ta, *Multirow Dislocation Boundaries of Grains in Polycrystalline Nickel.* Physics of Metals and Metallography-Ussr, 1969. **27**(6): p. 180-&.

127. Sanders, J.V., *Chemisorption and reactions on metallic films*. 1971.

128. Sohn, Y.H., R.R. Biederman, and R.D. Sisson, *Microstructural Development in Physical Vapor-Deposited Partially-Stabilized Zirconia Thermal Barrier Coatings.* Thin Solid Films, 1994. **250**(1-2): p. 1-7.

129. Guenther, K.H., *Microstructure of Vapor-Deposited Optical Coatings.* Applied Optics, 1984. **23**(21): p. 3806-3816.

130. Kik, P.G. and A. Polman, *Erbium doped optical-waveguide amplifiers on silicon.* Mrs Bulletin, 1998. **23**(4): p. 48-54.

131. Li, S.F., et al., *A numerical analysis of gain characteristics of Er-doped Al2O3 waveguide amplifiers.* Optical and Quantum Electronics, 2002. **34**(9): p. 859-866.

132. Kik, P.G. and A. Polman, *Cooperative upconversion as the gain-limiting factor in Er doped miniature Al2O3 optical waveguide amplifiers.* Journal of Applied Physics, 2003. **93**(9): p. 5008-5012.

133. Li, C.R., et al., *Deposition of Er : Al2O3 films and photoluminescence characteristics.* Chinese Physics Letters, 2003. **20**(9): p. 1613-1615.

134. Sugiura, H., et al., *Ar Ion Laser-Assisted Metalorganic Molecular-Beam Epitaxy of Gaas.* Applied Physics Letters, 1989. **54**(4): p. 335-337.

135. Farrell, T., et al., *XeCl Excimer Laser Assisted CBE Growth of GaAs.* Journal of Crystal Growth, 1992. **120**(1-4): p. 395-398.

136. Tokumitsu, E., et al., *Photo-Metalorganic Molecular-Beam Epitaxy - a New Epitaxial-Growth Technique.* Journal of Vacuum Science & Technology A-Vacuum Surfaces and Films, 1989. **7**(3): p. 706-710.

137. van Dorp, W.F. and C.W. Hagen, *A critical literature review of focused electron beam induced deposition.* Journal of Applied Physics, 2008. **104**(8).

138. Vieu, C., et al., *Electron beam lithography: resolution limits and applications.* Applied Surface Science, 2000. **164**: p. 111-117.

139. Kudelski, A. and B. Pettinger, *SERS on carbon chain segments: monitoring locally surface chemistry.* Chemical Physics Letters, 2000. **321**(5-6): p. 356-362.

140. Domke, K.F., D. Zhang, and B. Pettinger, *Enhanced Raman spectroscopy: Single molecules or carbon?* Journal of Physical Chemistry C, 2007. **111**(24): p. 8611-8616.

141. Jain, S.C., et al., *Total Emissivity of Silicon at High Temperatures.* Journal of Physics D-Applied Physics, 1971. **4**(8): p. 1207-&.

142. Sicre, J.E., et al., *Volatile Lanthanide Chelates .2. Vapor Pressures Heats of Vaporization and Heats of Sublimation.* Journal of the American Chemical Society, 1969. **91**(13): p. 3476-&.

Xavier MULTONE

June 8th 1978, Swiss, single
Micro-engineer EPFL
xavier.multone@epfl.ch
xavier.multone@gmail.com

Closillon 2
CH – 1870 Monthey
+41(0)24.471.94.25
+41(0)79.20.20.216

EDUCATION

- **PhD in Sciences**, Materials Science program 2005 -
  Ecole Polytechnique Fédérale de Lausanne (EPFL)
  High-Vacuum Chemical Vapor Deposition (CVD) of oxides for integrated optics

- **Master of Sciences**, Micro-engineering Section 2000 - 2005
  Ecole Polytechnique Fédérale de Lausanne (EPFL)
  With a specialization in *Applied Photonics*
  Optional lessons: *Optoelectronics*, *Lasers*, *Nanotechnology, Biotechnology*

- **Maturity in Sciences**, Collège de l'Abbaye de St-Maurice (University entrance) 1993 - 1997

EXPERIENCE

- Research Assistant in the Advanced Photonics Laboratory at EPFL 2005 -
  Participating to the European project "PI-Oxide" and supervising students

- Internship with FEI Company, Boston, USA, *R&D nanotechnology department* 2005
  New process of chrome etching by focused electron beam for lithographic application

- Lithographic mask's repair by focused electron beam in collaboration with 2004 - 2005
  FEI Company.
  (Diploma work at EPFL in the Nano Research Group of the Applied Optics Institute)

  This work led to a Patent deposited by FEI Company

- Scanning Electron Microscope formation at the CIME (Interdisciplinary Center of 2005
  Electron Microscope)

- Density's determination of nano-structures induced by focused electron beam 2004
  (Semester project at EPFL in the Nano Research Group of the Applied Optics Institute)

- Micro-fluidic part's realization of a biochip for DNA labeling in food (Semester project 2003
  at EPFL in the Microsystems Institute)

- Student Assistant for practical work in physics 2001

- Different jobs (driver, operator, …) 1995 - 2000

LANGUAGE SKILLS

- French: Mother tongue
- English: Good knowledge
- German: Middle knowledge

COMPUTER SKILLS

- Environments: Windows 98, 2000 NT, XP ; Mac OS, DOS
- Programming languages: C, C++, Java, HTML, Assembleur
- Programs: Microsoft Office, Matlab, Mathematica, Origin, Photoshop, Adobe Illustrator
- Simulation: Comsol multiphysics
- CAO: Pro Engineer

TECHNICAL SKILLS

Experimented with:

- Atomic Force Microscope (AFM)
- Scanning Electron Microscope (SEM)
- Ellipsometry and reflectometry
- Focused Electron Beam (FEB)
- Energy Dispersive X-Ray Analysis (EDX)
- Stylus Nano-Profilometer (SNP)
- X-Ray Diffraction (XRD)
- Fourier transform infrared (FTIR) & Raman spectroscopy

HOBBIES

- Basket-ball : National division player (Swiss champion LNA, vice champion LNB, vice champion 1st league and member of the Swiss young national team)
  Coach and trainer of 1st league team
- Sports in general: Youth and Sport Swiss certificate (Running, fitness, ski)
- Travelling: USA, China, Europe, South America, East-Asia, Africa
- Reading: French and English modern literature

PUBLICATIONS & PATENT

Multone, X., Luo, Y., Hoffmann, P., *Materials Science and Engineering B: Solid-State Materials for Advanced Technology* 146 (1-3), pp. 35-40.

Multone, X., Borca, C.N., Hoffmann, P. *Thin Solid Films* 515, pp. 7542-7545.

Multone X., Afra B., Kuzminykh Y., Hoffmann P., *Tailoring of Optical Properties of Alumina Films Deposited by High Vacuum CVD (HV-CVD)*, In Press.

Kuzminykh Y., Multone X. and Hoffmann P., *Combination of Electron or Laser Beam Irradiation with High Vacuum Chemical Vapor Deposition (HV-CVD) of Al_2O_3 for in-situ Local Structuring on Wafer Scale Substrate*, In Press.

Utke, I., Friedli, V., Michler, J., Bret, T., Multone, X., Hoffmann, P. *Applied Physics Letters* 88 (3), pp. 1-3.

Multone X., Bret T., Hoffmann P., Rossi M.J., *Beam-Induced Etching*, US Patent Application 11/102602 and European Patent Application 06112344.4.